Fiber Laser Based Nonlinear Spectroscopy

By

Peter Adany

Submitted to the Department of Electrical Engineering & Computer Science and the Faculty of the Graduate School of the University of Kansas in partial fulfillment of the requirements for the degree of Doctor of Philosophy

Chairperson: Dr. Rongqing Hui

Dr. Chris Allen

Dr. Shannon Blunt

Dr. David Petr

Dr. Carey Johnson

Date Defended: June 28, 2012

The Dissertation Committee for Peter Adany

certifies that this is the approved version of the following dissertation:

Fiber Laser Based Nonlinear Spectroscopy

_____

Chairperson: Dr. Rongqing Hui

Date approved: June 28, 2012

Abstract

To date, nonlinear spectroscopy has been considered an expensive technique and confined mostly to experimental laboratory settings. Over recent years, optical-fiber lasers that are highly reliable, simple to operate and relatively inexpensive have become commercially available, removing one of the major obstacles to widespread utilization of nonlinear optical measurement in biochemistry. However, fiber lasers generally offer relatively low output power compared to lasers traditionally used for nonlinear spectroscopy, and much more careful design is necessary to meet the excitation power thresholds for nonlinear signal generation. On the other hand, reducing the excitation intensity provides a much more suitable level of user-safety, minimizes damage to biological samples and reduces interference with intrinsic chemical processes. Compared to traditional spectroscopy systems, the complexity of nonlinear spectroscopy and imaging instruments must be drastically reduced for them to become practical. A nonlinear spectroscopy tool based on a single fiber laser, with electrically controlled wavelength-tuning and spectral resolution enhanced by a pulse shaping technique, will efficiently produce optical excitation that allows quantitative measurement of important nonlinear optical properties of materials. The work represented here encompasses the theory and design of a nonlinear spectroscopy and imaging system of the simplest architecture possible, while solving the difficult underlying design challenges. With this goal, the following report introduces the theories of nonlinear optical propagation relevant to the design of a wavelength tunable system for nonlinear spectroscopy applications, specifically Coherent Anti-Stokes Spectroscopy (CARS) and Förster Resonance Energy Transfer (FRET). It includes a detailed study of nonlinear propagation of optical solitons using various analysis techniques. A solution of the generalized nonlinear Schrödinger equation using the split-step Fourier method is demonstrated and investigation of

optical soliton propagation in fibers is carried out. Other numerical methods, such as the finite difference time domain approach and spectral-split step Fourier methods are also described and compared. Numerical results are contrasted with various measurements of wavelength shifted solitons. Both CARS and FRET test-bed designs and experiments are presented, representing two valuable biochemical measurement applications. Two-photon excitation experiments with a simplified calibration process for quantitative FRET measurement were conducted on calmodulin proteins modified with fluorescent dyes, as well as modified enhanced green fluorescent protein. The resulting new FRET efficiency measurements showed agreement with those of alternative techniques which are slower and can involve destruction of the sample. In the second major application of the nonlinear spectroscopy system, CARS measurement with enhanced spectral resolution was conducted on cyclohexane as well as on samples of mouse brain tissue containing lipids with Raman resonances. The measurements of cyclohexane verified the ability of the system to precisely determine its Raman resonances, thus providing a benchmark within a similar spectral range for biological materials which have weaker Raman signal responses. The improvement of spectral resolution (resonance frequency selectivity), was also demonstrated by measuring the closely-spaced resonances of cyclohexane. Finally, CARS measurements were also made on samples of mouse brain tissue which has a lipids-based Raman signature. The CARS spectrum of the lipid resonances matched well with other cited studies. The imaging of mouse brain tissue with Raman resonance contrast was also partially achieved, but it was hindered by low signal to noise ratio and limitations of the control hardware that led to some dropout of the CARS signal due to power coupling fluctuations. Nevertheless, these difficulties can be straightforwardly addressed by refinement of the wavelength tuning electronics. In conclusion, it is hoped that these efforts will lead to greater accessibility and use of CARS,

FRET and other nonlinear spectral measurement instruments, in line with the promising advances in optics and laser technology.

Acknowledgements

For their wonderful support, I would like first and foremost to thank my parents Zsuzsanna Vámos and István Ádány, and my sisters Anikó and Eszter.

I would also like to thank many friends and colleagues with whom I've shared interesting technical discussions and ideas, especially Chris Shively and Rory Petty who have continuously fueled my engineering imagination.

I would like to thank every member of my dissertation committee: Dr. Chris Allen, Dr. Shannon Blunt, Dr. David Petr, and Dr. Carey Johnson, each of whom contributed to my education and research in exemplary ways. They represent some of the very best teachers and professional role models I've had.

Finally, yet most importantly, I would like to thank my advisor Dr. Rongqing Hui for the tremendous opportunities, his valuable help and mentorship, and his never-ending enthusiasm. From the beginning of my graduate education, Dr. Hui has raised my sights higher and higher and made an incalculable impact on my academic and professional growth.

Table of Contents

List of Figures

I. Introduction

Current nonlinear spectroscopy techniques cannot be widely utilized. This is a major problem because useful nonlinear spectroscopy techniques have been developed for decades, while practical applications have remained extremely limited. The major hindrances have been the lack of intrinsic rapid wavelength tunability of lasers, and the reliance on high-power, complex laser systems for excitation. With the goal of overcoming these limitations, a system developed based on a fiber laser and electronically controlled wavelength tuning can provide the capability of nonlinear spectroscopy, as it:

(1) meets the power level and spectral resolution needs for multi-wavelength excitation with the use of novel pulse shaping techniques, and

(2) addresses the needs for quantitative spectroscopy with rapid-wavelength tuning, thereby improving calibration and expanding the versatility of nonlinear spectroscopy.

Proposed Project

The project will utilize a fiber laser that is self contained and commercially available. The key features are (1) 120 femtosecond-pulsewidth output at 806 nm with a 75 MHz repetition rate, (2) approximately 100 mW average power, (3) relatively low cost, low maintenance and high reliability compared to optically pumped crystal cavity lasers.

The fiber laser has a relatively low output power compared to the needs for nonlinear excitation, and like most laser designs it does not offer an intrinsic agile wavelength tuning capability. Therefore, we: (1) have to make full use of the fiber laser power, (2) introduce electrically controlled wavelength tuning, and (3) solve the problems associated with power and resolution constraints for useful nonlinear spectroscopy applications.

Contributions

The major contribution of this research can be summarized as:

(1) In order to design useful wavelength shifting devices, we made new investigations of soliton self frequency shift (SSFS) in photonic crystal fibers with various dispersion and nonlinear characteristics. While the optical theory behind soliton effects in nonlinear media has been previously developed, most analytical results have used perturbation approaches which are mostly appropriate for effects in long-haul communications under moderate power levels. Higher input power studies have been done, but they have not offered results applicable to designing wavelength tuning systems. The challenge remained to develop detailed numerical wavelength-tuning studies of multi-soliton output spectra with very high power propagation in very short spans of photonic crystal fiber. We developed numerical algorithms that solved the specific difficulties of modeling SSFS wavelength shift based on solutions of the Generalized Nonlinear Schrödinger Equation and Raman scattering in Photonic Crystal Fiber. This improved the understanding and predictions of wavelength shift for different pulsed lasers and photonic crystal fibers in the design of the wavelength shifting system.

(2) We proposed and developed a two-photon FRET system based on a wavelength switchable femtosecond laser source, which has the potential to significantly simplify the FRET calibration process. Applications of the system are demonstrated with a fluorescence-labeled biological material, Calmodulin (CaM), as well as a fluorescent protein, E^0GFP-mCherry. The results of FRET efficiency measurement of CaM closely agreed with previous results and demonstrated the flexibility of FRET measurement without loss of accuracy. FRET measurement over spans of time effectively requires continuous calibration of measured fluorescence signals. Results from CaM confirmed the independence of the FRET results from the donor excitation wavelength,

allowing a variety of rapid wavelength tuning modes. The speed limitation of techniques that require alternating banks of optical filters was thus overcome. Furthermore, Calmodulin studies included the presentation of new two-photon absorption spectra of fluorescent dyes, along with their one-photon excitation spectra, which is a valuable contribution because extremely few spectra of these dyes have been previously published. In the studies of E^0GFP-mCherry, the accuracy of the two-photon FRET system was further verified by independent one-photon FRET assessment made using a standalone UV-VIS instrument. This was possible because the E^0GFP-mCherry protein was specially engineered with a Thrombin-sensitive bridge, allowing the two fluorophores to be chemically cleaved. Therefore, the E^0GFP-mCherry studies offered an independent verification of FRET accuracy.

(3) We proposed and demonstrated a single-fiber laser based CARS system in which a wavelength scanned Stokes wave was obtained through SSFS. A novel technique was demonstrated that significantly improved the frequency resolution of CARS spectroscopy through the application of identical linear frequency chirping on both the pump and the Stokes optical pulses. The resolution enhancement technique avoids inefficiencies by allowing matched excitation pulse widths and by allowing higher peak power than for comparable frequency resolution achieved simply by using longer transform-limited pulses. This made possible the acquisition of CARS signals with a single fiber laser as the source. In the un-chirped case, the frequency selectivity is limited by the properties of the excitation pulses to a value of 200 cm^{-1} to 250 cm^{-1}. With the frequency chirping technique, the resolution was improved to 30 cm^{-1}. The CARS spectrum of Cyclohexane was measured, both with and without application of frequency chirp. Cyclohexane has Raman resonances separated by roughly 70 cm^{-1} at a central Raman frequency of about 2900 cm^{-1}, and the two peaks were clearly resolved only after applying the

frequency chirping technique. A pulse delay compensation design is also presented, which reduces the time walk-off between the two excitation pulses resulting from wavelength shift. Finally, CARS measurements of a mouse brain tissue sample were made. The CARS spectrum of the tissue was characterized, and although the signal to noise ratio (SNR) was very low, its peak CARS response corresponded with other CARS spectra of similar samples made using much higher excitation power. The acquisition of a Raman-contrasted image of the tissue was attempted, but limitations by low SNR and unmitigated pulse jitter prevented the realization of a useful image. All of the remaining obstacles to imaging can be addressed with straightforward improvements to the system hardware as discussed in the conclusions.

To fully detail these efforts, the following chapters develop the theories of nonlinear optical propagation relevant to the design of a wavelength tunable system for nonlinear spectroscopy applications, specifically Coherent Anti-Stokes Spectroscopy (CARS) and Förster Resonance Energy Transfer (FRET). A detailed study of nonlinear propagation of optical solitons using various numerical analysis techniques follows. The theories of CARS and FRET, as well as experimental designs and experiments are detailed, and successful results of CARS and FRET measurements are presented.

The experiments presented in this report establish benchmarks for both CARS and FRET techniques at the lowermost power thresholds. Traditionally, nonlinear spectroscopy has been bound to dedicated laboratory settings, where large, high power lasers are available. High power lasers are not only difficult to miniaturize and mass produce, but in some cases they also pose serious safety hazards that necessitate restricted access, user-training and operational safeguards. Most importantly, high intensity lasers are destructive to biological materials because of heating and deterioration by photobleaching. As helpful as laboratory lasers have been to the

development of nonlinear spectroscopy, they have not promoted its widespread standard use. The new class of lower-power, portable and robust fiber lasers may bridge this gap between experimental and practical application.

History of Lasers and Fiber Optics

The first working laser was demonstrated in May of 1960 by Ted Maiman, after Gordon Gould's functional design and proposal of the word *laser* in 1957. The invention was a successor of the microwave resonant cavity developed a few years prior by Charles H. Townes and James Gordon. The idea of optical amplified cavities followed from advances in quantum theory, from Einstein's elucidation of stimulated emission in 1916 to the studies of negative absorption by Valentin A. Fabrikant in 1939 [1-3]. Lasers caught the world by surprise. Maiman's initial report on the device was rejected out of skepticism, and the public was quick to mistake lasers as fantastical weapons, or worse, boring devices without practical use. [4] Yet, to research laboratories the concept was eminently promising and by 1962 the first visible-wavelength and semiconductor lasers had already been developed. Despite its brief history, the sequence of discoveries and breakthroughs surrounding lasers is remarkable. In fifty years, some of the landmark achievements included (1) discovery of various gain media for lasing at various wavelengths, (2) development of high power CW gas lasers now widely used in manufacturing, (3) refinement of efficient and reliable diode lasers, and (4) introduction of femtosecond lasers such as the titanium sapphire laser which is now central to chemistry and physics research. Revolutionary applications of lasers included the holograph invented by Dénes Gábor [5] as well as the new fields of femtochemistry and nonlinear spectroscopy [6]. Lasing inside optical fibers was also pursued early on [7-8]. In more recent years, developments have included the production of single-cycle optical pulses in the far-infrared and optical wavelengths [9] [10-11], high energy free-electron lasers [12] and the emergence of consumer fiber lasers.

Light guiding structures go back as far as the early 1800's, but widespread digital optical fiber communications began only sometime after 1978 [13]. The growth of the internet and its

massive worldwide fiber optic network led to the commoditization of sophisticated technologies. Examples of new mainstay technologies include standardized silica optical fiber, narrow line-width lasers for transmission at 800 and 1550 nm wavelengths, high speed electro-optic modulators, rare-earth element doped fiber amplifiers, and instruments such as optical spectrum analyzers and time-domain reflectometers. Photonic crystal fibers flirted with similar success because of their potential to solve the dispersion problems of standard graded-index fiber in long-haul fiber links. Although photonic crystal fibers were not widely adopted for communication networks, their manufacture led to extensive research on optical soliton and supercontinuum generation for measurement applications. Lasers and optical fiber technologies have thus catalyzed developments in spectroscopy and bio-imaging ever since their invention only a few decades ago.

All of the aforementioned developments paved the way towards bringing lab-proven nonlinear optical measurement techniques into everyday scientific use. Alongside lasers and optical fibers, a broader industry of high precision optical components has flourished. So far, nonlinear spectroscopy has been confined mostly to the experimental laboratory setting. The work presently reported is devoted to developing the most simple and practical nonlinear spectroscopy systems possible. It is hoped that greater accessibility to Coherent anti-Stokes Spectroscopy (CARS) and other nonlinear spectral measurement, made possible by the developments in neighboring technologies, will lead to its better utilization in a wide range of applications, especially chemically selective imaging for biological applications.

Microscope Configurations

A good entry point to the subject of fiber laser based nonlinear spectroscopy is an overview of the microscope and its adaptation for laser illumination. Laser-based microscope spectroscopy and imaging traditionally begins in the laboratory, where specimens are sectioned and mounted on a glass slide for observation with a microscope. Conventional lab microscopes are designed for incandescent light sources. The optical configuration can be categorized according to the methods of (1) illumination, (2) light collection and (3) stray light rejection. The simplest is the wide field configuration, requiring only one or two objective lenses and the projection (seeing) optics. The major limitation of wide field imaging is interference by scattered light originating outside the focal plane. The problem of this extraneous light scattering has been solved by the confocal system and more recently with two-photon laser excitation. These methods require scanning of the sample to produce images point-by-point, and both methods provide *optical sectioning* which is the rejection of unwanted scattered light in the image. Optical sectioning is achieved in confocal microscopy with the placement of pinhole apertures between the lenses and the imaged sample. Two-photon excitation achieves optical sectioning by the square-law characteristic of the nonlinear optical response. Another benefit of two-photon excitation is that the emission wavelength is widely shifted from the excitation wavelength, making it easy to isolate the emitted light with filters.

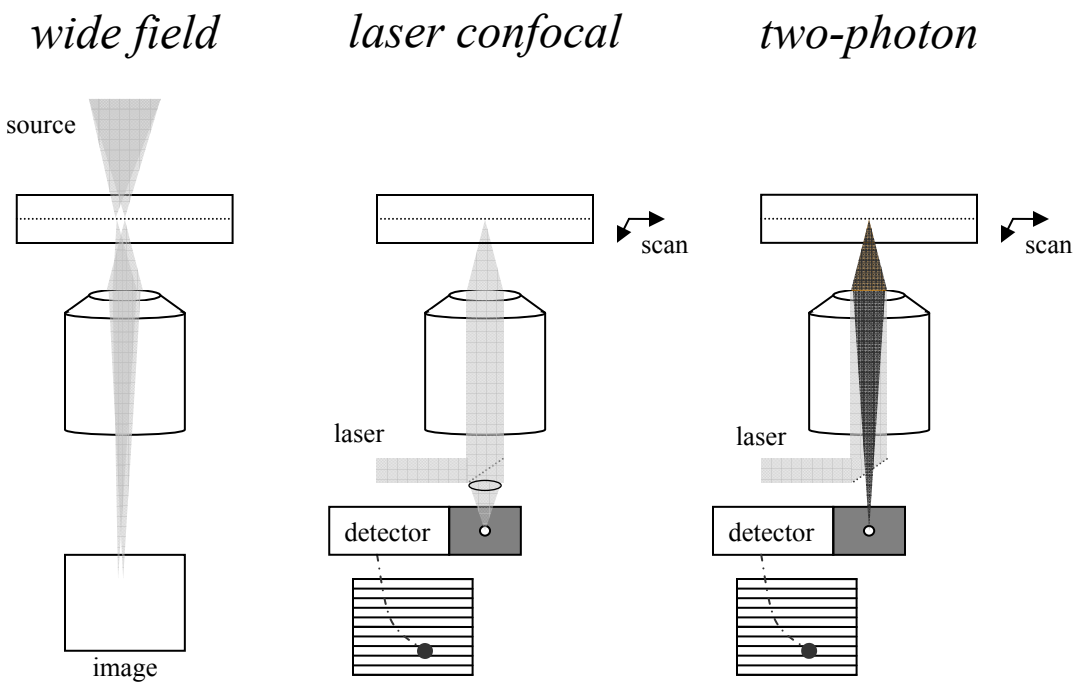

Figure 1. Microscope optical configurations.

Common microscope configurations are illustrated in Figure 1. In most microscopes the objective lens axis is vertical and light is captured in the downward direction. To adjust focus, the objective is raised and lowered using a gear rail. Light from the objective is often reflected by a mirror or dichroic film housed in a rotating carousel for rapid selection. The stage that holds the specimen is either fixed to the microscope body or it may move via transverse positioners. These features are useful for accommodating multiple imaging tasks and providing thermal and mechanical isolation, but they do hinder the precise and stable alignment of a laser input. On the other hand a microscope body is not strictly needed, and for safety reasons laser systems are usually built on an optical bench with the beam oriented horizontally. In a horizontal setup, separate excitation and collection objectives can easily be positioned opposite each other. When using two lenses, the matching of their numerical apertures and other properties becomes an important consideration.

Focusing Lens Mismatch

For spectroscopic measurements a slide-mounted sample (usually a thinly sliced section or a liquid layer under a thin glass cover slip) is placed between a pair of focusing lenses. The primary (objective) lens focuses excitation power into a refraction-limited focal volume in the sample, and the secondary (collector) lens captures emitted light. The main purpose of the primary lens is to focus illumination into the smallest focal volume possible in order to achieve the best resolution and to maximize nonlinear response. The size of the focal volume depends on the numerical aperture (*NA*) of the lens and the quality of the lens backfill. The numerical aperture and maximum light cone angle (ϕ_{NA}) are related by

$$\phi_{NA} = \sin^{-1}\left(NA / n_O\right) \tag{1}$$

where n_O is the refractive index of the surrounding medium. Usually the medium is air, water or an index matching oil. An *NA* value can also be used to refer to any cone-shaped propagating light field, in which case the medium will be assumed to be air. The backfill characteristic of a laser and lens combination must be considered because the beam generally has a Gaussian mode profile and the intensity is not uniform over the lens surface. Because of this, the theoretical resolution formula,

$$R = \frac{1.22\lambda}{NA_{excitation} + NA_{collection}} \tag{2}$$

does not hold. Perfectly uniform backfill is not realistic because it would require an infinitely large beam radius.

The purpose of the secondary (collector) lens is to capture as much of the available optical power as possible. Uneven backfill of the collector results in a somewhat increased spot size at the photo detector. The photo detector is usually larger than the spot size, even one enlarged by diffraction, so the collector backfill is not a major concern, and therefore the main concern is that

the collector *NA* must be approximately equal to the *NA* of the emitted light cone in order to catch all the available light.

Unfortunately, lenses are never ideal because of the material properties of dispersion, attenuation and surface distortion, and their physical dimensions depend on the magnification power as well. For the primary lens, a high *NA* is desired. However, the working distance (wd) of high *NA* objectives is very short (≈0.3 mm). It is not possible to fit a traditionally mounted sample between two such lenses. An illustration of the lens placement is shown in Figure 2.

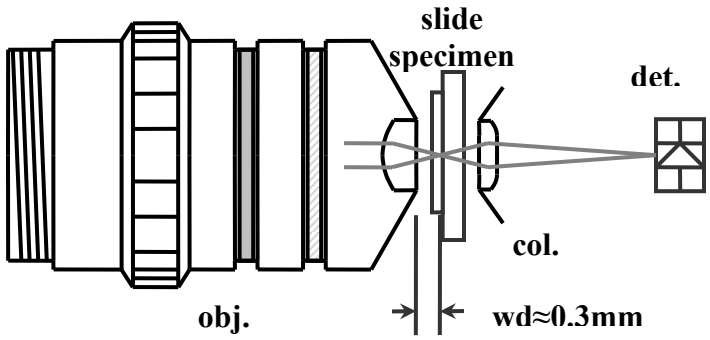

Figure 2. Horizontal beam focusing setup.

When the available power is very limited, as with the CARS system in this study, one important question is whether to use two identical lenses with lower *NA* or to use a higher *NA* lens on the primary side. For comparison, specifications of three lenses variously used in the CARS and FRET systems are given in Table 1.

Objective lens pairs are used ubiquitously in microscopy, and a rubric is needed for estimating lens mismatch losses for laser applications. Therefore, straightforward equations are formulated here that address (1) the degree of power loss incurred because the first lens has a finite diameter that crops the input beam, and (2) the degree of power loss between lenses of unequal numerical apertures, which is the result of an area integral of the beam profile parameterized by the lens *NA*

and the input beam size. The results are demonstrated with figures that facilitate comparison with visual observations.

Table 1. Objective lens specs.

lens	power	*NA* (medium)	wd	f
Olympus LCPlanFL 40x/0.60 air UIS	40x	0.60 (air)	2.60 mm	4.5 mm *
Olympus UPlanSApo 60x/1.20 water UIS2 inf/0.13-0.21/FN26.5	60x	1.20 (water)	0.28 mm	
Newport M-20x 0.40 5.0 mm beam diameter	20x	0.40 (air)	1.70 mm	9 mm

*** based on f=180/power where 180 mm is the Olympus UIS tube lens focal length.**

Firstly, a parameter is needed to evaluate losses due to cropping of the input beam profile by the first lens. We can define a backfill parameter Γ as the integration of the beam profile ρ over the angular aperture of the lens,

$$\Gamma = \int_{-\phi_{NA}}^{\phi_{NA}} \rho(\theta) d\theta \tag{3}$$

where the normalization of ρ is such that $0 < \Gamma < 1$, and therefore Γ is a normalized ratio with regard to an infinitely large beam radius for which $\Gamma = 1$.

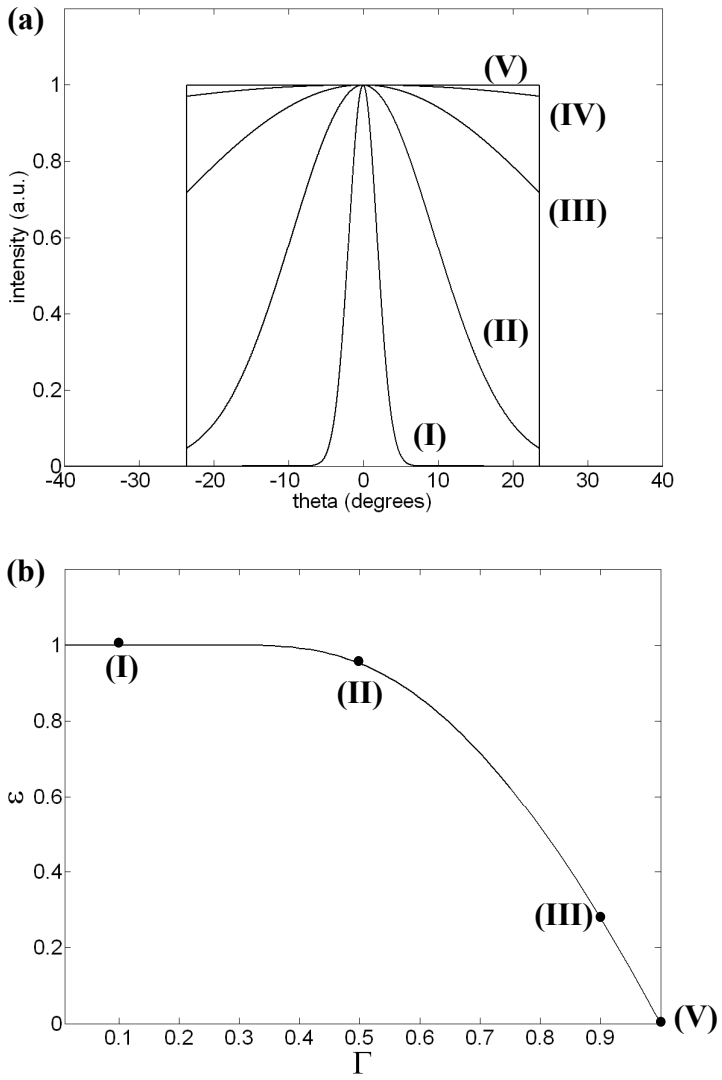

Figure 3. Beam profiles (a) and beam capture factor (b).
Both figures assume a 0.40 *NA* air objective.
Backfill parameter values: Γ = 0.10 (I), 0.50 (II), 0.90 (III), 0.99 (IV) and 1.00 (V)

Illustrations of beam profiles for different values of Γ with respect to a 0.40 *NA* lens are shown in Figure 3. Note that Γ does not represent power efficiency, because it is based on the beam cross-section rather than an area integral. As such, Figure 3 depicts values of Γ that can be easily compared to visual observations. The one-dimensional beam profile can be written as a Gaussian function ρ,

$$\rho(\theta) = \frac{1}{\sqrt{2\pi}\sigma} e^{\left(\frac{-\theta^2}{2\sigma^2}\right)} \tag{4}$$

where θ is the angle from normal and σ is calculated based on a give value of Γ. The standard error function $erf(\alpha)$ is

$$erf(\alpha) = 2 \cdot \int_0^{\alpha} \frac{1}{\sqrt{\pi}} e^{-x^2} dx \tag{5}$$

and it can be applied in this situation by relating α and σ as

$$\sigma = \frac{\phi_{NA}}{\sqrt{2}\alpha(\Gamma)} \tag{6}$$

The laser beam's mode field diameter is $D_{fwhm} = \sqrt{2\ln(2)}\,\sigma$. Finding the value of α for a given Γ requires the solution of

$$erf(\alpha) = \Gamma \cdot \frac{2\alpha}{\sqrt{\pi}} \tag{7}$$

An exact solution can be found by power series expansion of the standard error function, resulting in the equation

$$\Gamma(\alpha) = \sum_{n=0}^{\infty} \frac{(-1)^n \alpha^{2n}}{(2n+1)\,n!} \tag{8}$$

Solving this for α is cumbersome, however a good approximation is

$$\alpha(\Gamma) \approx \left(0.75 \cdot \left(\Gamma^{-2.5} - 1\right)\right)^{0.4} \tag{9}$$

The primary lens crops the input beam area, resulting in a power loss factor $(1-\varepsilon)$, where ε is determined by the backfill ratio and lens angular aperture. This value is an efficiency factor found as

$$\varepsilon = \frac{\int_0^{\phi_{NA}} \theta\,\rho(\theta)\,d\theta}{\int_0^{\infty} \theta\,\rho(\theta)\,d\theta} \tag{10}$$

The function is graphed in Figure 3, showing that the cropping loss becomes very high as the maximum resolving power of the lens is reached. It should be noted, however, that the laser beam width itself is always limited because of the generally small diameter of the cavity.

Next, the *NA* mismatch of the excitation and collection lenses must be considered. Power transfer is reduced when a smaller-*NA* collector lens is paired with a higher-*NA* primary lens. Rather than to evaluate every possible combination, we start with the highest possible *NA* lens as the primary lens because doing so will usually maximize the nonlinear signal according to the square-law response. Then, the efficiency is evaluated as a function of secondary lens *NA* and backfill parameter values. This efficiency is defined as

$$\eta = \frac{\int_0^{\phi_{col}} \theta\,\rho(\theta)\,d\theta}{\int_0^{\phi_{obj}} \theta\,\rho(\theta)\,d\theta} \tag{11}$$

where the $0 < \eta < 1$. The characteristic traces of η are given in Figure 4, with vertical lines demarcating the three popular lens *NA*s (also listed in Table 1). The legend denotes values of Γ which also correspond to those of Figure 3.

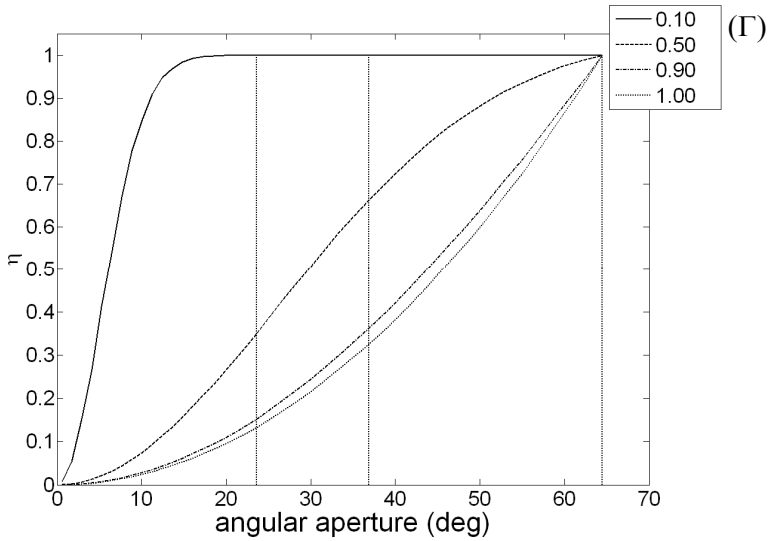

Figure 4. Lens coupling efficiency.
Vertical lines left to right denote NA/ni: 0.40/1.00, 0.60/1.00, 1.20/1.33, where ni is refractive index outside lens. Input: 1.20/1.33 lens. Legend denotes values of Γ.

While the lens mismatch efficiency η has a significant practical impact, the beam cropping loss $(1-\varepsilon)$ is not always a countable loss because laser cavities are by nature finite in size, and high *NA* lenses must realistically be small to mitigate chromatic dispersion. The above figure shows that lens-mismatch loss is significant unless the objective lens backfill is weak (or in other words that the beam waist is very small relative to the lens). For nonlinear signal generation, there are two further considerations: (1) dependence of the nonlinear response on the focal beam waist size, and (2) general square-law dependence of the nonlinear response on the power density. With consideration of all of these factors, the power efficiencies defined by the equations presented here should be suitable for finding the choice of lenses that gives the highest possible nonlinear signal power at the detector.

Advantages of Nonlinear Excitation over Linear Excitation

Spectroscopy is the study of material properties by interaction with electromagnetic radiation. A distinction can be made between linear excitation and nonlinear excitation methods, where linear

excitation refers to a one-photon absorption process in the material, and nonlinear excitation refers to a multi-photon absorption process.

For example, both linear and nonlinear excitation can be applied in fluorescence spectroscopy, where nonlinear (two-photon) excitation, at roughly double the linear excitation wavelength, has the following advantages: (1) clear emission window, i.e. wide separation of the fluorescence frequencies and the excitation frequency, (2) generally less damage to tissues by longer excitation wavelengths, and (3) optical sectioning.

The optical sectioning characteristic is a major benefit of nonlinear excitation for heterogeneous samples. Because one-photon (1p) absorption is linearly proportional to the optical power (ignoring saturation effects), 1p excitation occurs throughout the intersection of the excitation beam and the sample, resulting in emission throughout the entire volume. Two-photon (2p) absorption is proportional to the square of the optical power, and therefore 2p absorption is essentially confined to the focal volume. Furthermore, because of the square-law dependence on intensity, the effective focal volume of 2p absorption is reduced by a factor of 2 for Gaussian beams. With regard to the diffraction limited resolution, 2p excitation naturally has roughly double the diffracted spot size. However, the confinement effect of 2p absorption compensates exactly (for Gaussian beams) along with the added benefit of optical sectioning. Because of these reasons, nonlinear excitation significantly improves spectral measurement and imaging of heterogeneous samples.

One of the major practical applications of spectroscopy is acquisition of images with contrast based on chemical properties rather than physical structure. An illustration is shown in Figure 5, depicting the technique of scanning a sample through the beam focus to acquire two or three-dimensional image data.

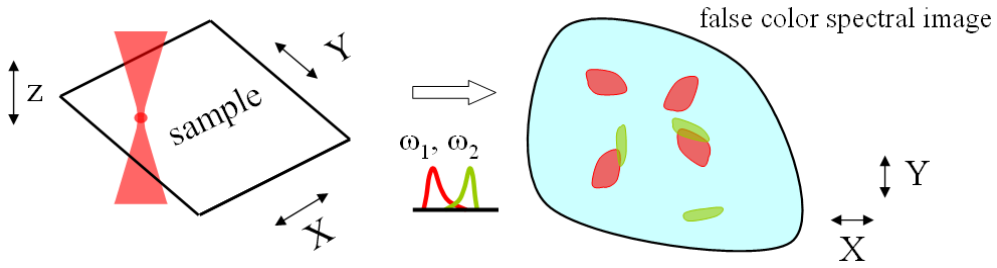

Figure 5. Illustration of frequency-selective imaging microscopy.

Frequency-selective imaging microscopy can utilize fluorescence labeling as well as label-free techniques, both of which have important uses. Fluorescence labeling is valuable for analysis of protein structures, because different branches of a large protein molecule can be stained with different fluorophores with the right chemical affinity. Fluorescent dyes with various excitation wavelengths and fluorescence spectra have been developed for this purpose, and Förster Resonance Energy Transfer measurement is an important technique that often relies on fluorescence labeling.

Label-free techniques require an intrinsic frequency-selective property, and for chemical differentiation one of the most useful intrinsic optical properties of materials is Raman scattering. The distribution of Raman resonances contains valuable information about molecular structure on scales that enable identification and differentiation of chemical species. Under linear excitation, spontaneous Raman scatter offers a relatively weak signal because it relies on the rate of decay from an excited state to a Raman energy level, a rate which is orders of magnitude less than the rate of the elastic (Rayleigh) relaxation process. Therefore, linear-excited Raman measurements require dwell times on the order of seconds to provide an adequate signal-to-noise ratio. Nonlinear excitation provides a key improvement by increasing the population rate of the Raman energy band via high intensity illumination with light at two wavelengths, whose frequency difference matches and thus drives the Raman vibrational mode. The induced polarization wave created by overlapped excitation beams can also be highly coherent, yielding a

third optical signal whose intensity is proportional to the strength of the Raman resonance and which can have temporal and spatial coherence similar to the excitation beams. This signal is generally orders of magnitude stronger than the linear-excited spontaneous Raman scatter, so the sensitivity and dynamic range requirements for optical detection are greatly reduced and the required dwell times are reduced significantly. Nonlinear Raman excitation also benefits from the same optical sectioning and other advantages of nonlinear excitation previously mentioned. With these traits, nonlinear Raman spectroscopy offers a fast, minimally invasive and label-free technique that has major benefits for biochemistry applications.

EM Theory of Nonlinear Propagation in Optical Fiber

The physical and mathematical theory of nonlinear optical effects can be found in many texts including Agrawal [14], Levenson [15], Shen [16], Sargent [17], Jackson [18] and others.

In an idealized material with the density of silica glass and body-centered cubic geometry, the distance between nearest nuclei is roughly 3.7 Å, as illustrated in Figure 6. Visible wavelengths are at least three orders of magnitude greater than the intermolecular distance, and the externally incident E field can be considered constant over any two adjacent point-like particles. Refraction and reflection at the macroscopic level can be analyzed via solutions of Maxwell's equations. In studying nonlinear propagation in optical fibers, the main non-localized phenomenon to consider is the temporal response of the medium, most importantly its dipole response in the presence of an external E field.

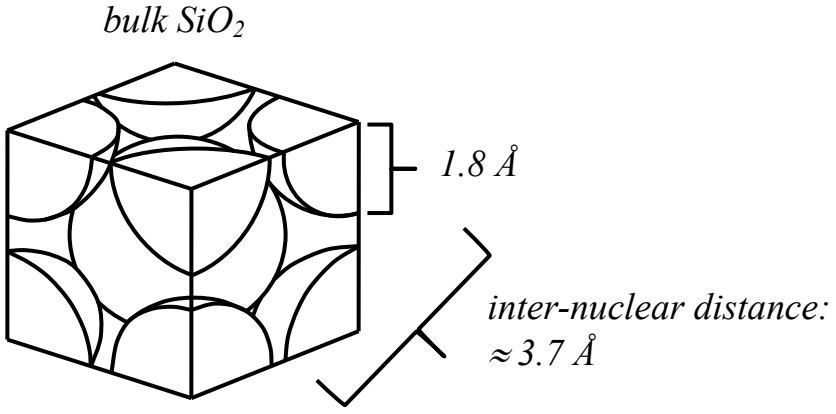

Figure 6. Illustration of atomic and optical field dimensions.

Assuming that each molecule interacts independently with the incident field, the aggregate effect is the individual response multiplied by the number of identical molecules in the system. To provide an orientation to the physical dimensions involved, the characteristics of an 806 nm pulsed fiber laser source (Imra Femtolite Ultra-100) are illustrated and detailed in Figure 7 below. [19] According to the optical lens diffraction limit, this source coupled with a 1.20 NA

lens can produce intrinsic lateral imaging resolution of 820 nm, a focal resolution area of 0.53 μm^2 and approximate peak focal intensity of 1.86 TW/cm^2.

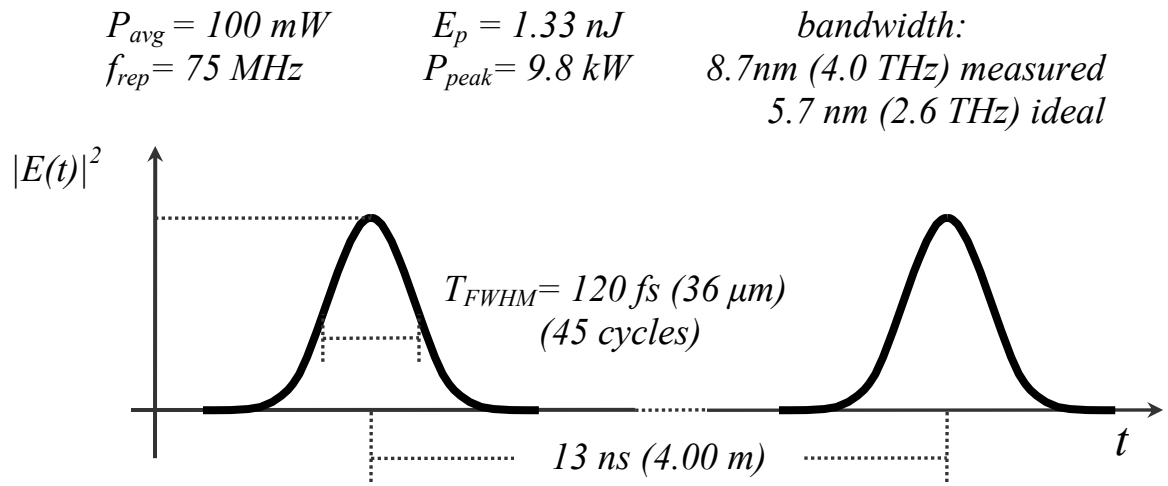

Figure 7. Characteristics of the pulsed 806 nm fiber laser.

In Figure 7, P_{avg}, E_p, f_{rep}, P_{peak}, $|E|^2$ and T_{FWHM} are the average output power, pulse energy, pulse repetition rate, pulse peak power, optical intensity and full-width at half-maximum pulse duration of the optical intensity, respectively.

Maxwell's Equations

The classical description of light is defined by Maxwell's equations. Maxwell's equations in point form are [20]

$$\nabla \times H = J + \frac{\partial D}{\partial t} \tag{12}$$

$$\nabla \cdot D = \rho_v \tag{13}$$

$$\nabla \times E = -\frac{\partial B}{\partial t} \tag{14}$$

$$\nabla \cdot B = 0 \tag{15}$$

where E and H are the vector electric and magnetic fields, and D and B are the vector electric displacement and magnetic flux density, respectively. In the absence of free charges, the charge density ρ_v and current density J are zero. The constitutive relations are

$$D = \varepsilon_0 E + P \tag{16}$$

$$B = \mu_0 H + M \tag{17}$$

where M is the magnetic polarization (zero in a nonmagnetic material such as silica glass) and P is the electric polarization of the medium. The uniform plane wave solutions of ME can be found by assuming (13) and (15) both equal zero (for free space) and assuming a phasor solution $E_x e^{j(\varpi t - kz)}$, which provides the general solution for arbitrary signals when linear superposition of Fourier modes is applied. In the phasor domain the equations become

$$\nabla \times H = j\varpi\varepsilon_0 E \tag{18}$$

$$\nabla \times E = -j\varpi\mu_0 H \tag{19}$$

Taking the curl of (19) leads to the Helmholtz equation

$$\nabla^2 E = -k^2 E \tag{20}$$

where $k = \varpi\sqrt{\mu_0\varepsilon_0}$ is the wavenumber.

Material Polarization

Polarization P is the dipole response of the charge distribution to an external E field. The propagating E field drives a polarization wave in the material that in turn contributes energy back to the propagating E field. The physical mechanism of polarization is related to the energy level transitions of bound charges in an atomic system. [15, 17] The mathematical model of polarization can be developed using a semi-classical approach in which atoms are treated as quantum mechanical systems with perturbation by a classical potential. [14-17, 20-21] The simplest case to consider is the ensemble of independent two-level systems. An undisturbed quantum system has a number of eigenstates. Introducing an interaction part of the Hamiltonian

couples the eigenstates and creates nonzero transition probabilities as a function of the energy of the driving force. This analysis is made more convenient by the dipole approximation, which assumes that the electric field does not vary significantly over the molecular diameter. The transition probability introduces a polarization response as a function of frequency in a form that can be applied in the context of the classical (Maxwell's) equations. The self-consistency of the E field during transformation between classical and quantum mechanical domains has been shown, demonstrating the validity of this approach [17]. For the independent two-level system, the natural resonance lineshape is a Lorentzian function. In a single atom with multiple transitions, the overall response can be modeled as the sum of resonances. In solids the quantum system is often too complex to tackle analytically and numeric methods are often used.[22]

Two basic models of electric susceptibility are the Lorentzian and Debye functions. [20] Each is useful for a class of materials characterized by coherently driven oscillators with a spontaneous relaxation process. The Lorentzian frequency response describes an under-damped relaxation mechanism, whereas the Debye response describes an over-damped case. The complex electric susceptibility χ relates E and P as

$$P = \varepsilon_0 \chi E \tag{21}$$

The electric susceptibility is related to the dielectric constant ε, which can be further decomposed into real ε_R part and imaginary part ε_I,

$$\varepsilon = 1 + \chi = \varepsilon_R + j\varepsilon_I \tag{22}$$

The Lorentzian function is

$$\chi(\varpi) = \frac{N q^2}{\varepsilon_0 m_e} \frac{1}{\varpi_0^2 - \varpi^2 + j\varpi\gamma_L} \tag{23}$$

where N, q, m_e are density of dipoles, electron charge (a positive quantity), and the electron mass, respectively. The resonance frequency is ϖ_0. The full width at half-maximum of the imaginary part of χ is γ_L, and it is inversely proportional to the dephasing time of the coherently driven charge oscillators. For the uniform plane wave solution that satisfies

$$\frac{d^2 E_x}{dz^2} = -k^2 E_x \tag{24}$$

where a complex valued wavenumber $jk = \alpha + j\beta$ is assumed, the attenuation and phase constants are [20]

$$\alpha = \varpi\sqrt{\mu\varepsilon_R/2}\left(\sqrt{1+\left(\frac{\varepsilon_I}{\varepsilon_R}\right)^2}-1\right)^{1/2} \tag{25}$$

$$\beta = \varpi\sqrt{\mu\varepsilon_R/2}\left(\sqrt{1+\left(\frac{\varepsilon_I}{\varepsilon_R}\right)^2}+1\right)^{1/2} \tag{26}$$

At frequencies far from resonance, the refractive index is given by

$$n \approx \sqrt{1+\mathrm{Re}\{\chi\}} \tag{27}$$

The characteristic susceptibility lineshape of the Lorentzian function is shown in Figure 8 below.

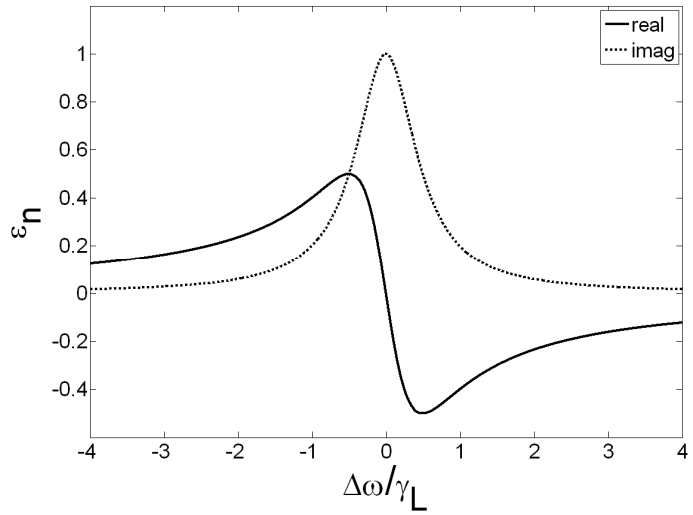

Figure 8. Lorentzian response.

Figure 8 shows the real and imaginary components of normalized permittivity ε_n which is normalized by the maximum imaginary response. The center frequency is 4.0×10^{14} rad/s and the linewidth γ_L corresponds to a characteristic time constant of 2.0×10^{9} s^{-1}. An important characteristic of the Lorentzian resonance is that dispersion crosses zero at the attenuation peak.

Unlike the Lorentzian model, the Debye model applies generally to liquids and gases. In the Debye model, dipoles slowly reach alignment with the external field to produce a bulk polarization. This alignment is continually lost through thermal interactions and there is no resonant frequency. The real and imaginary susceptibility functions are plotted in Figure 9.

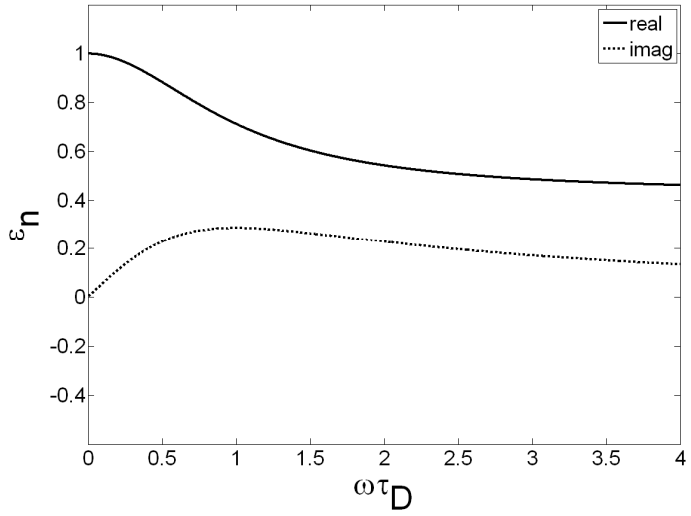

Figure 9. Debye response.

Figure 9 shows the real and imaginary components of normalized permittivity ε_n which is normalized by the maximum imaginary response. The characteristic time constant is 0.5 ns. Under the Debye model, thermal activity causes the molecules to continually lose their alignment, and as the frequency of the driving field increases, the net bulk polarization goes to zero. The Debye model is an example of an over-damped oscillator, and its frequency dependent susceptibility can be written as

$$\chi(\varpi) = \frac{N p^2}{\varepsilon_0 k_B T} \frac{1}{(1 + j\varpi\tau_D)} \tag{28}$$

where p, k_B, T are the molecular permanent dipole moment, Boltzmann's constant and temperature (K), respectively, and τ_D is the characteristic relaxation time.

Higher Order Phenomenological Susceptibility Term

At driving frequencies far from the atomic resonances, polarization can be described using the macroscopic material properties of dispersion, absorption, nonlinear refractive index and Raman scattering function. [14] The phenomenological polarization takes the form

$$P = \varepsilon_0(\chi_1 E + \chi_3 E \cdot E \cdot E + ...) \tag{29}$$

where χ_j is the j-th order susceptibility, and χ_2 is omitted because silica glass has inversion symmetry with respect to E which means $\chi_2 = -\chi_2 = 0$. The third order susceptibility is a fourth-order tensor quantity representing the nonlinear elastic scattering process. Other higher order susceptibilities are generally negligible, and cross phase mixing is generally inefficient because of the lack of phase matching conditions with coaxial propagation along a fiber. [14] Inelastic scattering processes must be considered, including stimulated Raman scattering (SRS) and Brillouin scattering. In soliton propagations, SRS is the most influential inelastic scattering process.

Electromagnetic Wave Equation

The wave equation for the propagating E field can be written as [20]

$$\nabla^2 E - \frac{1}{c^2}\frac{\partial^2}{\partial t^2} E = \mu_0 \frac{\partial^2}{\partial t^2} P \tag{30}$$

The electric field is a spatial and temporal function $E(r,t)$. In vacuum the right side of (30) is zero, in which case the phase velocity is *c* for all frequencies. This equation can be simplified by assuming propagation of an E field only in the direction of the *z* unit vector,

$$\vec{E}(r,t) = \frac{1}{2}\left(F(x,y)A(z,t)e^{(-j\omega_0 t)} + c.c. \right)\hat{x} \tag{31}$$

where c.c. is the complex conjugate and $\hat{x}$ is the directional unit vector. A quasi-monochromatic field is assumed, where A represents a slowly varying amplitude with a carrier frequency ω_0. The lateral mode profile F is independent of z and t for the case of a fundamental guided fiber mode, allowing the nonlinear and Raman responses to be applied to A only. [14] To further simplify the study of soliton effects, birefringence can be ignored which leaves only a single transverse mode of E. The polarization P under the same assumptions can be expressed as

$$\vec{P}(r,t) = \frac{1}{2}\left(Q(x,y)P(z,t)e^{(-j\varpi 0 t)} + c.c. \right)\hat{x} \tag{32}$$

The Generalized Nonlinear Schrödinger Equation (GNLSE) will be written in terms of A. The use of A rather than the full field introduces several major assumptions and approximations. Prior to studying the full nonlinear and non-localized GNLSE, the role of the susceptibility term under linear and localized conditions was explored using an optical-field level simulation. Polarization can be defined using real and imaginary relative susceptibility terms χ_R and χ_I as

$$\frac{P}{E} = \varepsilon_0\left(1 + \chi_R + j\chi_I\right) \tag{33}$$

The imaginary part χ_I affects the attenuation of the waveform while χ_R affects the phase evolution. The influence of χ_I on wave propagation was investigated using finite-difference time-domain (FDTD) computation with Lorentzian and Debye resonance models. Although the Lorentzian model is most appropriate for solids, the Debye model is useful for modeling liquids

with nonlinear responses, such as the solvent cyclohexane used in testing the CARS system. The FDTD method is especially useful in that case because optical fields of multiple wavelengths can be introduced without modification to the equations governing the polarization response.

Finite Difference Time Domain Method

The FDTD method is a discretization scheme for numerically solving coupled differential equations. [23-33] The fields in Maxwell's Equations (either E and B or D and H) can be propagated step-wise, starting with some initial state. Because they are coupled differential equations, the system can be effectively solved by evolving the electric and magnetic fields in alternating time steps. This method is full-field which means it requires time resolution on the order of the optical cycle. Because of the large time ranges involved in soliton propagation (several picoseconds), the FDTD method would present unapproachably enormous memory requirements and is therefore not useful for simulations other than very short propagating lengths, e.g. the initial pulse interactions that may occur within a few cm of propagation after entry of a nonlinear fiber. Another complication in the FDTD method is the need to initialize the propagating field with properly balanced E and H amplitudes according to the wave impedance and accounting for the half time-step difference between E and H, or otherwise arbitrary initial reflections will result. On the other hand, a major advantage of FDTD simulations is that it requires the least level of approximation and it correctly models bidirectional propagation.

Numeric data in an FDTD simulation consists of a grid of H and D sampled fields as shown in Figure 10. In this example, wave propagation is along the x direction, and the field is a 2D surface. As few as three time points are sufficient, and they can be cycled in memory.

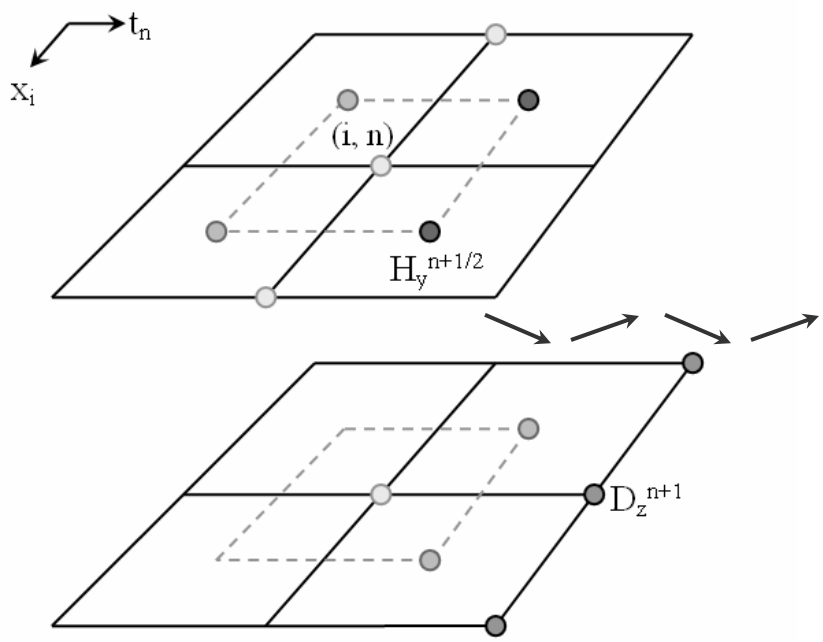

Figure 10. FDTD lattice illustration.

FDTD solution of Maxwell's Equations depends on difference equations derived from the physical system model. The numerical stability depends on the choice of forward difference, backward difference or central difference approximations of the derivative. [26] As an example, Figure 11 below shows the results of a free-space initialized pulse with unity E field amplitude after 90 fs propagation in a Debye dispersion medium. The difference equations are outlined in [26]. The Debye parameter was $\tau_D = 1/\varpi_c = 1.16$ femtoseconds. The ratio $|D_z|/|E_z|$ was approximately 2.09, or $|D_z| \approx 2.09\varepsilon_0|E_z|$. The black dot in Figure 11 represents movement from $x = 0$ with velocity of *c*, and the group index of refraction was approximately $n_g \approx 1.447$. The permittivity parameters for frequencies on resonance and far from resonance [26] were $\varepsilon_S = 2.25\varepsilon_0$ and $\varepsilon_\infty = \varepsilon_0$, respectively.

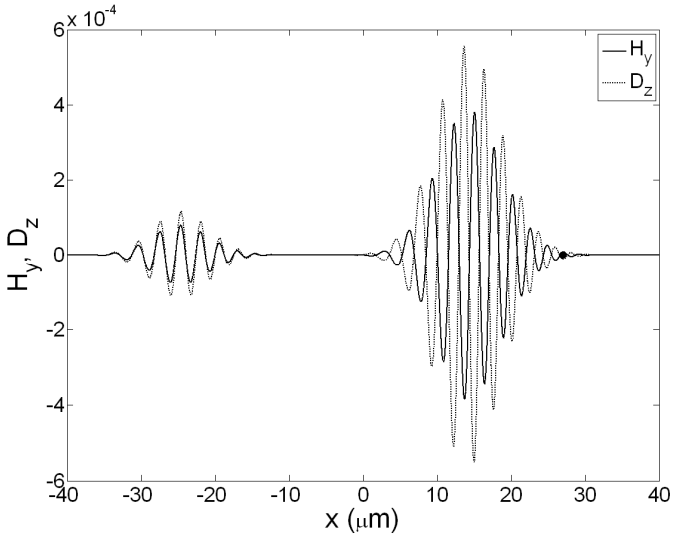

Figure 11. FDTD fields after propagation.

The following figures show comparisons of optical propagation as the resonance frequency is varied in the vicinity of a particular optical frequency. This verifies the group velocity and dispersion characteristic predicted by each resonance model. The inverse of the optical frequency is indicated by a circle in each figure.

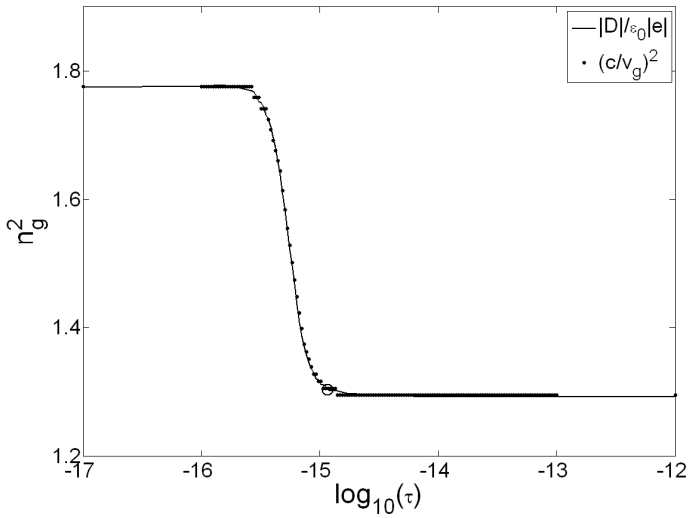

Figure 12. Varying the Lorentzian resonance frequency.

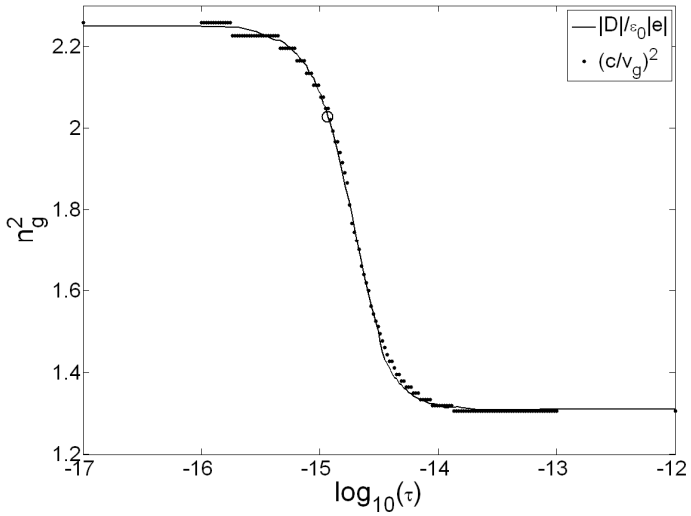

Figure 13. Varying the Debye characteristic time constant.

With the need to develop amplitude envelope-based simulations with much lower time resolution, the next sections will introduce a propagation model using the slowly-varying pulse envelope. In contrast with the FDTD method, the slowly-varying envelope approximation simplifies the inclusion of nonlinear and non-localized optical effects which are important for correctly modeling pulse propagation in optical fibers, including intensity-modulated group velocity, dispersion and Raman scattering.

Adapting Dispersion Data for the Split Step Fourier Method

A spatially uniform, monochromatic plane wave defined as

$$E(z,t) \propto \Re e\left\{ e^{j(\omega t - \beta z)} \right\} = \cos(\omega t - \beta z) \tag{34}$$

oscillates in time at a rate of $\omega / 2\pi$ (s^{-1}) at any value of z held constant. Likewise, at any fixed time t the field oscillates in space according to the propagation constant β (radians/meter). In general,

$$\beta(\omega) = n(\omega)\frac{\omega}{c} \tag{35}$$

where ω is the optical frequency (radians / second), c is the velocity of light and n is the refractive index. In free space all signal information travels with the same velocity of c (m/s). Signals generally contain frequency components bunched around a central carrier ω_0, and in this context the signal is generally a time-limited waveform that travels with an average velocity

$$v_g(\omega_0) = \left.\frac{d\omega}{d\beta}\right|_{\omega_0} \tag{36}$$

The next derivative of the propagation constant,

$$\beta_2(\omega_0) = \left.\frac{d^2\omega}{d\beta^2}\right|_{\omega_0} \tag{37}$$

is the lowest-order dispersion term. Dispersion measurement techniques generally yield values of $\beta_2(\omega_n)$, where ω_n can be varied.

Dispersion Characterization

For many bulk materials, the Sellmeier equation accurately models the refractive index at optical wavelengths, and coefficients are freely available for many materials. However, in optical fiber and other structures with waveguide propagation effects, accurate dispersion profiles can only be

obtained by measurement. There are a number of dispersion measurement techniques. The general approach is to measure relative arrival times of signals at a number of different wavelengths and to reconstruct a dispersion curve from the group velocities as illustrated in Figure 14 below.[34]

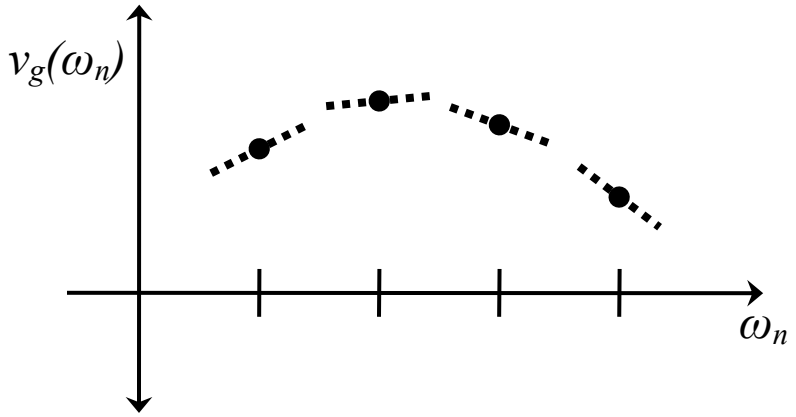

Figure 14. Group velocities measured at different frequencies.

Figure 14 is an illustration of measured group velocities, with the group velocity dispersion in the vicinity of each point indicated with slopes (dashed lines). The material's dispersion curve consists of many such slope values taken as a continuous function of frequency, which implies they must be measured in sufficiently small frequency intervals. The higher order dispersion of the material is manifested in the gradual variation of the dispersion curve as a function of frequency.

Arbitrary Dispersion in the Split Step Fourier Algorithm

Higher order dispersion in the derivation of the GNLSE is incorporated with a Taylor series expansion. [14, 35-38] This has been used to introduce one additional analytical term of higher order dispersion, which is appropriate for extending the perturbation-based equations, but it does not clearly address how those terms relate to arbitrary dispersion data covering a wide spectrum, which is required for high-power soliton spectral simulations. Because arbitrary dispersion profiles must be used for accurate representation of fibers, the measured dispersion curve must

be converted into a functional frequency-dependent propagation parameter. An explanation of this conversion could not be found elsewhere, so it is formulated here as a straightforward numeric integration of the dispersion data.

The Taylor series is a power series expansion of the frequency-dependent β parameter with coefficients from successive derivatives at a given physical frequency,

$$\beta(\omega) = \beta_0 + \beta_1(\omega - \omega_0) + \frac{1}{2}\beta_2(\omega - \omega_0)^2 + \ldots \frac{1}{k!}\beta_k(\omega - \omega_0)^k \tag{38}$$

where the Taylor series coefficients are found by derivatives,

$$\beta_k = \frac{d^k}{d^k \omega}\beta(\omega) \tag{39}$$

at the frequency ω_0. For the split step implementation, the slowly-varying envelope approximation is applied and the group velocity must vanish at some chosen frequency ω_0, i.e. $\beta_0 = \beta_1 = 0$. An obvious choice is to set ω_0 equal to the input pulse center frequency, but other choices can be made, for instance one that might reduce pulse walk-off at soliton shifted wavelengths. Because of the zero group velocity requirement, the propagation constant applied in the propagation simulations is a specialized beta function $\widetilde{\beta}$. The slope of $\widetilde{\beta}$ must be zero at the chosen zero group velocity wavelength. The function is sampled as $\widetilde{\beta}(\omega_n)$, where values of ω_n represent a uniform frequency grid over the simulation bandwidth.

The values $\widetilde{\beta}(\omega_n)$ can be calculated by two ways. The first method includes the determination of Taylor series coefficients at the given center wavelength, and the function is constructed from Taylor coefficients with omission of the group velocity term. We start with the physical

propagation constant of the material, $\beta(\omega)$. The second derivative of the Taylor expansion of $\beta(\omega)$ near ω_0 is

$$\beta''(\omega) = \beta_2 + \ldots \frac{1}{(k-2)!}\beta_k(\omega-\omega_0)^{(k-2)} \tag{40}$$

The right side of this equation can be recognized as the dispersion associated with $\beta(\omega)$, containing a constant term β_2. As previously discussed, only the value of β_2 is obtained by the measurement techniques. By generalizing to the arbitrary center frequency ω_n we have

$$\beta''(\omega) = B_2(n) + B_3(n)(\omega-\omega_n) + \frac{1}{2}B_4(n)(\omega-\omega_n)^2 + \ldots \tag{41}$$

and the coefficients, now general in n, are accordingly renamed. The lowest order dispersion term $B_2(n)$ is defined for many wavelength values ω_n, so $B_2(n)$ matches the form of dispersion data described and shown in Figure 14. Under numerical integration, values of $B_{3,4,\ldots}$ become insignificant as the frequency step approaches zero:

$$\int_{\omega_1}^{\omega_1+N\Delta\omega} \beta''(\omega)\, d\omega = \lim_{\Delta\omega\to 0}\left\{\Delta\omega \sum_{n=1}^{N} B_2(n)\right\} \tag{42}$$

If the dispersion profile is provided in the more common wavelength units such as a data set $\{\lambda_m, D_m\}$ where D_m are in units of fs/nm·m, it should be converted (by applying any necessary interpolation) to a dispersion parameter $B_2(n)$ as

$$B_2(n) = \frac{-\lambda^2}{2\pi c} D(n) \Leftarrow Interp\{\lambda_m, D_m, \omega_n\} \tag{43}$$

where $g(b) = Interp\{a, f(a), b\}$ designates interpolation of a sampled data set from reference points a to variable points b. Numerically integrating $B_2(n)$ provides the new function $B'(n)$,

$$B'(n) = \Delta\omega \sum_{j=1}^{N} \left[B_2(\omega_j) \right] \tag{44}$$

This arbitrary function $B'(n)$ can be fitted by an N-order polynomial expansion, making sure to input into the fitting algorithm a shifted axis $(\omega_n - \omega_0)$, such that

$$B'(n) = p(1) + p(k)(\omega_n - \omega_0)^{(k-1)} + \ldots p(N+1)(\omega_n - \omega_0)^{(N)} \tag{45}$$

The polynomial coefficients can be translated to Taylor series coefficients $B'_T(k)$ as

$$B'_T(k) = p(k)(k-1)! \tag{46}$$

Finally these Taylor series coefficients can be used, with omission of the lowest order term, to calculate the propagation function:

$$\widetilde{\beta}(\omega_n) = \sum_{k=2}^{N+1} \left[\frac{1}{k!} B'_T(k) \cdot (\omega_n - \omega_0)^k \right] \tag{47}$$

This method guarantees $\beta_0 = \beta_1 = 0$, and group velocity at the chosen ω_0 is zero.

The second method provides a simple formula, originating from the relationship of dispersion and propagation constant:

$$D = \frac{-\lambda}{2\pi c} \frac{d^2}{d\lambda^2} \left(\beta(\lambda) \cdot \lambda \right) \tag{48}$$

Assuming the array of M dispersion values are given as $\{\lambda_m, D_m\}$, we can define an array of numerical difference values as $\Delta X = X_{m+1} - X_m$. Then, the dispersion profile can be numerically integrated via nested cumulative sums as

$$\widetilde{I}(\omega_n) = Interp\left\{ \frac{2\pi c}{\lambda_{m''}}, \sum_{m'=1}^{m''} \left[\sum_{m=1}^{m'} \left[\frac{1}{\lambda_m} D_m \Delta\lambda \right] \Delta\lambda \right] \cdot \left(\frac{-2\pi c}{\lambda_{m''}} \right), \omega_n \right\} \tag{49}$$

From this result, the propagation function can be calculated as

$$\widetilde{\beta}(\omega_n) = \widetilde{I}(\omega_n) - \widetilde{I}'(\omega_0) \cdot (\omega_n - \omega_0) \tag{50}$$

where $\tilde{I}'(\omega_0)$ represents a group velocity,

$$\tilde{I}'(\omega_0) = \left.\frac{\Delta\tilde{I}(\omega_n)}{\Delta\omega_n}\right|_{\omega_n = \omega_0} \tag{51}$$

Examples of $\tilde{\beta}(\omega_n)$ are given for two profiles in Figure 15 and Figure 16. In the first example, dispersion of D=1.0 fs/nm·m at 806 nm is held constant with respect to frequency, resulting in a sloping graph when shown on a wavelength axis. The second profile shows the dispersion curve of NL-PM-750 fiber (CrystalFibre).

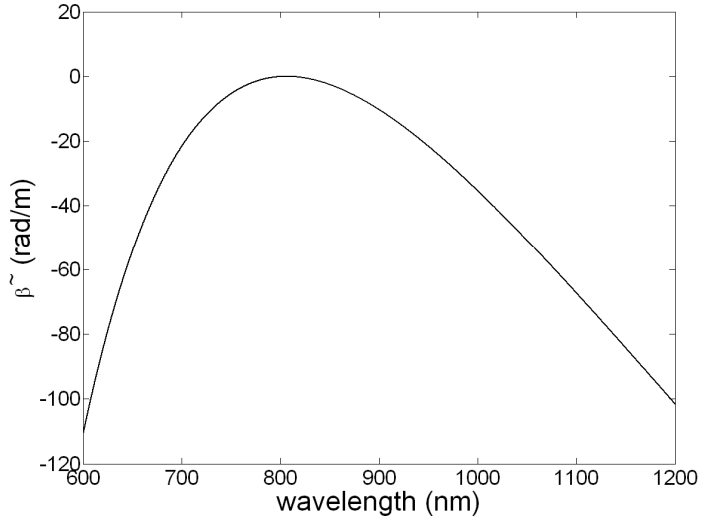

Figure 15. Propagation function for zero v_g at 806 nm (D = 1 fs/nm•m at 806 nm).

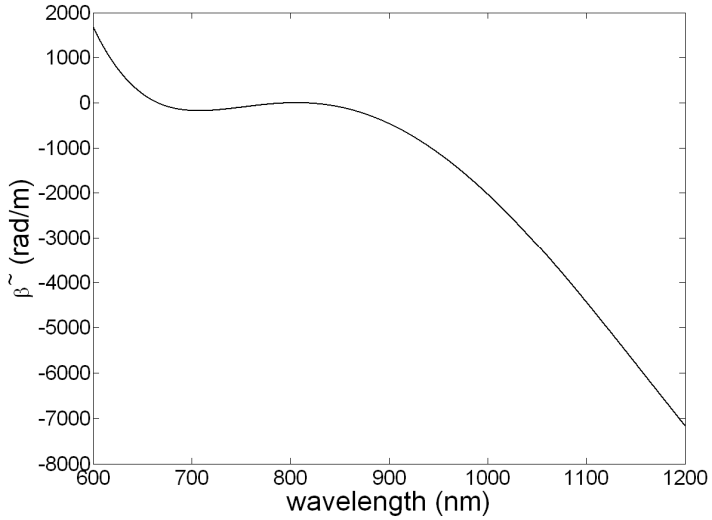

Figure 16. Propagation function for zero v_g at 806 nm (NL-PM-750).

The group velocity and dispersion produced by these propagation parameters was used for split-step numeric simulations described in the following sections. In wavelength regions outside the available data, the functions were linearly extrapolated.

II. Numeric Solution of Generalized Nonlinear Schrödinger Equation

The principal requirements for wavelength tuning of soliton pulses for use as a tunable-frequency output are: (1) the maximum wavelength of the longest-wavelength shifted soliton, and (2) the free spectral range not occupied by higher order solitons as the input power is varied.

The detailed theory of optical soliton propagation has been developed in prior works [14, 37-46]. However, previously the goal has been to develop analytical derivations of solutions of the higher-order solitons under various nonlinear responses, and to obtain perturbation based results for signaling by soliton pulse transmission and for estimating signal degradation by nonlinear effects. These results are applicable to long-haul optical fibers with relatively low input pulse power, but their assumptions are violated when the input power is significantly higher. More recently, studies of wavelengths shift over wider wavelengths have been developed [14, 45-46], but none of these studies address the details most relevant to wavelength tuning simulations, and none can be used to obtain further results without creating new numerical algorithms. Central to our numeric investigations are: (1) predicting absolute and relative wavelength shift of the first and second wavelength shifted solitons as a function of the coupled input power, (2) fine-grained parameterized study of entry-point and end-point dispersion level and slope, pulsewidth and other critical parameters, and (3) computational stability without dependence on parameter variations. As the results in the following sections demonstrate, the existing results are helpful, but they are not directly applicable to predicting the wavelength-shifting behavior of specialty fibers with soliton-like pulsed inputs with very high power.

In order to elucidate the fundamental processes, the following sections discuss existing perturbation based results and clearly delineate their applicability towards modeling soliton wavelength shift. Sources of numerical instability effects are discussed, and the full numerical

simulations are detailed. Results of simulations of various wavelength shifting characteristics are presented. The key findings of the following soliton investigations are:

(I) A previously known expression of Raman induced frequency shift is based on the energy-conserving first-order perturbation of the propagation equation, and it is correct for the $N=1$ soliton in the vicinity of the originating wavelength. However, because of the contributions of other nonlinear effects, it cannot be solely relied on to predict the net soliton wavelength shift for a short fiber with high input power. Another previously known expression, based on the method of moments, is also limited because of the perturbation assumption. In numerical simulations, the linear Raman approximation, with induced frequency chirp and self phase modulation, is accurate in predicting the net wavelength shift of the fundamental soliton, but it does not correctly reproduce the experimentally observed higher-order solitons. The most accurate numerical approach is to apply an un-simplified Raman response function, even when the input pulse width is not less than the accepted limits on the applicability of the linear Raman approximation [47].

(II) Propagation under high input power, identified as input power satisfying $N>>1$ soliton conditions, involves the complicated interaction of arbitrary dispersion and self phase modulation acting together with Raman scatter and optical shock, to produce a broad and highly varied output spectrum. These effects were separately simulated in order to determine their contributions and combined effects. As discussed in the following sections, the optical shock term introduces numerical instability because it tends to produce physically unrealistic pulse peaks unless its steepening effect dispersion is otherwise mitigated. Because the simulation spectrum covers an extremely wide bandwidth, aliased signal suppression and recreation of the wavelength-dependent waveguide losses must also be considered.

(III) The desired wavelength shifting attributes are constrained by the dispersion profile. A lower absolute value of dispersion at the entry wavelength produces wider eventual wavelength shift because of the comparatively higher soliton *N* value. On the other hand, below a critical margin, lack of sufficient dispersion facilitates generation of a supercontinuum or near-supercontinuum, which are not useful for wavelength shifting of pulses. Meanwhile, in the long-wavelength edge of the anomalous dispersion range of a fiber, the diminishing dispersion limits the maximum attainable wavelength shift. Parameterized variations of entry point dispersion level and slope, presented in the following sections, were useful in choosing the proper input wavelength for a given fiber.

(IV) As gauged by the comparisons of simulations with experimental measurements, secondary solitons demonstrate a behavior roughly similar to a power-scaled fundamental soliton. If the input power exceeds the *N=1* condition, an initial pulse-breakup event occurs upon fiber entry, and pulses of different wavelengths separate temporally due to dispersion. Thereafter, they may acquire new integer-*N* soliton pulse shapes and behave independently of other components, especially as fundamental *N=1* solitons. However, under appropriate circumstances, higher order solitons may propagate without losing coherence, and their spectrum evolves much differently as a result.

Soliton Solutions of the GNLSE

The equation for wave propagation in a nonlinear medium takes the form of the generalized nonlinear Schrödinger equation (GNLSE). There is a set of analytic solutions to the GNLSE known as soliton solutions. Solitons remain stable under an exact balance of anomalous dispersion, which is a linear response of the material and waveguide effects, and ordinary dispersion which is induced by a nonlinear response. To remain stable means that solitons

maintain their temporal and spectral shape during propagation, and moreover, under perturbation, soliton-like waveforms tend to converge to the nearest soliton solution. The detailed analysis of solitons can be found in various publications. [14, 37-45] The nonlinear response of silica is very weak, so solitons in the optical fiber guided mode are supported only when the peak power is sufficiently high. Because of the power limitation of various lasers, soliton pulses are usually very short (less than 1 ps for typical fiber lasers).

To keep the notation conventional and consistent with the previous sections, the GNLSE will be written in terms of $A(z,t)$, which is the slowly-varying complex amplitude envelope component of the full E field:

$$\vec{E}(r,t) = \frac{1}{2}\hat{x}\,F(x,y,t)A(z,t)e^{j\omega_0 t} + c.c. \tag{52}$$

The Fourier transform (FT) of $A(z,t)$ is defined as [14]

$$\tilde{A}(z,\Omega-\omega_0) = \int_{-\infty}^{\infty} A(z,t)\,e^{j\omega t}\,dt \tag{53}$$

where ω_0 is the carrier frequency and Ω is the optical frequency, and a frequency shift $\omega = \Omega - \omega_0$ is made. This may seem to be an unusual definition of the Fourier transform because the sign of the exponent is positive. It results from a choice to represent the positive frequency side of the full spectrum $\vec{E}(z,\Omega)$ using $\tilde{A}(z,\omega)$. This provides a positive sign orientation of the frequency variable in $\tilde{A}(z,\omega)$. The impact of this in the numerical algorithm is simply that the Fast Fourier Transform (FFT) and Inverse Fast Fourier Transform (IFFT) must be exchanged with each other.

The Nonlinear Schrödinger Equation

The mathematical treatment of solitons is based on exact and approximate solutions to the GNLSE. Some terms related to the material's optical response, especially the Raman response, will prevent analytical solution. The GNLSE is a complete model for light propagation, and solitons are one example of steady solutions that can occur. Because solitons comprise a class of analytic solutions of the GNLSE, they are an important starting point for analyzing nonlinear propagation effects. The goal of the numerical GNLSE simulations made in this work is to predict the wavelength shifting behavior of highly nonlinear photonic crystal fiber (PCF). Achieving large wavelength shifts in relatively short PCFs requires high input power which entails complex higher order behavior going beyond the analytic soliton solutions of the GNLSE, especially the Raman response. Therefore, numerical simulations are necessary for investigating the complex interactions of the GNLSE terms in the realm of very high input power.

The wave equation as written in (30) applies to localized, linear media. Non-local and nonlinear responses can be incorporated with the following formulation:

$$\frac{\partial^2}{\partial z^2}E(z,t)-\frac{1}{c^2}\frac{\partial^2 D(z,t)}{\partial t^2}=\frac{4\pi}{c^2}\frac{\partial^2 P(z,t)}{\partial t^2} \tag{54}$$

where D is the linear induced field and P is the third order polarization. [43] The latter terms can be defined as

$$D(z,t)=\int \varepsilon(\tau)E(z,t-\tau)d\tau \tag{55}$$

$$P(z,t)=E(z,t)\int R(\tau)\left|E(z,t-\tau)\right|^2 d\tau \tag{56}$$

where ε is the linear complex permittivity and R is the nonlinear response. Here, the function R contains an impulse at $\tau=0$ that describes the instantaneous response and a Raman characteristic response over values $\tau>0$. Some terms in (54) involving the transverse coordinates are omitted

for simplicity. Only the average of the mode profile is considered, although the effective mode area is used in calculating the nonlinear gain.

A frequency domain expression of the wave equation can be found by taking the Fourier transform of (54). It can be expressed in terms of the complex envelope $\widetilde{A}(z,\omega)$ under the slowly varying envelope approximation. Ignoring the wavelength dependence of the mode area, it can be expressed as [43]

$$\begin{aligned}&\frac{\partial\widetilde{A}}{\partial z}-i\big(k(\omega)-k_0\big)\widetilde{A}=\frac{i2\pi}{cn_{eff}(\omega)}\omega_0\left(1+\frac{\omega}{\omega_0}\right)\times\\&\iint\left(\widetilde{A}(z,\omega')\widetilde{A}(z,\omega'')\widetilde{A}^*(z,\omega'+\omega''-\omega)\chi^3\times\big(\omega-\omega'\big)\right)d\omega'\,d\omega''\end{aligned}\tag{57}$$

For a short span of fiber, the attenuation is very small so it may often be omitted. The uniform group velocity component β_1 can be omitted because it does not affect the spectral evolution. The time domain equation can then be written as [14]

$$\frac{\partial A}{\partial z}+\frac{i\beta_2}{2}\frac{\partial^2 A}{\partial t^2}-\frac{\beta_3}{6}\frac{\partial^3 A}{\partial t^3}=i\gamma A(z,t)\int_0^\infty R(\tau)\big|A(z,t-\tau)\big|^2 d\tau\tag{58}$$

This version of the GNLSE includes the second expansion of dispersion and a convolution term for the non-localized Raman response. To provide a frequency dependence of the nonlinear response, the constant γ will be replaced with $\gamma=\left(\gamma_0+i\gamma_1\frac{\partial}{\partial t}\right)$. This introduces a first-order Taylor expansion of the nonlinear parameter. The γ_1 term is the optical shock, or self steepening of the pulse. The optical shock term represents intensity-dependent group dispersion. Due to the Kerr response, energy converges towards the trailing edge of the pulse and the pulse tends to become saw tooth-shaped. [39] The self-steepening effect plays a role in soliton breakup. It interferes with the coherence of the soliton, allowing new lower-order solitons to form. It also

temporally stretches the pulse, leading to a reduction of the Raman energy conversion. The optical shock term can limitlessly sharpen the pulse temporal profile which may then develop non-physical features. Under realistic conditions this never happens because dispersion prevents this non-physical 'breaking wave' effect. On the other hand, it does cause a problem in simulations as unlimited steepening results in numeric instability. This problem can be solved, when using the Raman time-domain response in the nonlinear model, by reducing or eliminating the instantaneous component represented by the $\delta(t)$ component. Another way to prevent instability from the shock term is to artificially increase the magnitude of dispersion compared to the fiber parameters.

When higher-order dispersion and attenuation parameters are ignored and γ is time-independent, the GNLSE reduces to a simple form that still supports soliton solutions,

$$\frac{\partial A}{\partial z} + i\frac{\beta_2}{2}\frac{\partial^2 A}{\partial t^2} = i\gamma|A|^2 A \tag{59}$$

Nonlinear-propagating pulses are usually hyperbolic secant or Gaussian in their temporal profile. To the extent that the initial pulse shape $A(t)$ is soliton-like, propagation of the field amplitude according to (59) results in soliton-like behavior such as preservation of the pulsewidth and periodicity. Although the two types of pulses are similar, the hyperbolic secant (sech) function is an exact soliton solution, whereas the Gaussian function most often describes the output of a pulsed laser. Both types of pulse are characterized by their central frequency, pulse width and a chirp parameter, C. The pulse chirp, if nonzero, represents quadratic phase modulation over the span of the pulse. The Gaussian initial pulse is

$$A(0,t) = \sqrt{P_0} e\left(-(1+iC)\frac{t^2}{2\tau_0^2} \right) \tag{60}$$

The dispersion-induced pulsewidth for a Gaussian pulse at distance z with a single dispersion parameter β_2 (negative or positive) and initial pulse width τ_0 is

$$\tau(z) = \tau_0 \sqrt{1 + \left(\frac{\beta_2 z}{\tau_0^2} \right)^2} \tag{61}$$

As laser amplifying cavities always have some dispersion, dispersion compensation is required. Pre-chirp of the laser pulse in a PCF can be detrimental for two reasons: 1) the stretched pulse has lower peak power and therefore weaker nonlinear induced phase shift, and 2) the efficiency of the Raman induced self frequency shift (SSFS) is less because of the narrower instantaneous bandwidth of the pulse.

Solutions of (59) known as fundamental soliton solutions have been found using a technique called the inverse scattering method [48]. Solution of the nonlinear Schrödinger equation via the inverse scattering method is a highly rigorous endeavor. The simplest analytic solution of the GNLSE is the $N = 1$ or *fundamental* soliton, which is a sech function for all propagated distances. The first order solution can be derived by induction from the GNLSE, without resorting to the inverse scattering method [35]. The integer order N of a soliton refers to numbered solutions that occur for peak powers obeying $P_0 \propto N^2$. All solitons with $N > 1$ are spatially periodic. As the simulations in following sections show, for $N = 2,3,...$ the temporal and spectral traces evolve into complex patterns and return to the initial sech profile at each multiple of the soliton period, z_0. If the power does not exactly match a soliton order, the dispersion will

not be balanced and the soliton may gradually disperse. If the residual energy at any point matches the soliton conditions, a lower-order soliton may form.

Soliton Conditions

For soliton propagation, the transmitting medium must have anomalous dispersion in the linear regime which is compensated by nonlinearity-induced normal dispersion (e.g. the Kerr response). The conditions for propagation of any *Nth* order soliton governed by the simplified GNLSE (59) can be defined by just a few equations. The nonlinear parameter γ is [14]

$$\gamma = \frac{n_2 \omega_0}{c A_{eff}} \qquad (W^{-1} m^{-1}) \tag{62}$$

where n_2 is the nonlinear refractive index, and A_{eff} is the effective cross section area associated with the transverse mode profile. The nonlinear index is defined as [49]

$$n = n_0 + n_2 \frac{1}{2} |E|^2 \tag{63}$$

The constraint for the *Nth* soliton solution is given by [14, 49]

$$N = \sqrt{\frac{\gamma P_0 \tau_0^2}{|\beta_2|}} \tag{64}$$

where P_0 is the pulse peak power and τ_0 is the pulse width, measured as the half-width of the intensity at the $P_0 / \exp(1)$ level. The dispersion term β_2 is a negative value for optical fibers, indicating that the dispersion is anomalous. For a Gaussian pulse, the full width at half maximum (FWHM) pulse width is related to τ_0 as $T_{fwhm} = 2\sqrt{\ln(2)} \cdot \tau_0$. The soliton period is given by [14]

$$z_0 = \frac{\pi}{2} \frac{\tau_0^2}{|\beta_2|} \qquad (m) \tag{65}$$

For solitons generated by an 806 nm, 120 femtosecond pulsed laser in a PCF of the type NL-PM-750, z_0 is on the order of 1 m.

First Order Soliton Solution

The first-order ordinary hyperbolic secant soliton solution has the time-domain expression [14]

$$A(z,t) = \sqrt{\frac{E}{2\tau_0}} sech\left(\frac{t-T_C}{\tau_0}\right) \exp\left(-j\Omega_R(t-T_C) - j\frac{C(t-T_C)^2}{2{\tau_0}^2}\right) \tag{66}$$

where $E, T_C, \tau_0, \Omega_R, C$ are the pulse energy, position, pulse width, Raman induced frequency shift and the chirp parameter, respectively. This form introduces soliton parameters used by the moments equations in the following section. For the sech pulse, the pulse width relationships is $T_{fwhm} = 2\ln\left(1+\sqrt{2}\right)\cdot\tau_0$.

Moments Equations

The $N=1$ soliton is useful because it maintains the sech profile during propagation. Physically, we expect that the pulse shape will preserve itself under small perturbations such as dispersion-induced chirp, Raman loss-induced frequency shift and attenuation loss. Like sech pulses, Gaussian pulses can also have a stable pulse shape when propagating, e.g. in dispersion managed fiber links. We might ask how the soliton pulse behaves to a first order approximation under perturbations. In perturbation theory, variation of parameters is a well known technique for solving systems of differential equations for which the corresponding homogeneous equation solution is known. However, the propagating soliton pulse loses energy as it propagates, violating the basis for the variation method. Because of this problem, the method of moments proves to be a more useful approach. [50-54] The pulse whose amplitude satisfies the GNLSE can be treated as a particle which has the following parameters: [54]

$$E = \int_{-\infty}^{\infty} |A|^2 \, dt \tag{67}$$

$$T_C = \frac{1}{E} \int_{-\infty}^{\infty} t \, |A|^2 \, dt \tag{68}$$

$$\Omega_R = \frac{i}{2E} \int_{-\infty}^{\infty} \left(A^* \frac{\partial}{\partial t} A - A \frac{\partial}{\partial t} A^* \right) dt \tag{69}$$

where E is the pulse energy, T_C is the relative pulse walk-off and Ω_R is the Raman induced frequency shift (RIFS). The equations apply for the first order soliton as long as the pulse shape is preserved. The above equations can be differentiated with respect to the distance variable to find general solutions, and explicit forms can be found for Gaussian or sech pulses. The moments equations were derived in previous works [50-54], but details of the derivations were not given. Therefore, solutions for (67,68) are worked out in the appendix.

Calculation and Simulation of Moments Behavior of N=1 Soliton

The spectra obtained under high input power conditions depend on individual effects that can be analyzed using the lower power $N = 1$ soliton. For instance, the level of Raman induced frequency shift (RIFS) has a physical origin in the measured Raman gain of silica. To validate the Raman model, simulations were made over a propagation span $(100\, z_o)$ which is a relatively long distance compared to the length of fibers used in the CARS system, which is described in detail later. The evolving Raman shifted soliton spectrum is shown in Figure 18. In that simulation, a uniform dispersion of 15 fs/nm•m (at 806 nm) was assumed and the input pulse was a 120 femtosecond pulse at 806 nm with input coupled power level corresponding to the soliton condition $N = 1$. This simulation was based on the GNLSE without the optical shock term, zero attenuation and with the linear approximation of the Raman response. A white line over the image represents the Raman spectral shift evaluated by the moments equations. The

comparison verifies that the Raman shift realized in the SSFS simulation matches closely to that predicted by the moments equations and the underlying physical origin of Raman temporal response.

For virtually all solitons in optical fiber, there tends to be a characteristic reduction in the rate of Raman shift versus propagation distance. The spectral evolution shown in Figure 18 exhibits this feature, although the magnitude of reduction is not significant because the power is relatively low. According to the GNLSE theory [14], the reduction of the Raman self-induced frequency shift is explained by the gradual chirping of the fundamental soliton. As the pulse becomes chirped, the efficiency of the Raman shift decreases. This can be explained by the Raman gain spectrum of silica. The Raman gain increases with frequency in a roughly linear fashion from 0 cm^{-1} to about 400 cm^{-1}, which means that the gain between individual frequency components is reduced when the pulse instantaneous bandwidth is narrowed because of dispersion induced stretch. Pulse chirp cannot increase without limit, however. Eventually, the accumulated chirp will deform the temporal profile until it begins to deviate from the sech form. If this excess chirp is treated as a small perturbation, then it should be halted from increasing because of the soliton equilibrium. Meanwhile, there may be another explanation for the gradual lessening of the self-induced frequency shift because the energy of the soliton pulse will change during propagation due to the red shift. Wavelength change via RIFS causes photon energy loss as photons at a higher energy are absorbed and photons of lower energy are emitted. Other dissipative processes can also occur, including absorption and scattering. Because of the soliton constraint equation (64), any gradual reduction of power resulting from the red shift and attenuation processes should be accompanied by increasing pulse width. However, supposing that the soliton condition is no longer met because of the RIFS and attenuation, the pulse should be squeezed because of

the anomalous dispersion. For the NL-750-PM fiber, dispersion is anomalous out to the 1200 nm wavelength mark. Considering a pulse that propagates down the fiber while its wavelength gradually becomes longer, the nonlinear induced dispersion will diminish because of decreasing peak power from accumulated loss associated with the red-shift and reduced waveguide confinement of the mode profile inside the fiber core. Under these conditions, the self-balancing soliton equilibrium effect should result in the pulse width becoming increasingly squeezed. To test this reasoning with actual measurements, the fundamental soliton output pulse widths from the NL-PM-750 fiber were measured using an SHG autocorrelator (Femtochrome). The results, shown in Figure 17, confirm that the fundamental soliton pulse width did decrease with wavelength shift of 100-300 nm in a 2.5 m length of NL-PM-750 fiber. The input pulse width was 125±5 fs (fwhm) , and the wavelength shift was obtained by increasing the input coupled power of the 806 nm pulse.

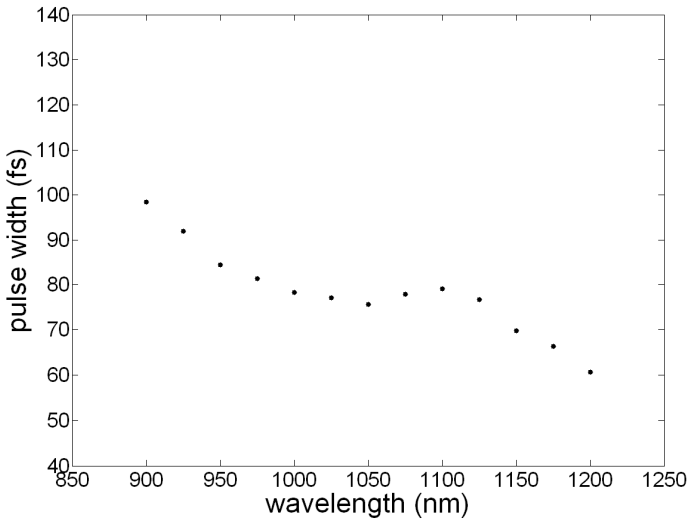

Figure 17. Pulse widths of wavelength-shifted soliton (measured).

Naturally, as the pulse shortens, its bandwidth widens and the dispersion experienced by the pulse increases. The data shown in Figure 17 suggest that the pulse chirp remained small. The

final pulse width and pulse chirp will depend on the particular properties of the fiber and input laser.

Because the moments equations are not applicable for large input powers, numerical analysis must be used for high input power ($N >> 1$). Still, all results should be in agreement in the low-power regime. To make the comparison with the Split-Step Fourier Method (SSFM) as straightforward as possible, the β_3 term can be omitted and initial chirp can be set to zero. In that case, the set of moments equations for the first order sech soliton (based on results of [54]) is

$$\frac{dE}{dz} = -\alpha E \tag{70}$$

$$\frac{dT_c}{dz} = \beta_2 \Omega_R \tag{71}$$

$$\frac{d\tau}{dz} = \frac{\beta_2 C}{\tau} \tag{72}$$

$$\frac{dC}{dz} = \left(\frac{4}{\pi^2} + C^2 \right) \frac{\beta_2}{\tau^2} + \frac{2\bar{\gamma}E}{\pi^2 \tau} + \frac{12\beta_2 \Omega_R^2}{\pi^2} + \frac{24\bar{\gamma}E}{\pi^2 \varpi_0 \tau} \tag{73}$$

$$\frac{d\Omega_R}{dz} = -\frac{4T_R \bar{\gamma}E}{15\tau^3} + \frac{\bar{\gamma}EC}{3\varpi_0 \tau^3} \tag{74}$$

Considering the length of fibers used in wavelength shifting applications, attenuation should not be significant and the soliton conditions (pulse width and peak power, nonlinear parameter and dispersion) should not necessarily vary over the course of propagation. As previously discussed, the impact of induced pulse chirp is uncertain but seems to have a major role in wavelength shifting behavior according to the GNLSE and moments equations. The moments equations predicted a significant degree of induced chirp in the presence of Raman shift, but this prediction is not consistent with the actual measurements of wavelength shifted soliton pulses. The moments equations allow unlimited growth of the induced chirp, which is not realistic. To test the degree of induced chirp in simulations of the GNLSE as compared to the moments prediction, a simulation was done using 120 femtosecond fundamental soliton pulses at 806 nm

in dispersion of 15 fs/nm·m at 806 nm, with the result that the pulse width after a distance of $10z_0$ was 139.8 fs. The soliton period in this case was $z_0 = 1.406\,m$. The results of these simulations are plotted with overlays of the moments equations (dashed lines) in the following figures. The comparison of traces in Figure 18 shows that the magnitude of Raman induced frequency shift (RIFS) predicted by the moments equations agrees with the simulation. However, the initial rate of chirp increase is approximately -0.344 km^{-1} and this value grows rapidly with distance. A value of the rate of chirp increase that most closely reproduces the simulated RIFS is a constant rate of chirp increase of -0.05 km^{-1}. Nevertheless, when this value was used, the final pulse width from moments equations was 174 fs, which is larger than the simulation result, suggesting that the induced chirp in simulations and in the moments equations did not precisely match. As discussed, there may be alternate explanations for the gradual diminishing of RIFS.

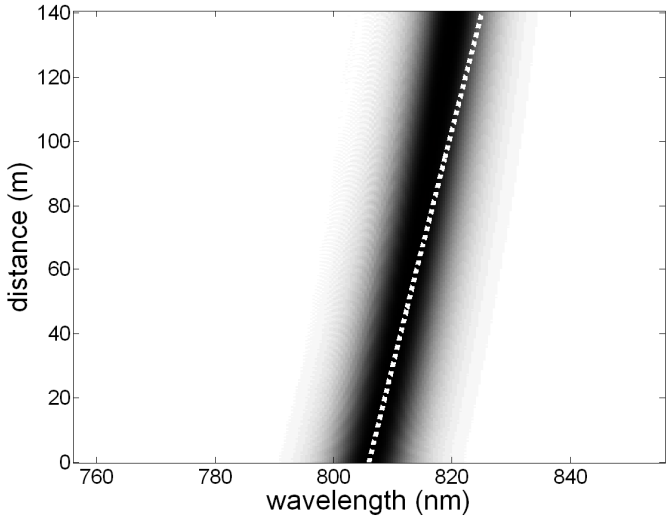

Figure 18. Moments equation trace (white) over simulation (black).

According to the differences in the frequency plot of Figure 18 between simulated RIFS (black) and the moments equations prediction (white dotted line), the time domain characteristics should also be slightly different between the two. This was confirmed as shown in Figure 19, which

shows the corresponding time domain traces for simulation (solid) and moments equations (dashed).

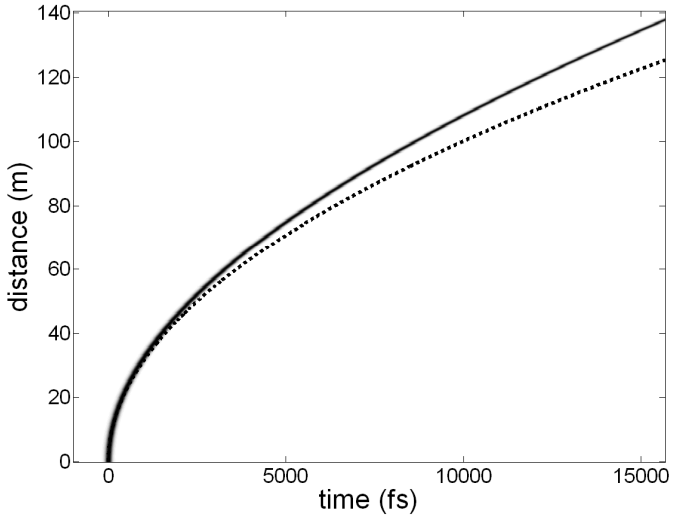

Figure 19. Pulse walk-off prediction over simulation.
(solid line: results of numerical simulation, dashed line: from moment equations)

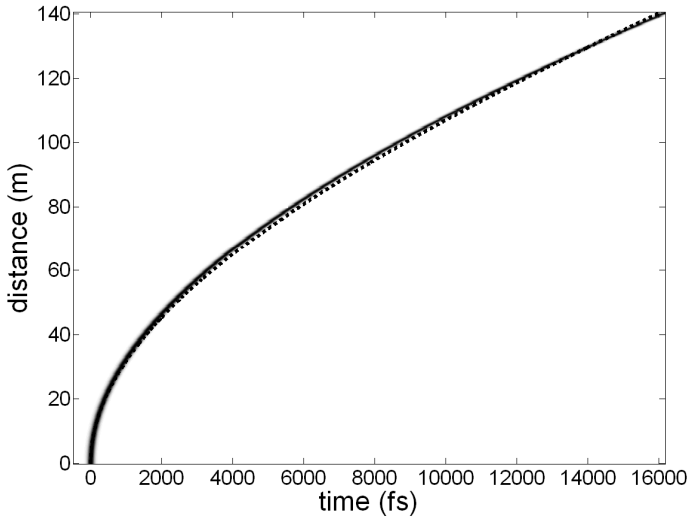

Figure 20. Fixed loss parameter fitted to simulation results.
(solid line: results of numerical simulation, dashed line: from moment equations)

Fundamentally, the moments equations predict that the history of an input soliton affects its eventual state. The RIFS term contributes to the pulse chirp rate of change. According to these simulations, it seems that the moments prediction is only accurate while the induced chirp

remains relatively small. There are two gradual loss mechanisms: (1) material attenuation and (2) photon energy loss via RIFS as absorbed photons of higher energy are converted through Raman scattering to emitted photons of lower energy. We can introduce a gradual loss term based on the photon energy transition to obtain a reduction of RIFS spectrally similar to induced chirp, but tied to the mechanism of RIFS. Such an approach has been previously introduced [55]. With a fixed loss term, a good match to the simulations was obtained, as shown in Figure 20. Using this method, the final pulse width is not overestimated. RIFS-based moments equations were investigated in [55], but it should be noted that a fiber-dependent parameter was always necessary to calibrate the RIFS characteristic. This may be necessary to account for frequency dependent nonlinear gain and birefringence. To proceed with the investigations of soliton propagation, the numerical algorithms used to calculate solutions of the GNLSE will be detailed next.

Split Step Fourier Algorithm

The split step Fourier algorithm simplifies the numerical solution of the GNLSE, and it reduces the computation time by allowing use of the Fourier Transform [56]. It is useful to separate the GNLSE equation into a linear dispersion and attenuation operator $\hat{D}$, which includes the terms that describe the material and waveguide dispersion and attenuation, and a nonlinear operator $\hat{N}$ which describes the Raman and other nonlinear responses: [56]

$$\frac{\partial A}{\partial z} = (\hat{D} + \hat{N})A \tag{75}$$

The split step method involves a time sampled trace of the complex waveform A. The formal (analytic) and numeric representations of the operators will be distinguished as $\hat{D}, \hat{N}$ and $\hat{D}, \hat{N}$ respectively. In the split-step approximation, the effects of dispersion-induced phase shift and attenuation can be applied separately from the nonlinear-induced phase shift as long as the time

step is small enough that the local error remains small. The limits on error in the SSFM have previously been studied in detail [57], and for many purposes a limiting criteria such as a maximum induced phase shift of $\pi/10$ within each step can be assumed. Improvements to the static phase shift criteria are mostly useful for long-haul simulations in which the nonlinear induced phase shift varies greatly over the distance of the fiber. The fiber spans involved with this work were so short that the static phase criterion still allowed acceptable throughput. A step-back variable step size technique was used to improve efficiency, as described later.

Most importantly, separation of the GNLSE into the dispersion and nonlinear operators simplifies evaluation because dispersion can be applied in the frequency domain while the nonlinear response can be calculated in the time domain. The general form of the SSFM, using a trapezoidal approximation for the nonlinear operator $\hat{N}$, is

$$A^{+} = fft\left\{\hat{D}\cdot ifft\left\{e^{j\Delta z\gamma\left(\frac{\hat{N}^{\oplus}+\hat{N}}{2}\right)}\cdot A\right\}\right\} \tag{76}$$

where $A = A(z,t)$ is the slowly varying field and $A^{+} = A(z+\Delta z,t)$ is the field at the next time step. The operations $fft, ifft$ represent the numeric Fast Fourier Transform (FFT) and the inverse (IFFT). The operators are given by

$$\hat{D} = fft\left\{e^{\Delta z\left(j\,\tilde{\beta}(\varpi)-\frac{\alpha(\varpi)}{2}\right)}\right\} \tag{77}$$

$$\hat{N} = |A|^2 + \frac{2j}{\varpi_0 A}\frac{\partial}{\partial t}|A|^2 A - T_R\frac{\partial}{\partial t}|A|^2 \tag{78}$$

$$\hat{N}^{\oplus} = \left|A^{\oplus}\right|^2 + \frac{2j}{\varpi_0 A^{+}}\frac{\partial}{\partial t}\left|A^{\oplus}\right|^2 A^{\oplus} - T_R\frac{\partial}{\partial t}\left|A^{\oplus}\right|^2 \tag{79}$$

The predictive $\hat{N}^{\oplus}$ is initialized to $\hat{N}$ and then recursively updated. It is updated several times using the prediction $A^{\oplus}$, which is also recursively updated. This improves the accuracy of the nonlinear operator term according to the trapezoidal approximation. The implementation of (76) is known as the symmetric-SSFM. The nonlinear operator is placed halfway between two dispersion steps of half distance to reduce the error. Combining adjacent iterations, dispersion can be applied in whole steps throughout the propagating length except for the very first and very last steps. Therefore, the symmetric SSFM implementation is nearly identical to the ordinary SSFM algorithm.

Choosing the SSFM Center Frequency for Simulation

Establishing SSFM parameters requires the assignment of a suitable FFT size n, generally $n = 2^{9\sim15}$ in this work. A portion of the optical spectrum is represented in the SSFM simulation by baseband complex variable A. The optical wavelength represented by the DC component is generally chosen to be the wavelength of the input laser, although this does not have to be the case, as mentioned previously. The time domain resolution is determined when the center and lower or upper bounding optical wavelengths are chosen. The mapping is shown in Figure 21.

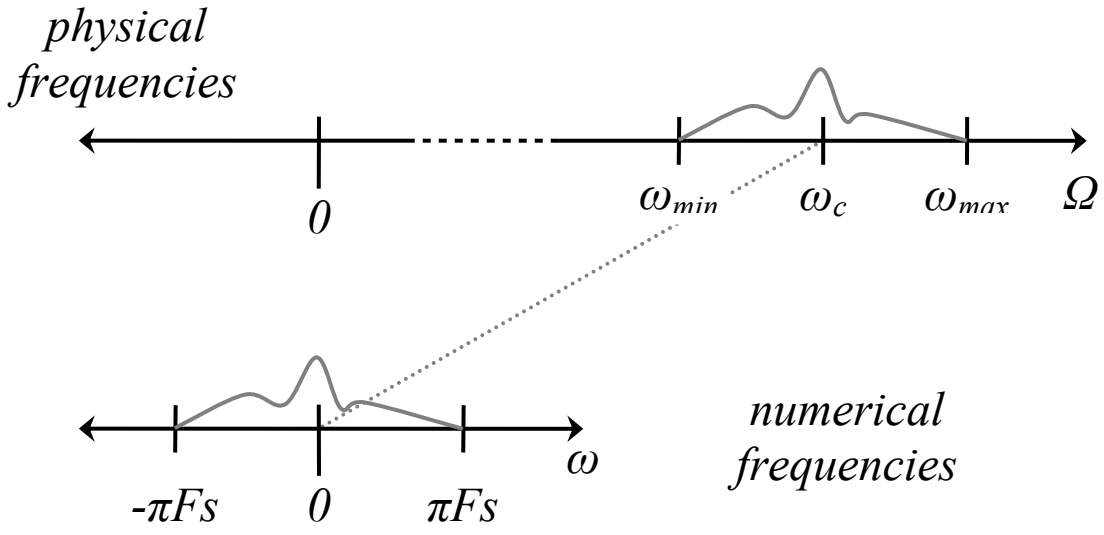

Figure 21. Mapping physical frequencies to numerical frequencies in the SSFM.

In Figure 21, the physical (optical) frequency axis is denoted by Ω (rad/s). The spectrum represented by the simulation is identified by a center frequency ω_c as well as the minimum and maximum of the represented spectrum, ω_{min} and ω_{max}. The numerical simulation data contains this spectrum as illustrated on an angular frequency axis denoted by ω (rad/s), where the frequency span is based on the Nyquist sampling criterion for a sampling rate Fs (s^{-1}).

Incorporating Raman Response in the Split Step Fourier Method

The equation for the nonlinear operator (78) includes an approximation of the Raman response using the characteristic Raman response time $T_R \approx 3$ femtoseconds. This avoids the much greater computational demand of convolution with a Raman response function. A simulation comparable to that shown in Figure 18, but using the convolution of the Raman response, is shown in the figure below. The moments equation trace is again superimposed.

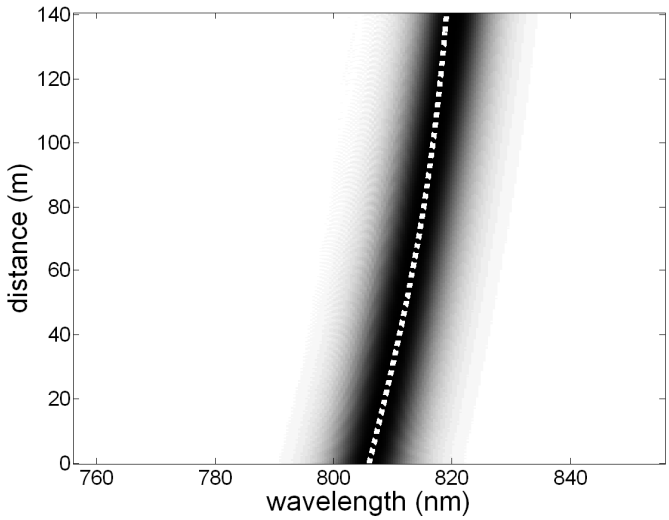

Figure 22. Convolution-based Raman shift simulation.

A pictorial representation of convolution with the Raman response is shown in Figure 23. It is provided in order to illustrate the scale of the Raman impulse response relative to the pulse and to emphasize that the signal function $u(t)$ is arbitrary.

The Raman response for silica has been obtained by spectral measurement of the Raman gain using a narrow linewidth laser. [58] A response function based on this data has been applied in the time as well as frequency domains by transformation according to the Kramers-Kronig relation. [38]

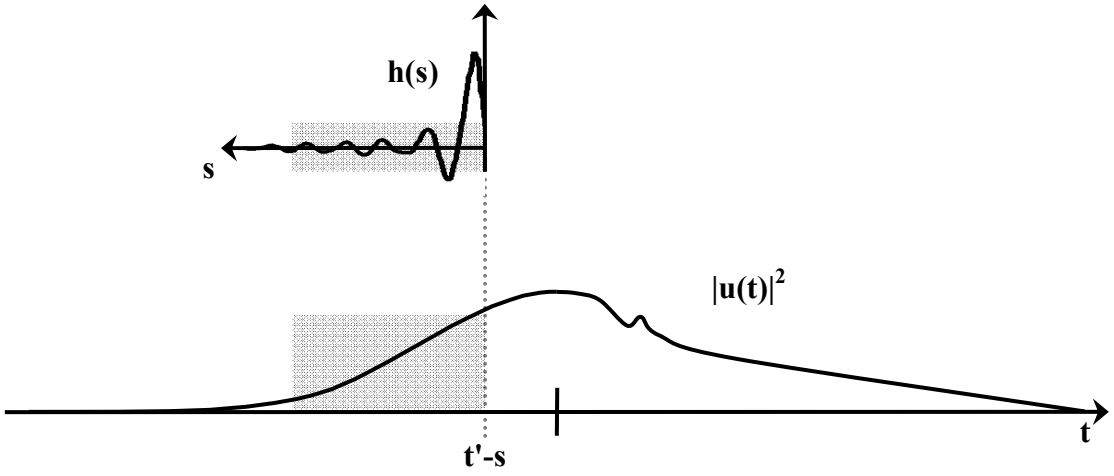

Figure 23. Raman response convolution.
***|u(t)|²* is the field intensity and *h(s)* is the temporal Raman response function.**

Raman response is incorporated in the GNLSE by the following replacement

$$|u(t)|^2 u(t) \quad \rightarrow \quad u(t) \int h(s)|u(t-s)|^2 ds \tag{80}$$

The left side of (80) is a computationally small term involving multiplication that grows in proportion to n. The convolution operation (prior to any optimization) grows as n^2. Because of the high computational demand, an approximation by a two-term Taylor series expansion is often used. [14, 59] The result is a differential term proportional to the Raman time constant T_R appearing in the GNLSE. The Taylor expansion of $u(t-s)$ is

$$
\begin{aligned}
&\left|u(t-s)\right|^2\Big|_{t-s\approx\tau} \approx \\
&\left|u(\tau)\right|^2 + \frac{d}{dt}\left|u(\tau)\right|^2(t-s-\tau) \\
&+\frac{1}{2!}\frac{d^2}{dt^2}\left|u(\tau)\right|^2(t-s-\tau)^2 \\
&+\frac{1}{3!}\frac{d^3}{dt^3}\left|u(\tau)\right|^2(t'-s-\tau)^3 + ...
\end{aligned}
\tag{81}
$$

Under a simplification $u(t) = u(\tau)$, which implies that u is constant over the duration of the Raman response function, terms can be moved outside the integral and the right side of (80) can be replaced with

$$
u(t)\left[\left|u(t)\right|^2 - \frac{d}{d\tau}\left|u(t)\right|^2 \cdot \int h(\tau)\tau \, d\tau\right] \tag{82}
$$

This argument is only valid when the initial pulse duration is over 60 fs and the constant amplitude approximation within a 60 fs window holds during the course of propagation. It is important to note that these conditions can be violated when high input powers are used. In a recent study [47], it is concluded that the approximate Raman method produces satisfactory results for pulse widths greater than 60 fs. However, we found that the convolution based Raman response was necessary even with 120 fs input pulses for modeling the behavior of the higher-order solitons as well as the wavelength-shifted fundamental soliton.

Variable Step Size Technique

The limiting factor on the SSFM step size is the magnitude of phase shift generated by the nonlinear response. During initial stages, the high peak power level of the input pulse maximizes nonlinear phase shift and a small step size is necessary. Pulse squeezing and self steepening can raise the peak power even further, while attenuation and dispersion can reduce it. The Raman

contribution is a gradient-proportional term that can produce very large phase shifts. Signal artifacts such as aliasing can also introduce abnormally large nonlinear phase shift.

The GNLSE derivation is based on expansion in the vicinity of an input pulse at the initial wavelength. The self steepening term (SST) of the $\hat{N}$ operator is

$$\hat{N}_{SS} = \frac{2j}{\omega_0 A}\frac{\partial}{\partial t}|A|^2 A \tag{83}$$

The SST related phase shift can be found under presence of a Gaussian soliton-like pulse with shifted center frequency Ω_R:

$$A(t) = \sqrt{P_0}\, e^{(-t^2/2\tau_0^2)} e^{(j\Omega_R t)} \tag{84}$$

with the result

$$\hat{N}_{SS} = \left(\frac{-2P_0\Omega_R}{\omega_0} - j\frac{6P_0 t}{\omega_0 \tau_0^2} \right) e^{(-t^2/\tau_0^2)} \tag{85}$$

Inserting only this term into the SSFM algorithm (76) and omitting $\hat{D}$ gives

$$A(t, z+\Delta z) \approx e\left(-\Delta z\gamma \left(\frac{6P_0 t}{\omega_0 \tau_0^2} - j\frac{2P_0\Omega_R}{\omega_0} \right) e^{(-t^2/\tau_0^2)} \right) A(t, z) \tag{86}$$

For a soliton with input power $P_0 \approx 16W$ corresponding to the $N = 1$ soliton with input 120 fs pulses at 806 nm in an idealized material with dispersion of 15 fs/nm·km, the Raman shifted soliton wavelength is roughly 820 nm after traversing one soliton period length (1.406 m), and the peak phase shift is roughly 0.022 rad/step, which is well below the $\pi/10$ phase shift criterion. For the same parameters and $P_0 \approx 1000W$, the Raman shift extends to 1100 nm, in which case the maximum phase shift exceeds 1 rad/step. This shows how the formulation of the

GNLSE and time domain SSFM approach tend to produce errors as the input power is raised and the Raman induced shift increases.

It is important to assure that the step size used in the SSFM is sufficiently small. The local error of an SSFM iteration is difficult to find, but the phase shift can easily be tracked. Step-back adjustment based on the nonlinear phase shift allows variable step sizes to be applied over the propagation length. The approach taken here was to choose a reasonable step size and to inspect the phase shift at regular intervals. When the maximum phase shift threshold was exceeded, the step size was divided into the fewest integer number of sections $\Delta z / M$ such that the criterion was met. Then, the previous step was repeated using the new size. This allowed straightforward bookkeeping and significant improvement in simulation efficiency. An example of the adapted step size in the simulation, shown in Figure 24, illustrates that the required step size evolved over the length of the fiber as the soliton wavelength underwent change.

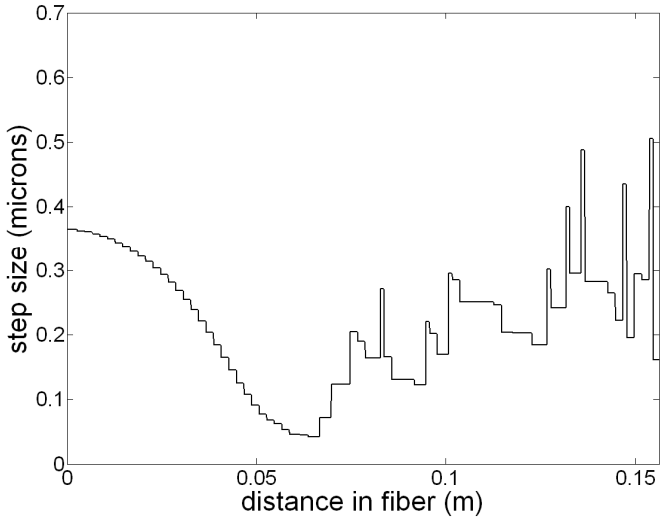

Figure 24. Adaptive step sizes in the SSFM.

Initially in the simulation shown, the step size can be chosen to be relatively large because of the relaxed conditions for the input pulse. The input pulse remained well-formed until after 0.05 m in the case shown above. In this case, the gradual decrease of the step size became asymptotic

after 0.05 m and a minimum was reached. There was no hard limit to the minimum step size in the simulation. The abrupt change of step size does not necessarily indicate any error. Based on the phase shift calculations, it is possible that excessive local error was introduced midway in the simulation. However, it is also possible that the spectrum simply evolved rapidly because of the generation of new spectral components. The variable step size technique does not rely on error estimation, so instability and error accumulation is possible even under the variable step size routine. Therefore, the sensitivity of simulations to scaling the step size was always manually inspected.

Circular Time Span in the Split Step Fourier Algorithm

The FFT involved in applying the dispersion operator $\hat{D}$ produces a circularly continuous time-amplitude trace $A(t)$. The simulation start and end points may or may not correspond to physical boundaries. Situations when boundaries are not desired but are necessary for computation often require modifications such as minimally reflecting absorption regions, especially in the FDTD which produces reflected fields. For the SSFM a cyclic time frame is acceptable because the signal waveforms involved in soliton propagation are usually discrete and few in number. This approach does introduce two important considerations. Firstly, the fundamental soliton is generally the slowest propagating component, and it can quickly reach the time window edge in simulations (it takes a longer time to travel through a certain distance in the fiber in comparison to the higher order solitons, as shown in Figure 25). The crossing events should be tracked to avoid misinterpreting the pulse walk-off behavior.

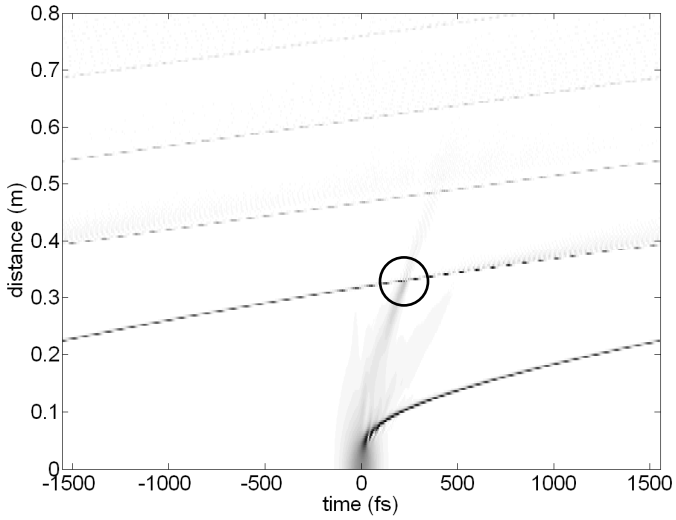

Figure 25. Soliton collisions due to cyclic boundaries.

Secondly, artificial soliton collisions may occur when a circular boundary is used. An example is shown in Figure 25. Interestingly, in the canonical solution of solitons, a collision only causes a phase shift, and a superimposed pair of solitons momentarily take a single soliton shape. Nevertheless, in the non-canonical GNLSE it is important to avoid superimposing signals. In the simulations, collisions are easy to spot and they can be prevented by temporarily splitting the SSFM simulation spectrally (although this was not implemented). The simulation illustrating a soliton collision is shown in Figure 26. In Figure 26 (a,b), soliton collision is present and can be identified in the time trace Figure 26 (a). In Figure 26 (b), the spectrum with soliton collision is shown. The comparable collision-free simulation is displayed in Figure 26 (c,d).

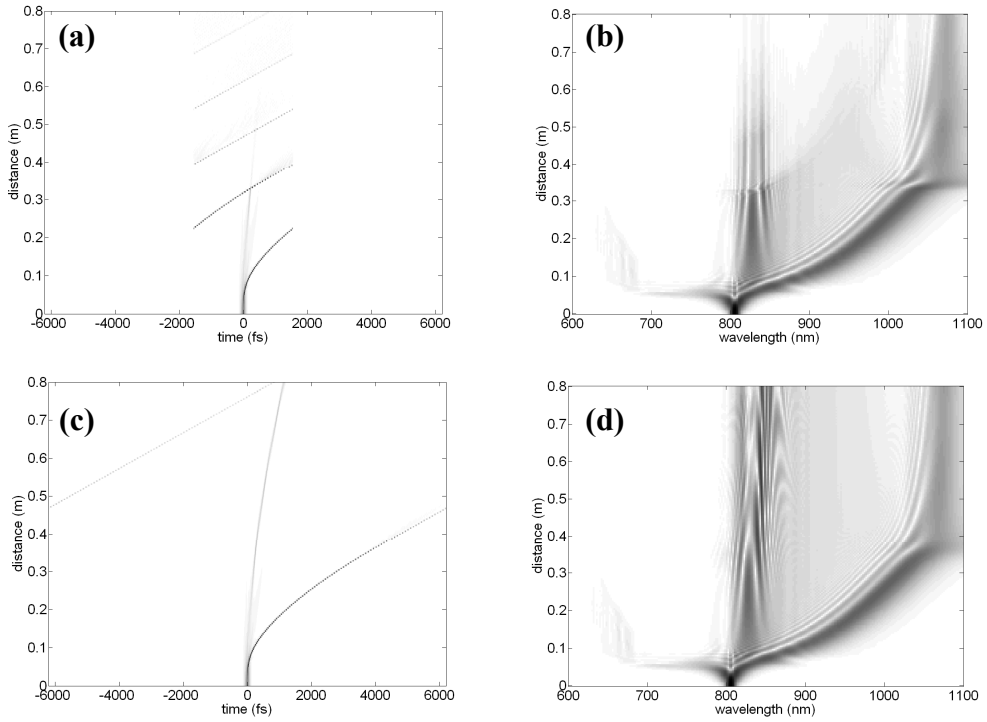

Figure 26. Collision problems in the SSFM.

It might appear for this case that the impact of pulse collision is slight, because the longer wavelength shift remains nearly unchanged. However, in addition to a small glitch at that wavelength, the secondary soliton at roughly 820 nm appears to collapse. In any case, non-physical collisions are not acceptable in realistic simulations.

Calculation of Raman Response via Circular Convolution

Considering that dispersion is already implemented by FFT, which produces a time axis with cyclic boundaries, it makes sense to replace the convolution step for the Raman response by a circular convolution using another FFT. Ordinary numeric convolution has a computation cost $\propto n^2$, while a substitution with FFTs as

$$\sum_{i=0}^{n-1} A(x)h(x-i) \Rightarrow \Re e\left(ifft\left\{fft(h)\times fft(A)\right\}\right) \tag{87}$$

incurs the computational cost of two FFTs, $\propto 2n\ln n$. The Raman impulse response $fft(h)$ can be calculated once and cached. For $n = 2^{13}$ the difference is a 450× reduction in the number of arithmetic operations. The real operation $\Re e()$ is used only to avoid numeric artifacts because no imaginary part is expected. Furthermore, because the impulse response of the Raman function is itself quite long, circular convolution may also prevent some truncation.

Fundamental Soliton Orders

To verify the correct behavior of the SSFM numeric simulations, solitons of various orders were propagated under the same conditions. They are shown in Figure 27 below. The pictures are greatly condensed in order to save space. Each soliton number is represented with a picture pair: to the left is the time amplitude, with abscissa spanning -300 fs to 300 fs and to the right is the spectral intensity where the abscissa spans wavelengths from 756 nm to 856 nm. Dispersion was spectrally uniform with D = 15 fs/nm·m at the center wavelength of 806 nm, the FWHM pulse width was 120 fs and power was varied from soliton order 0 (arbitrarily small power) to soliton orders 1 through 9 according to the soliton equation. The soliton period z_0 was 1.406 meters. The vertical axis for both Figure 27 and Figure 28 is distance $0 < z < z_0$. The intensity mapping of each figure was normalized to provide the best possible visual contrast. It should be clarified that, because these simulations are for demonstrating the canonical soliton solutions, the Raman and optical shock terms of the GNLSE were not included.

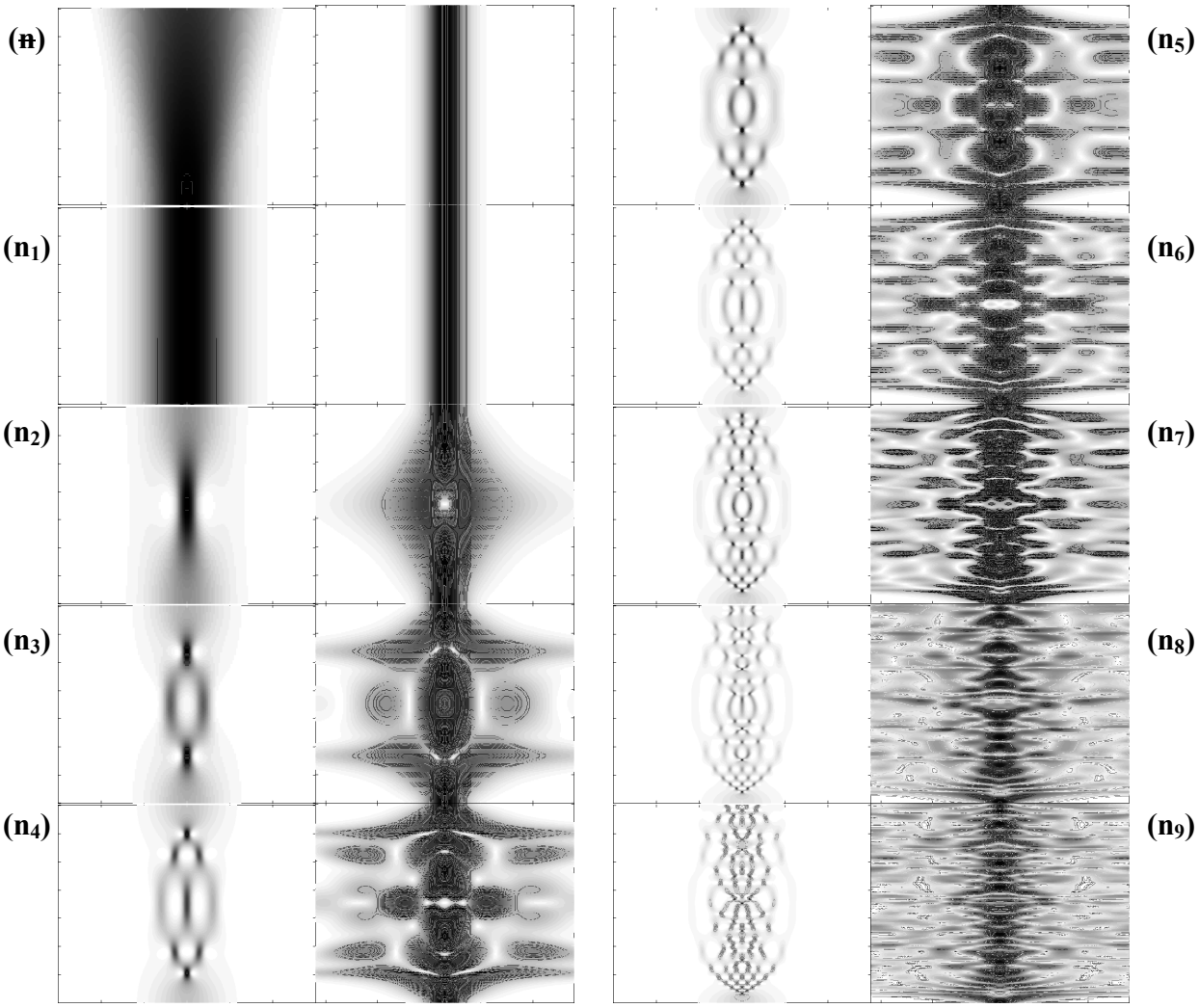

Figure 27. 2nπ soliton time and frequency features (n=0,1,…9).
D(806nm) = 15 fs/nm*m, Tfwhm=120fs; zo=1.406 m
left axis: time -300:300 fs & right axis: wavelengths 756:856 nm
Left column: time -300:300 fs for the horizontal axis and distance (0 to z0) for the vertical axis. Right column: wavelengths 756:856 nm for the horizontal axis and distance (0 to z0) for the vertical axis.

Soliton order 9 was the highest power level before the accumulated error interfered enough to alter the periodicity of the soliton. This served as a benchmark for the numerical accuracy of the simulations.

Separating Effects of the GNLSE Terms

The GNLSE contains various terms tied to individual physical phenomena. Pulses at the power level corresponding to the 8th order soliton were propagated with inclusion and exclusion of GNLSE terms. The results are shown by the pictures in Figure 28 below, arranged similarly to the previous figure. In the first set (1a,b), all nonlinear responses are removed to isolate dispersion of 15 fs/nm·m. In the second set (2a,b), dispersion is removed and nonlinear induced phase shift is enabled resulting in self phase modulation (SPM). In the third set (2a,b), the dispersion is increased again to 15 fs/nm·m, providing stability conditions necessary for the 8th order soliton. In the fourth set (4a,b), only the self-steepening term is applied. In the next set (5a,b), only Raman response is applied. Note that the Raman contribution is more complex here than in the moments equation simulations because the power is now much higher. In the final set (6a,b), all terms are applied together. For comparison the wavelength limits were kept consistent.

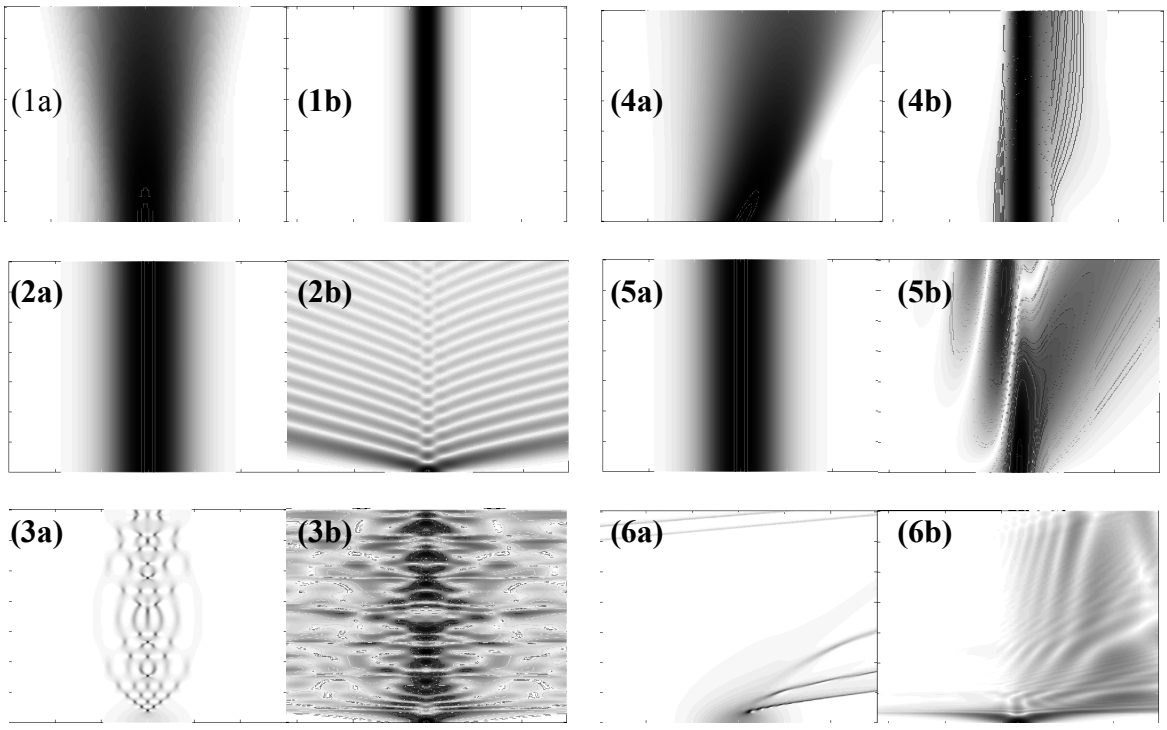

Figure 28. Dispersion (1), SPM (2), soliton (3), self steepening (4), Raman (5), all (6). (806nm 120fs input pulses z_0=1.406m, with *Po(N=8)*, *D=15* fs/nm·m)

Although wavelength shift is attributed to Raman induced frequency shift (RIFS), these figures indicate that SPM is a significant contributor. To investigate this further, the next simulations (shown in Figure 29) compared SPM with the other combined effects and the total result. As suggested by the SSFM results, the wavelength shift induced by Raman response was less significant than the SPM induced broadening over the short spans of fiber involved (< 3m), although the total wavelength shift involved a combination of the effects.

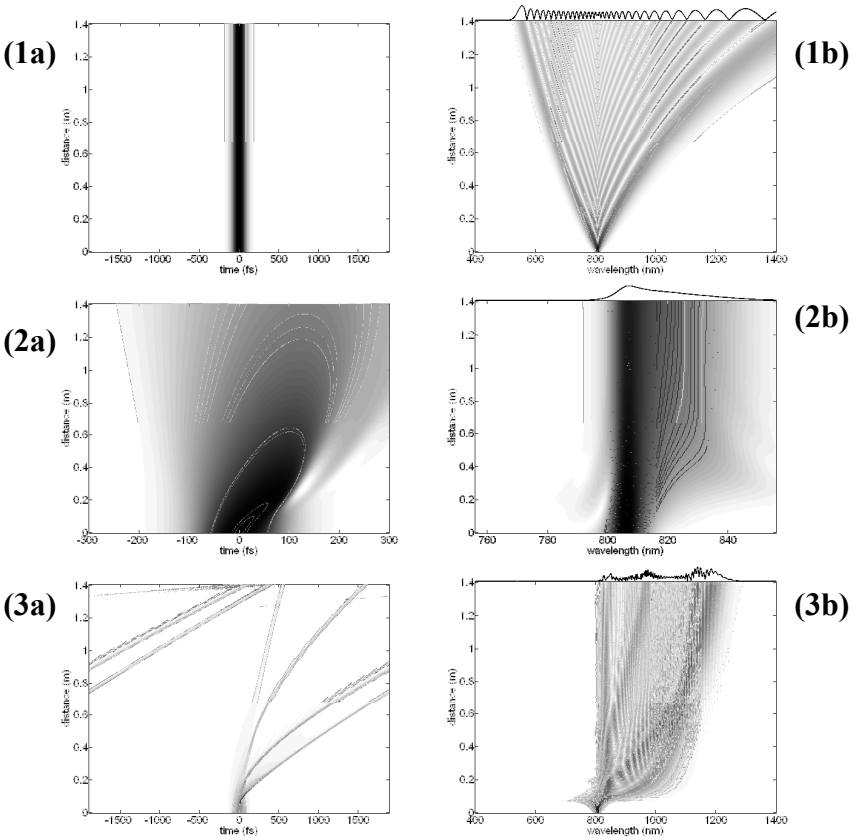

Figure 29. Isolation of SPM from other contributors to SSFS.
(1) SPM term only, (2) all terms except SPM, (3) all terms of SSFS
(capping plots for right column are the final spectra on a log scale)

As discussed in a later section, results obtained via an alternate, pseudo-spectral method of the split-step Fourier algorithm sometimes produced wider spectral shift at the same power level, suggesting that the Raman response might be greater. Although there may be some uncertainty,

the GNLSE simulations were based on the physical theory of the Raman scattering mechanism, and the soliton moments equations demonstrated agreement between the theory and numeric evaluation. Therefore, the results that have been shown here should be correct within the limits of the framework of the GNLSE and the SSFM method. The discrepancies with other simulations will be discussed in a later section detailing the pseudo-spectral split-step Fourier method and results.

Soliton Self-Frequency Shift

We now turn to measurements and comparisons of various fibers. The primary fiber used was NL-PM-750 (Crysal Fibre), and the length of fiber used in experiments was 2.5 m. The recorded output spectra of this fiber are shown in Figure 30. The input was a 806 nm 120 fs laser source (Femtolite F-100). A series of output spectra were acquired by gradually increasing the incident power level, but it was not possible to know the actual couple power in the fiber. Therefore, the waterfall axis in Figure 30 is formatted as a linear scaling of the fundamental soliton wavelength.

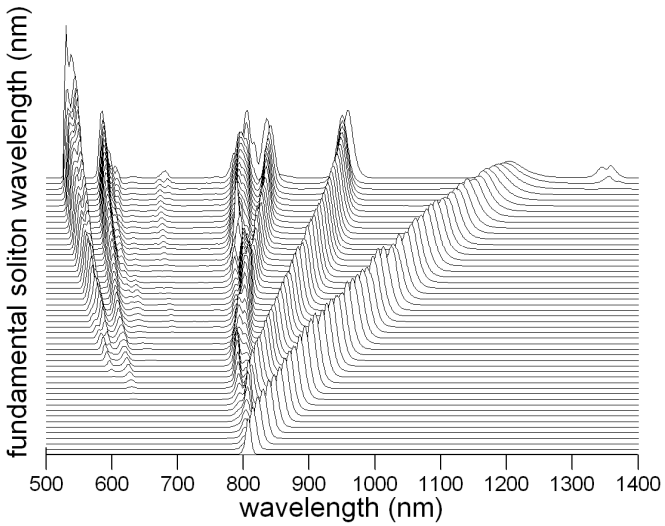

Figure 30. Measured output spectrum of NL-PM-750 (waterfall). The spectra were acquired by varying the incident power, but because the level of coupled power could not be determined, the waterfall axis was converted to a linear scaling of the wavelengths of the fundamental soliton.

As an alternative visual representation, the same data is shown as a spectrogram plot in Figure 31 (a). The results of simulations are also shown in this figure, and independent simulations of this fiber have also been previously reported [46]. A key feature observed, which is easiest to note in Figure 31 (a), is the rapid spectral broadening of the fundamental soliton as it reaches 1200 nm. This widening trend of the spectrum suggests that pulse widths at increasing wavelengths become extremely narrow, and indeed this characteristic was separately confirmed by the

measurements of pulsewidth shown previously in Figure 17. At wavelength shifts exceeding 1200 nm, which are not shown by Figure 17, Figure 30 and Figure 31 (a), the soliton spectral broadening of the fundamental soliton becomes so severe that no further usable soliton wavelengths can be reached. Instead, the spectrum develops longer-wavelength components that have characteristics both of solitons (shifting of wavelength with power) and of supercontinuum (extremely wide and not Gaussian or sech spectral lineshape).

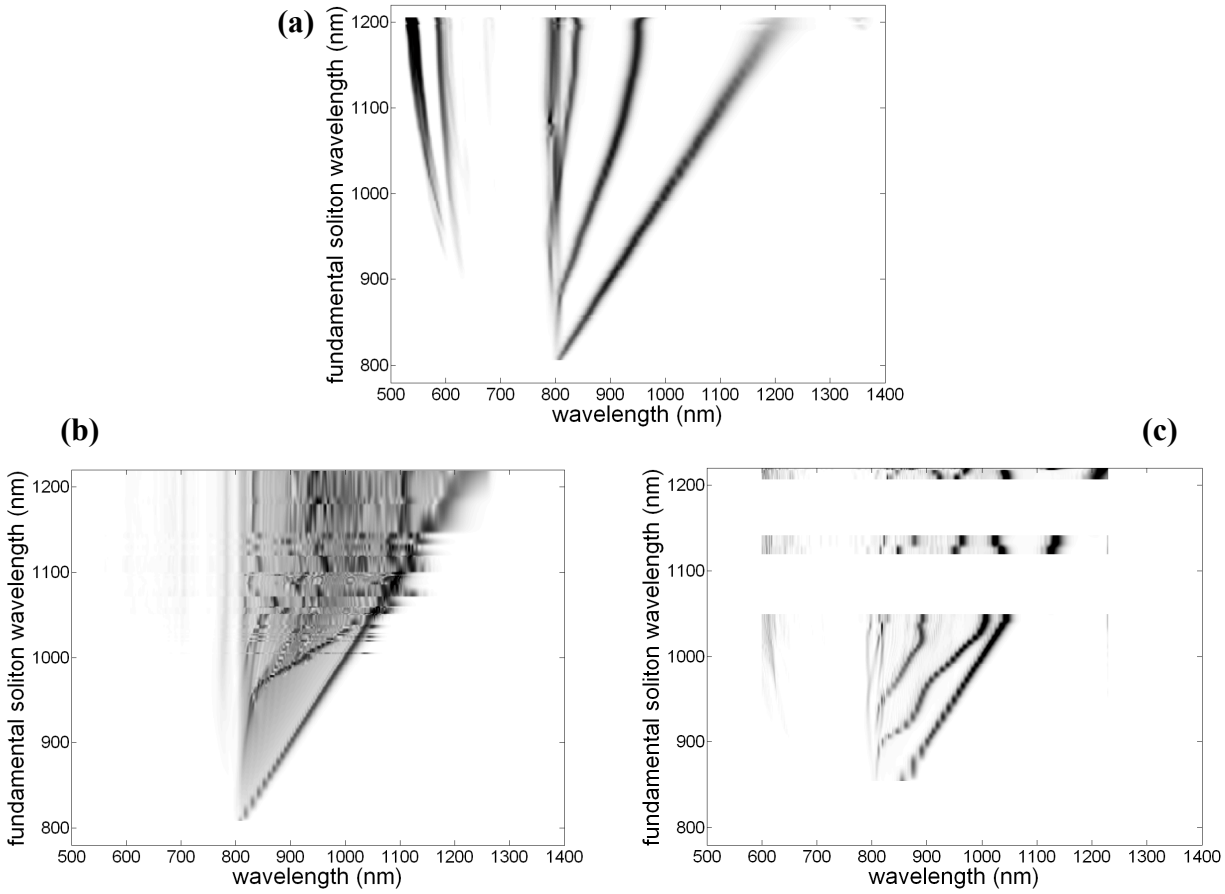

Figure 31. Varied output spectrum of NL-PM-750 (spectrograms)
(a) experimentally measured
(b) simulation using SSFM method (Matlab)
(c) simulation using VPI
(Blank regions appear at wavelengths where the parameterized simulations did not yield a fundamental soliton near that wavelength.)

The primary concern for wavelength tuning is the behavior of the longest-wavelength soliton, which is referred to as the fundamental soliton. A clearly isolated spectral component with the second-longest wavelength can be referred to for simplicity as the secondary soliton. This spectral component appears when the input coupled power exceeds the $N = 1$ condition. The behavior of the secondary soliton compared to the fundamental soliton is important, because its wavelength shift may impinge on the tunable spectral range of the fundamental soliton. For the case of the NL-PM-750 fiber with an 806 nm, 120 fs pulse input (shown in Figure 31 (a)), the secondary soliton rate of frequency shift seems to decrease as the fundamental soliton wavelength increases. This is beneficial, and it can most likely be attributed to a relative acceleration of the wavelength shift of the fundamental because of the decreasing dispersion between 1100 nm and 1200 nm.

The results of the SSFM based solution of the GNLSE are shown in Figure 31 (b), with 120 fs 806 nm input pulse propagation simulated as a function of the coupled input power. To facilitate comparisons of the experimentally measured characteristics of the NL-PM-750 fiber with the results of numeric simulations, the simulations were formatted with a vertical axis measured by linear scaling of the fundamental soliton. Because the fundamental soliton wavelength was not known *a priori*, and the input power was swept linearly, there are some regions which lack any simulation results. On the other hand, it was not feasible to scale the experimental data according to input power because the coupled power could not be known precisely. As Figure 31 (b) shows, the range of fundamental soliton wavelengths predicted by SSFM matches closely with those of the measurements in Figure 31 (a). In SSFM simulations, as the wavelength of the fundamental soliton reached the longest-wavelength limit, the appearance of longer-wavelength radiation matched that of the measured results at an input pulse peak power level approaching

1500 W. This corresponds with diminishing dispersion for wavelengths nearing 1200 nm, which leads to temporal squeezing of the pulse. In order to achieve the accuracy of the secondary soliton achieved by the SSFM, the simulations employed the convolution method of calculating Raman response. When the linear Raman approximation was used, the second-order soliton showed significantly less wavelength shift. Comparing the SSFM results shown in Figure 31 (b) to the measurements (a), the secondary soliton has a similar trend, but a spectral fission occurs roughly halfway in the figure, and as power is increased the longer-wavelength spectral line approaches the fundamental soliton wavelength. Meanwhile, the lower-wavelength component roughly aligns with wavelengths of the secondary soliton in the measured data. These discrepancies of the SSFM results compared to the actual fiber measurements leave some uncertainty in the accuracy of the SSFM simulations. As a potential source of independent verification, another simulation algorithm was also investigated. The alternative numerical simulation, which uses a spectral-split step method discussed in a following section and which was made with the software VPI, is shown in Figure 31 (c) alongside the other spectrograms. In Figure 31 (c), the higher order soliton behavior shows much greater variability than the SSFM result. In predicting the wavelength shift of the secondary soliton compared to the fundamental soliton, the VPI results overestimate the extent of secondary soliton shift both to measurements and the SSFM trials. Based on estimations of the coupled power in the experimental measurements, both simulations (traditional SSFM and the spectral method) accurately predict the relationship of the input coupled peak power and the fundamental soliton wavelength shift. The secondary soliton is approximately accurate in the SSFM simulations.

The anomalous dispersion range of the fiber plays a crucial role in the soliton tuning characteristics. Several dispersion profiles were investigated in order to understand the effect on

the maximum attainable wavelength shift as well as the optimal conditions for the widest spectral separation between fundamental and secondary solitons as well as higher order components. These dispersion profiles are shown in Figure 32.

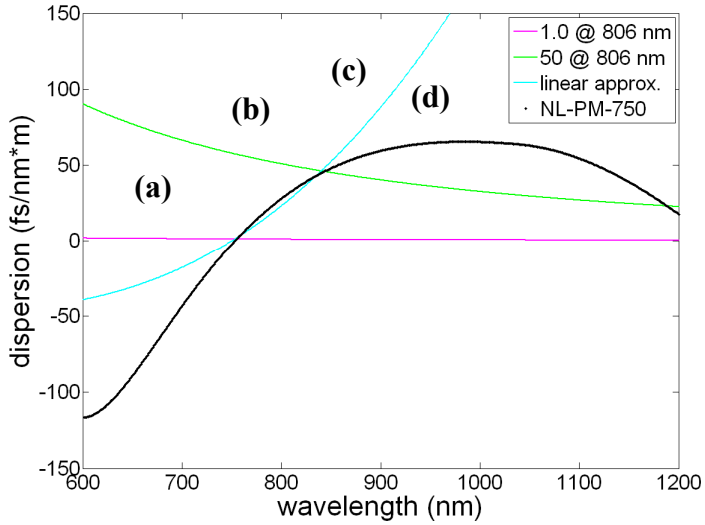

Figure 32. Comparison of four dispersion profiles.

Simulations were carried out using each of these profiles under the same global conditions. The results are shown in Figure 33. It should be noted that the fiber length was 2.5 m, but the simulations shown are carried out to 0.8 m because the spectral evolution has diminished by that point. In case (a), the anomalous dispersion is very small and not sufficient to overcome the SPM effects. The self steepening and SPM in this case were excessive, and because the simulation parameters were kept the same for all cases, the results became non-realistic after propagation of a short distance. In case (b), the dispersion is uniform and approximately matched to the dispersion value of the NL-PM-750 fiber at 806 nm. The dispersion experienced by the pulse remains constant over the course of the ensuing wavelength shift, resulting in the largest wavelength shift. In the next case (c), the entry point dispersion is again matched to the NL-PM-750 PCF, as is the zero dispersion wavelength, and thus the initial slope of the dispersion is made very high. With a very rapidly increasing dispersion, the net wavelength shift was much smaller.

This can be explained by the fact that excessive dispersion stretches the pulse and thereby reduces the peak power, leading to reduced RIFS. In the final figure (d), the manufacturer's measured profile for NL-PM-750 was used. This produced a wavelength shift that came closest to actual measurements. The standard value of Raman time constant (3 fs) and a reasonable input power (assuming 10% coupling efficiency) were used.

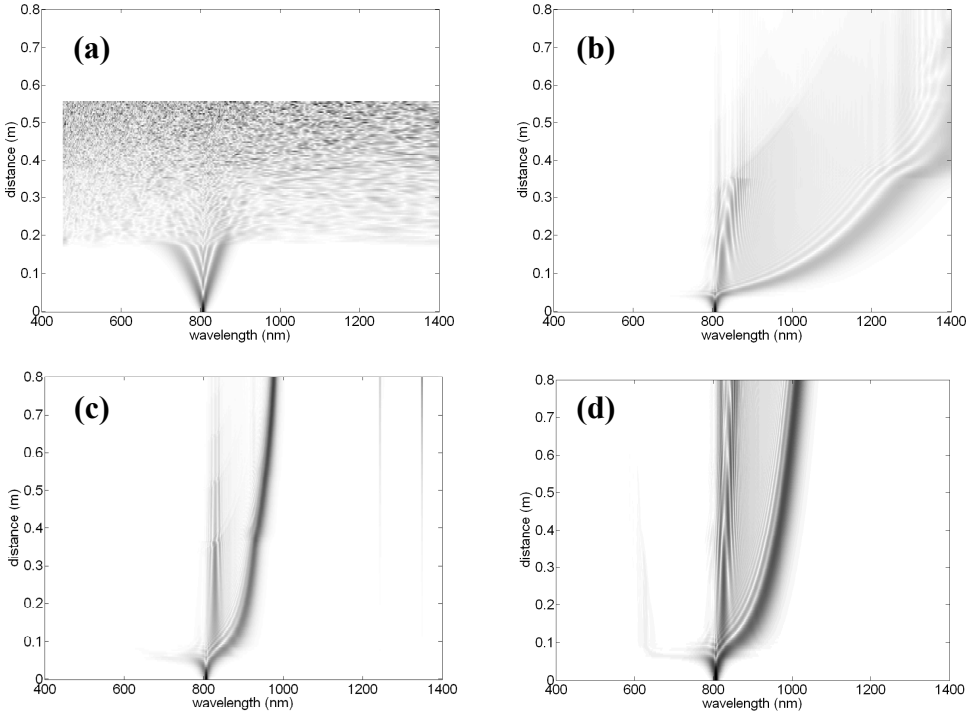

Figure 33. Simulations of four dispersion types.
Simulations results are shown for (a) uniform dispersion, 1 fs/nm·m at 806 nm (b) uniform dispersion, 50 fs/nm•m at 806 nm (c) linear increasing approximation with zero dispersion at 750 nm and matching dispersion slope of NL-PM-750 at laser wavelength 806 nm (d) NL-PM-750. The global parameters were 1 kW input peak power (representing coupling of ≈10% of maximum laser power), FWHM pulse width of 120 fs (sech pulses) and nonlinear parameter 95 W^{-1}km, and linear Raman approximation with T_R=3 fs.

Further investigations of soliton dynamics were made. The dependence of net wavelength shift on the dispersion level was tested with dispersion set globally uniform over the entire spectrum (similar to trace (b) in Figure 32). A scan of D=0 to D=100 fs/nm·m is shown in Figure 34. The pulse was propagated to 200 mm for each value of D (referenced at the input optical wavelength

806 nm). Again the input peak power was 1 kW, the FWHM pulse width was 120 fs (sech pulses) and the nonlinear parameter was 95 W^{-1}km. According to the soliton criteria, greater dispersion requires greater input power or shorter pulse width. Therefore it is reasonable that the wavelength shift reduces as dispersion increases. The spectrum of Figure 32(b) at the distance of 20 cm should be identical to the horizontal trace of Figure 34 at a dispersion value of roughly 50 fs/nm·m.

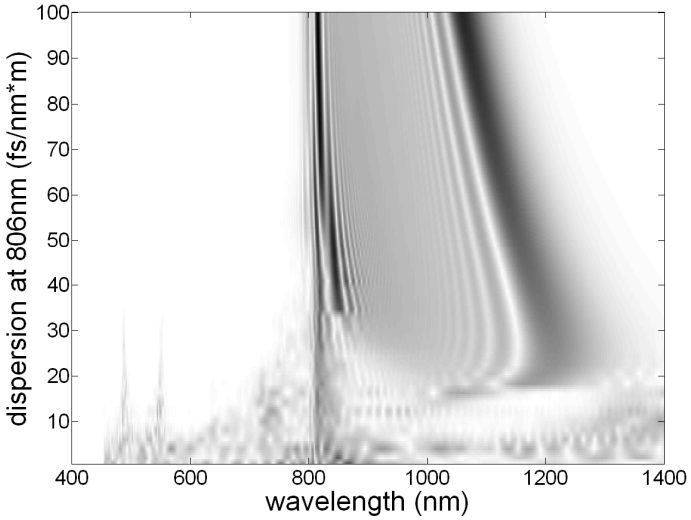

Figure 34. Dispersion level simulations.
Spectrum after 20 cm propagation (sufficient for inspecting soliton formation).

Considering that the range of 100 fs/nm·m represents roughly the largest variation found among common fibers, this simulation has shown that a tradeoff of roughly 60% of frequency shift can be expected. From a practical application point of view, simulation results shown in Figure 33 provide a guideline for fiber selection to optimize the fundamental soliton wavelength shift. The dispersion value at the input pulse wavelength should be higher than 30 fs/nm•m to avoid excessive pulse squeezing and SPM that can lead to the creation of a supercontinuum rather than a tunable soliton.

The next scan investigates the impact of the frequency slope of the dispersion. The soliton frequency shift is expected to be highly sensitive to the slope of the dispersion because of the changing soliton condition (64) caused by attenuation, dispersion and loss from the photon energy loss under soliton self frequency shift (SSFS). The dispersion slope corresponding to NL-PM-750 corresponds to a horizontal line roughly halfway in Figure 35. Soliton spectra are shown after 20 cm propagation with linearly increasing dispersion function with zero dispersion set at 750 and varying dispersion slope at 806 nm.

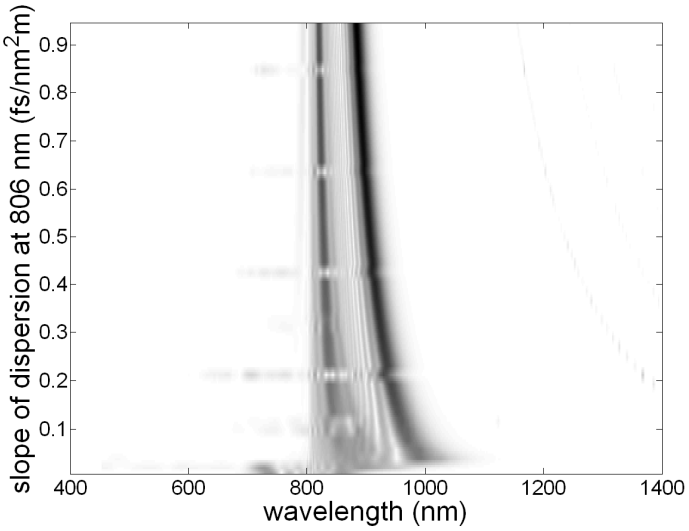

Figure 35. Dispersion slope simulations.
Spectrum after 20 cm propagation (sufficient for inspecting soliton formation).

The net effect on wavelength shift is similar to the case of varying the global uniform dispersion. This suggest that a large portion of the total wavelength shift occurs during the initial propagation in the fiber.

Nyquist Filtering

For large soliton wavelength shifts in the SSFM, new spectral components were observed originating at long wavelengths and merging towards shorter wavelengths. The appearance of a long-wavelength signal coincided with the disappearance of the fundamental soliton, and its frequency behavior seemed to be a reflection of the fundamental soliton frequency centering around a zero dispersion wavelength. Physically this might be attributable to Cherenkov radiation; similar results have been described by Skryabin, 2003 [44]. Although the NL-PM-750 fiber did appear to have new, longer wavelength components with very high input powers, it did not appear to be symmetrical to components below the zero dispersion wavelength. In the simulation domain the spectral margin is very large because of the time resolution needed for accurate calculation of the Raman and self-steepening terms. Occupation of most of this large spectrum is not physically allowed because of waveguide loss, but in simulations some spectral components may crop up if an attenuation window is not included as necessary to simulate the waveguide loss.

New spectral components may be generated in multiple ways by physical and numerical effects. In nonlinear fiber propagation, new frequencies are generated physically by self phase modulation (SPM) and the Raman induced frequency shift (RIFS). Non-degenerate four wave mixing should be negligible because of the lack of phase matching conditions when dispersion is sufficiently high. Second Harmonic Generation (SHG) should be absent because non-crystal materials lack the necessary inversion symmetry. SHG is not mathematically included in the SSFM terms. SPM does not affect the pulse temporal shape, so the spectrum may spread gradually but without any limitation. Therefore, some frequency aliasing in the numerical simulation may eventually arise due to continued intra-pulse mixing. A band-limiting attenuation

profile was implemented to simulate a realistic wavelength-dependent attenuation in the PCF that would eliminate uncontrolled spectral accumulation in the non-physical regions. The attenuation was simply increased at frequencies outside of $F_S / 4$, where F_S is the sampling rate.

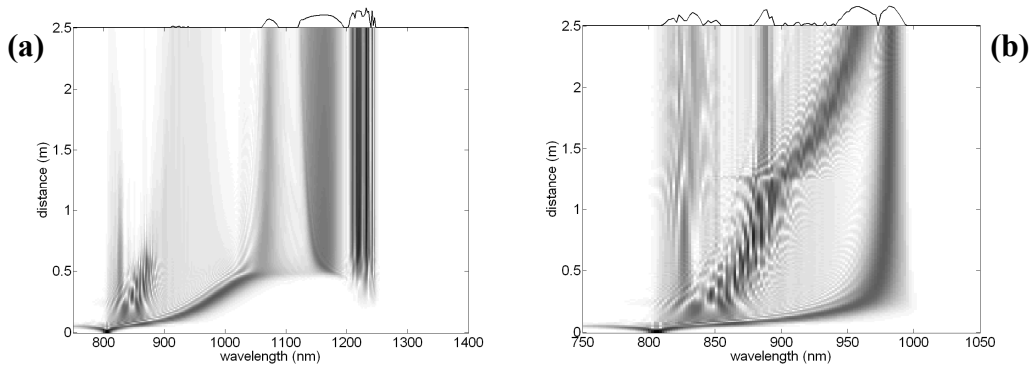

Figure 36. Soliton wavelength shift simulated with SSFM without (a) and with (b) Nyquist band limiting

In Figure 36, image (a) shows simulation with unrestricted bandwidth, while image (b) shows the same simulation with Nyquist band limiting. The zero dispersion wavelength was roughly 1100 nm. The total wavelength shift of the first order soliton is somewhat reduced when the filter is applied. However, the wavelength evolution then becomes monotonic and free of any long-wavelength spontaneous interference. In general, the best choice of cutoff wavelength to reduce numeric artifacts was one that shouldered the expected fundamental soliton wavelength with a small margin. Generally, restricting the spectrum by this means had the same effect shown in the above figure, which is a slight reduction of the soliton shift.

Effect of Pulse Width on Soliton Spectra

One important consideration for wavelength tuning applications is the spectral window over which the fundamental soliton can be tuned without the introduction of other interfering frequency components. While lasers with different pulse widths may produce the same net wavelength shift of the 1st order soliton, the 2nd order soliton behavior may vary greatly. Unfortunately, the shortest pulse width fiber lasers are the most difficult to produce. Fiber lasers

built with a certain power level specification may yield a range of possible pulse widths, with the shortest pulse widths being the rarest. The effect of pulse width on the soliton spectrum under the constraint of pulse energy is therefore an important concern. Primarily, the spectral tuning window is determined by the relationship of the 1st and 2nd order solitons. The shortest possible pulse width is desirable because it maximizes the nonlinear effect, but it may not be the best for reducing the shift of the secondary soliton. SSFM simulations are shown in Figure 37, in which the pulse width was increased under fixed pulse energies, with P_0 set at 1000 W for 120 fs pulses.

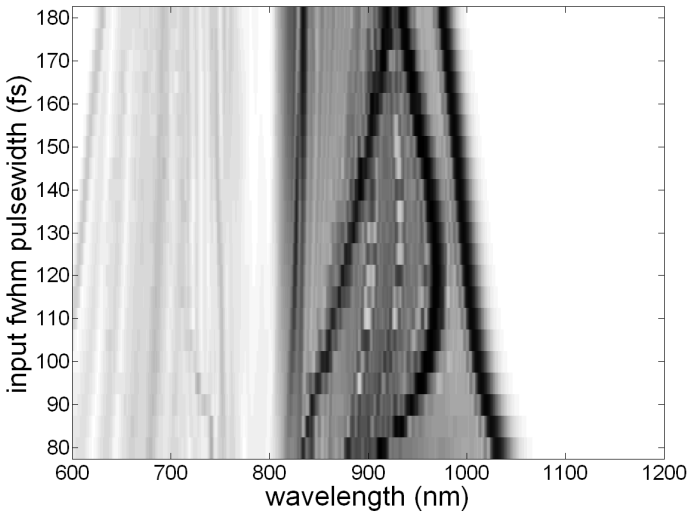

Figure 37. Varying pulse width with pulse energy constrained.

These results were produced using a full Raman convolution in the SSFM, which offers the greatest degree of accuracy for higher-order soliton features. For these simulations, the pulse energy was constrained, which is usually a design constraint of available fiber lasers. As the pulse width is increased, the power is decreased in proportion. However, in order to maintain the same soliton condition, the power must actually scale up by the square of the factor applied to the pulse width. Therefore, it is reasonable that the maximum wavelength shift would become significantly less in this simulation series as the pulse width was increased.

Comparison of Commercial Photonic Crystal Fibers for Wavelength Tuning

Three photonic crystal fibers (PCF) useful for wavelength shifting are NL-PM-1.8-750 (Crystal Fibre), NL-3.3-890 (Blaze Photonics) and SC-3.7-975 (NKT Photonics). Although all of the fibers were studied using the SSFM, only the NL-PM-750 fiber was available for measurements. The manufacturer's measured dispersion and attenuation profiles are displayed for comparison in Figure 38. Note that in the figure below, dispersion of NL-3.3-890 beyond 1238 nm is extrapolated.

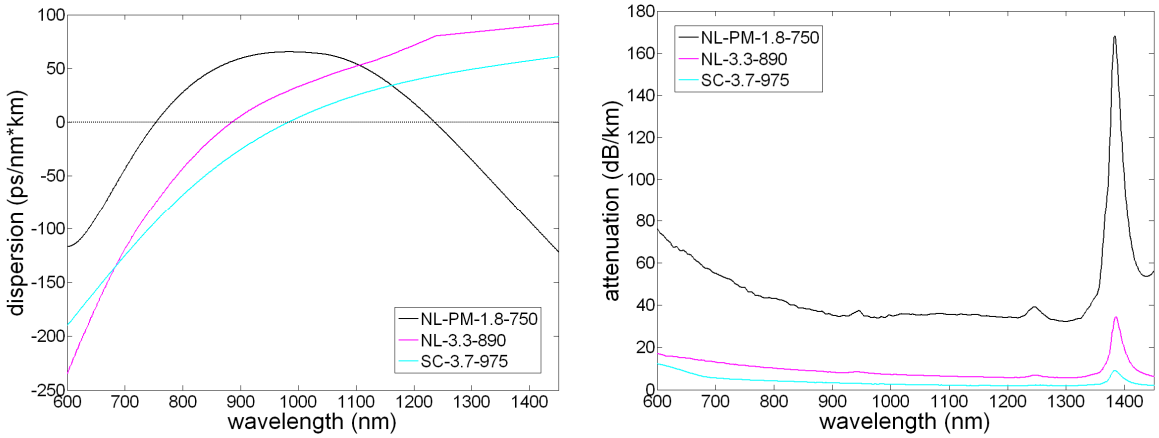

Figure 38. Dispersion and attenuation characteristics of three photonic crystal fibers.

The full SSFM simulation of the 2.5 meter NL-PM-750 fiber is shown in Figure 39. The input was 806 nm laser with 120 fs pulse width (fwhm) and 1000 W peak power coupled into the fiber.

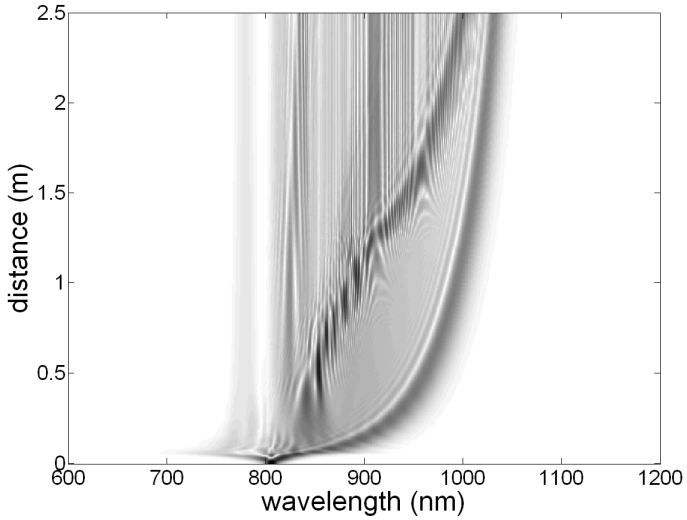

Figure 39. Simulation of NL-PM-750.

The amount of fundamental soliton wavelength shift predicted by this simulation is in approximate agreement with the recorded spectrum shown in Figure 30. Varying the input wavelength for this fiber has significant impact on the soliton wavelength shift, as shown in Figure 40. With the propagating distance constrained to 2.5 m, the higher order soliton may exit the fiber at different points within its own soliton period, which is changed by varying the input wavelength. In Figure 40, the vertical axis is the wavelength of the input pulse. The horizontal axis is the wavelength axis of the output spectrum. Varying the input wavelength effectively changes the soliton period because the dispersion level is different for the entering pulse. The result is that the display of the spectra versus input pulse wavelength resembles the periodic spectral evolution of the $N = 2$ soliton.

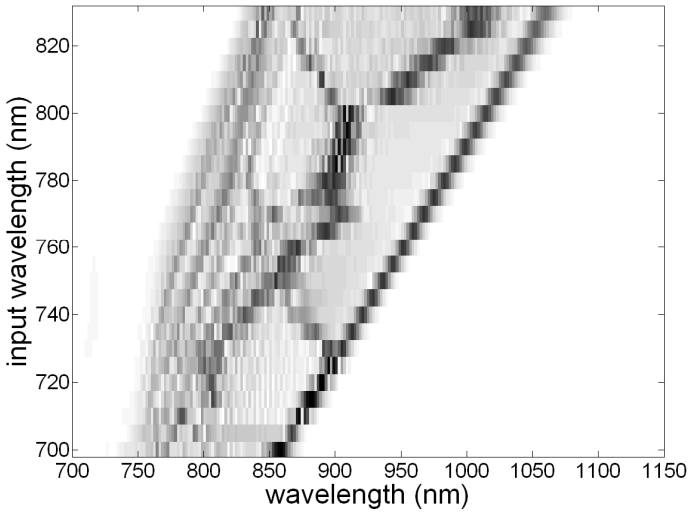

Figure 40. Varying the input wavelength in NL-PM-750 fiber.

Simulation of the SC-37-975 fiber is shown next, in Figure 41. For this fiber the input was 734 W peak power at 1030 nm with 90 fs fwhm pulse width.

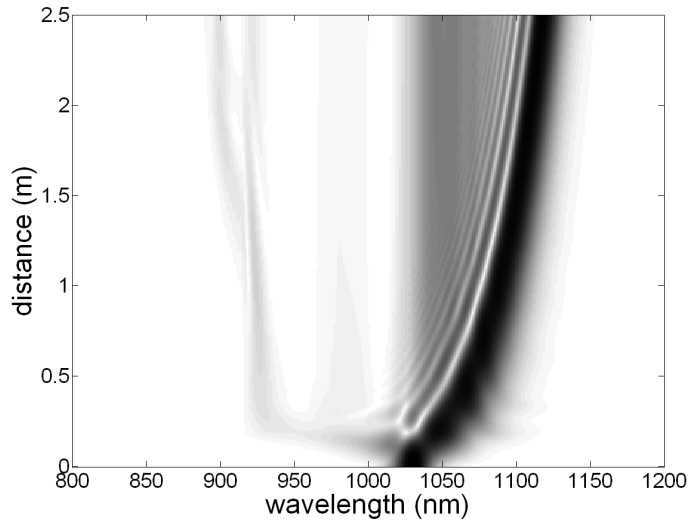

Figure 41. Results for SC-37-975.

An alternative to the traditional SSFM known as a pseudo-spectral SSFM method has been proposed. Details of this method used can be found in [35, 38, 60], with relevant details of the implementation given in [60]. Simulations were made using the pseudo-spectral split step algorithm which uses a somewhat modified approach to the numeric evaluation of the GNLSE.

This work was done using a third party software (VPI) [61]. Results involving this method are discussed in the following sections.

Pseudo-Spectral SSFM Method

A pseudo-spectral SSFM method (PSFM) is implemented in the software package VPI [61]. The algorithm described by Mori [60] is referenced in an example file provided with the software, and the example produces output identical to that reference. Otherwise, the software implementation is proprietary. To match the frequency notation used in this work, if the physical frequency Ω is related to the central frequency ω_0 as $\omega = \Omega - \omega_0$, then a normalized pulse amplitude can be defined as [60]

$$\widetilde{S}(\omega, z) = \sqrt{\frac{\varepsilon_0 nc}{2P_0}}\widetilde{A}(\Omega, z)e^{i\int_0^z dx(\beta(\omega_0)+\omega\beta_1(\omega_0))} \tag{88}$$

The PSFM algorithm, as formulated in [60], is then

$$\begin{aligned}\frac{\partial}{\partial z}\widetilde{S} = &-i\left(\beta(\omega_0+\omega)-\beta(\omega_0)-\omega\beta_1(\omega_0)-i\alpha(\omega_0)\right)\widetilde{S}\ldots \\ &-i\gamma P_0\left(1+\frac{\omega}{\omega_0}\right)ft\left[S|S|^2 + S\,ft^{-1}\left[R(\omega)\,ft\left[|S|^2\ \right]\right]\right]\end{aligned} \tag{89}$$

where variables are similar to the ordinary SSFM variable definitions, and ft, ft^{-1} are Fourier transforms defined as

$$ft[U(T)] = \frac{1}{\sqrt{2\pi}}\int_{-\infty}^{\infty} dT\left[e^{-i\omega T}U(T)\right] \tag{90}$$

$$ft^{-1}[U(\omega)] = \frac{1}{\sqrt{2\pi}}\int_{-\infty}^{\infty} d\omega\left[e^{i\omega T}U(\omega)\right] \tag{91}$$

and $R(\omega)$ is the Raman gain spectrum. In this formulation, dispersion as a function of the propagation length is accommodated by a transformation of the time coordinate as [60]

$$T = t - \int_0^z dx \beta_1(\omega_0, x) \tag{92}$$

where $\beta_1(\omega) = (\partial / \partial\omega)\beta(\omega)$. The purpose of the time coordinate transformation is to allow the central dispersion to vary with propagation distance. The description of methods by [60] states as a limitation of traditional approaches that the SSFM relies on chromatic dispersion definitions by differential operators rather than arbitrary profiles. On the other hand, as already detailed in a previous section, arbitrary dispersion curves can be applied in the ordinary SSFM using an integration procedure. Using that approach, dispersion does not affect the definition of the time variable in any way.

When the propagation constant for the ordinary SSFM is generated according to the integration step previously described, and when the Raman effect is applied using FFT-based convolution, then the pseudo spectral method and ordinary SSFM appear to be identical. On the other hand, differences in the output of the pseudo spectral simulations (VPI) and traditional split step scheme remained. A PSFM simulation of 119 fs pulses at 1030 nm propagated in 2 m of SC-3.7-975 fiber is shown in the figure below.

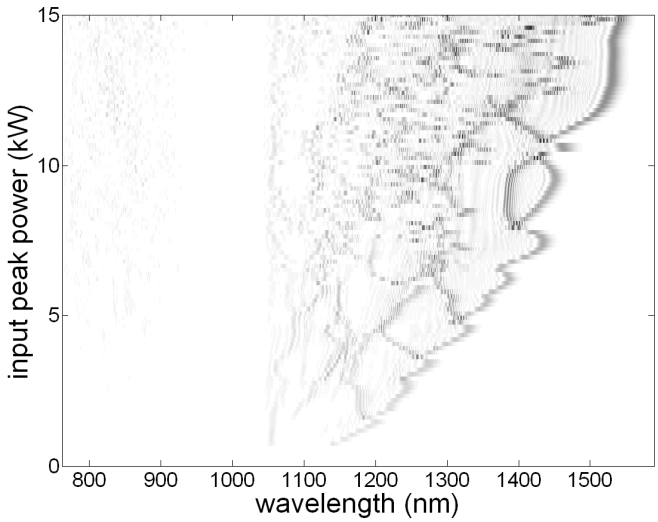

Figure 42. SC-3.7-975 spectra with 119 fs input.

The figure above shows a greater interdependence of the various soliton orders produced by an input pulse. The longest wavelength soliton splits chaotically upon a minor change of the input power, suggesting that it is similar to a coherent, higher order soliton. Such a result did not occur in the ordinary SSFM based on the GNLSE approximations. In the SSFM, pulse evolution is tied to the pulse initial origin, and the wavelength-shifted fundamental soliton does not split based on an increase of the input peak power. Realistically, soliton fission is expected from a physical standpoint. However, the chaotic spectral evolution provided by the VPI software is difficult to explain on the basis of the terms included in the GNLSE.

The theory and practical behavior of solitons is very complex. The results depend on detailed parameters of fiber dispersion and nonlinearity, signal pulse wavelength, shape and chirp, as well as theoretical models used in the simulation, numerical algorithm, approximations used and the associated accuracy. These investigations have attempted to characterize soliton behavior according to physical phenomena and to isolate various features of soliton propagation, leading to the ability to predict the output of untested combinations of photonic crystal fibers and pulsed fiber lasers. In some cases, the realistic output spectrum could only be obtained by measurement, but close approximations of the fundamental soliton wavelength shift and tuning window characteristics were made possible. As these results show, the pulse evolution has more chaotic features when simulated using a proprietary pseudo spectral method. In principle, the ordinary SSFM is limited to the effects included as terms in the GNLSE. However, neither the time-domain nor pseudo-spectral domain results are without error and simplification. Of greatest importance to this work is the behavior of the secondary soliton which interferes with the tunable spectral range of the fundamental soliton. As these simulations have shown, even the secondary soliton is difficult to model without understanding of the underlying optical effects. From a

practical perspective, both types of simulation were necessary together with measurements of available fibers and lasers in order to optimize choices between available lasers and photonic crystal fibers.

III. Rapid Quantitative Measurement of Two-Photon Förster Resonance Energy Transfer

Förster Resonance Energy Transfer (FRET) is a non-radiative energy transfer between two fluorophores [62-63]. Förster Resonance Energy Transfer provides a means to determine distances on a molecular scale, and thus FRET can be figuratively called a *molecular meter stick*. To determine distances between two points of a large molecular structure such as a protein, the relative efficiency of energy transfer between two fluorophores, the FRET Efficiency, must be extracted from fluorescence measurements. The technique of fluorescence labeling allows the controlled placement of fluorophores on specific locations of such large molecules. In recent years, the development of fluorescent dyes and proteins has spurred the study of protein structures and protein interactions in fixed and live cells [64-69]. FRET efficiency between a donor-acceptor pair is defined as the ratio of the rate of energy transfer between the donor and acceptor to the total decay rate of the donor. FRET efficiency provides a quantitative measure of fluorophore separation (r) because it has an r^{-6} dependence on the donor-acceptor distance, with r being in the range of 10 to 60 Angstroms in common applications.

The FRET efficiency can be measured by three different techniques: (1) the change in lifetime of the donor in the presence of acceptor, (2) donor dequenching, i.e. the enhancement of donor emission when the acceptor is deactivated (e.g. by photobleaching); or (3) the relative emission yields of donor and acceptor [65]. The third method is the most common and generally the most straightforward, with much faster acquisition than lifetime correlation. Donor energy transfers via FRET to the acceptor, causing FRET-sensitized acceptor fluorescence. Quantifying the sensitized fluorescence requires tracking of donor and acceptor fluorescence under donor and acceptor excitation [59, 70].

Care must be taken in particular to dissect spectrally overlapping contributions from donor and acceptor emission and to account for direct acceptor excitation [71-74]. Corrections for spectral overlap are particularly important for two-photon excitation (TPE), where excitation spectra are often broader than their one-photon counterparts and therefore more likely to overlap.

Although one-photon FRET excitation is straightforward, two-photon excitation (TPE) is advantageous for imaging applications due to intrinsic optical sectioning [75]. TPE has a number of additional advantages, such as the wide spectral separation of fluorescence from the excitation wavelength, reduced bulk photobleaching and better penetration depth at longer wavelengths. In single-molecule or single-pair FRET measurements, alternating laser excitation of donor and acceptor (ALEX) [76] (also termed pulsed interleaved excitation in applications with pulsed lasers [77]) has been used to control for the presence of an acceptor fluorophore. The issue of spectral overlap does not factor into fluorescence lifetime imaging microscopy (FLIM) techniques, e.g. FLIM-FRET [67].

High intensity pulses are required for two-photon excitation, and traditionally Ti:Sapphire lasers have been used for this purpose. Ti:Sapphire lasers are bulky and expensive compared to fiber lasers, and their wavelength adjustment is done via mechanical cavity tuning. The maximum tuning speed of Ti:Sapphire systems is currently in the range of 40 nm/s. By contrast, wavelength tuning based the SSFS transfers the speed limitation to the electro-optic modulator used to control the input power. Electro-optic modulation is non-mechanical and can be orders of magnitude faster. In order to increase speed and reduce the size and complexity of components in two-photon FRET measurements, a two-photon excitation (TPE) FRET system was developed based on a turn-key femtosecond fiber laser and a photonic crystal fiber, achieving wavelength shifting through Soliton Self Frequency Shift (SSFS) [78-79]. This system provides electrically

controlled wavelength tuning over a wide range, making it an ideal excitation source for two-photon FRET measurements and imaging. Wavelength switching was performed with latencies of 10-20 ms using a liquid crystal modulator, and 5 μs switching times were achieved using an electro-optic modulator based on ceramic material [78].

Our goals are to demonstrate the feasibility of wavelength switching TPE for FRET using a PCF and to validate our techniques by recording FRET values for two model FRET constructs. To verify our techniques, we made FRET measurements of calmodulin labeled with fluorescent dyes Alexa Fluor 488 and Texas Red, as well as a mutant fluorescent protein with linked E^0GFP and mCherry [64]. Calmodulin is a valuable candidate for FRET study because it plays fundamental roles in all living cells and because it undergoes conformational changes upon binding to calcium or specific target molecules [80]. E^0GFP and mCherry are useful as they, along with the other families of fluorescent proteins, can be expressed and observed in living cells. To demonstrate the feasibility of our two-photon FRET measurement system, we measured proteins with rapidly alternating excitation over a wide range of excitation wavelengths. Our results include a comparison of FRET values obtained for calmodulin over the donor excitation wavelength range as well as time based observation of FRET of an E^0GFP-mCherry protein.

FRET: Materials and Methods

Two-photon FRET measurement with fast wavelength tuning

The experimental setup is shown in Figure 43. The laser source (IMRA Femtolite-100) is a fiber-based femtosecond laser with a wavelength of 806 nm. Major components include a fiber laser, variable attenuator, a photonic crystal fiber (PCF), excitation filters, power meter (PM), optical spectrum analyzer (OSA), microscope dichroic (1), objective lens, emission filters, FRET dichroic (2) and avalanche photo diodes (APD 1, APD 2).

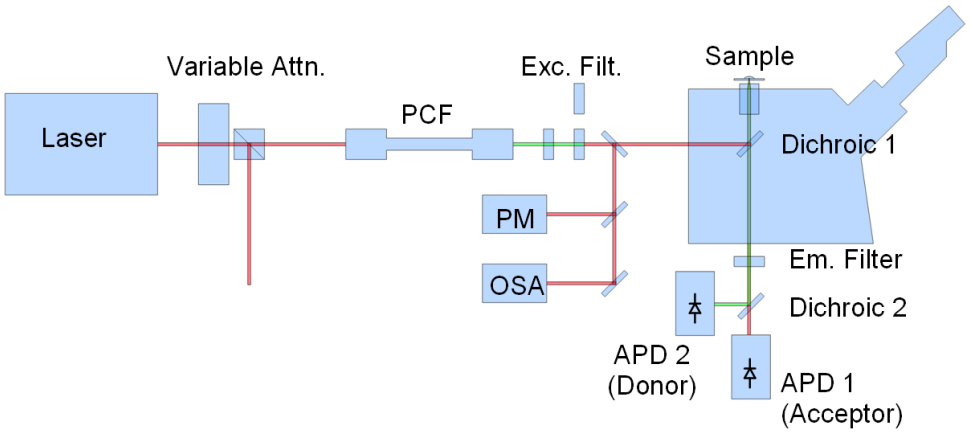

Figure 43. FRET system diagram.

The FWHM pulse width of the laser source is roughly 120 fs as measured using an autocorrelator (Femtochrome). The average output power is approximately 100 mW and the pulse repetition rate is 75 MHz, and therefore the pulse energy is 1.33 nJ with a peak power of approximately 11 kW. The transform-limited FWHM bandwidth, assuming sech^2 pulse shapes, is roughly 9 nm. The variable attenuator contains a voltage controlled liquid crystal (LC) birefringent cell (Meadowlark Optics) that rotates the polarization of the incoming vertically polarized light in reaction to a control voltage. The device is driven with a 2 kHz square voltage signal varied from 0 to 20 Vpp with zero DC offset. A polarization beam splitter transmits vertically polarized light towards the PCF while rejecting the horizontally polarized component. Pulses are then coupled into a Photonic Crystal Fiber (PCF) (Chroma NL-PM-750) to create wavelength shifted pulses through SSFS [45, 81-82]. Hardware control and data collection were made by a computer using a custom Matlab interface. A screenshot of the interface is shown in Figure 44.

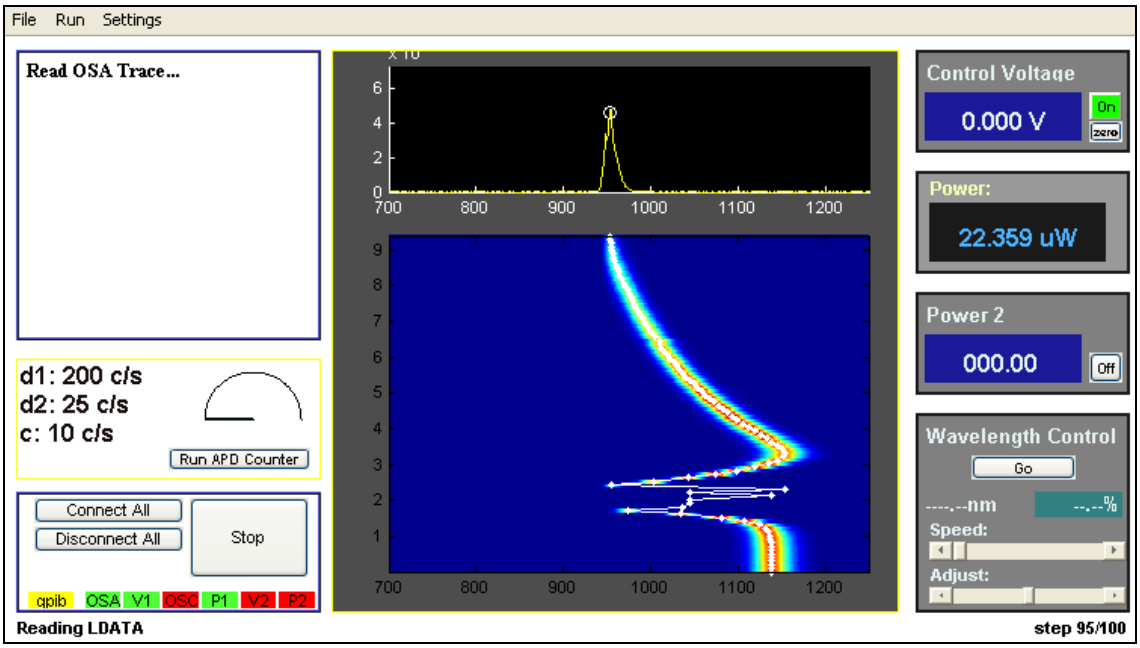

Figure 44. Matlab FRET system interface.

At the output of the PCF, a stable fundamental soliton is produced with a wavelength longer than that of the input pulse. The output wavelength depends on the length of the fiber (2 m) as well as the input power. With a sufficiently high input power, undesired high order solitons are also created, and these components must be removed by excitation filters. Figure 45 is a waterfall plot which shows the measured soliton output spectrum over a range of soliton wavelengths. It is a reduced set of the data shown in a previous figure for NL-PM-750 fiber, formatted to clearly show the tuning window and relative power levels. The fundamental soliton can be tuned from approximately 850 nm to as far as 1200 nm by varying the power of the input pulse at 806 nm. Below 850 nm, the power level of the wavelength-shifted soliton is relatively low, whereas beyond 1200 nm the output spectrum is significantly broadened and eventually develops into a supercontinuum.

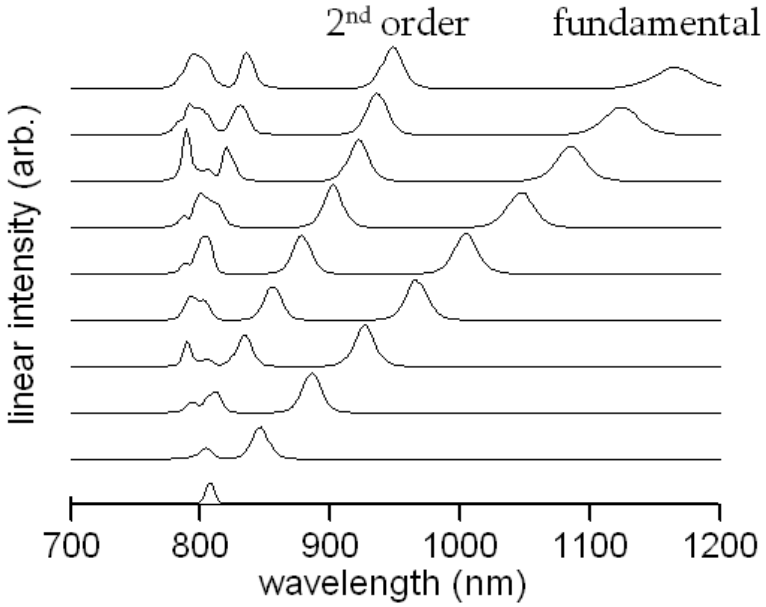

Figure 45. Evolution of the soliton spectra when the input power is varied.

The parameters that affect the tunable range include the dispersion characteristic and length of the fiber, as well as the width of the optical pulses. Hence, other wavelength ranges can be attained using different fiber types and input wavelengths. Note that as the wavelength of the fundamental soliton is tuned beyond 900 nm, a 2nd order soliton starts to appear which has to be filtered out by a long pass-filter in the experiment. In the measurements with wavelength scanning, we used a 950 nm long-pass filter when the fundamental soliton wavelength was between 975 nm and 1050 nm, and we used a 1000 nm long-pass filter for fundamental soliton wavelengths above 1050 nm. The optimal filter cutoff wavelength for a given application can be determined from the spectral characteristic shown in Figure 45. For rapid wavelength switching, changing filter is not feasible and a single long-pass filter must accommodate the entire switched wavelength region as discussed later.

Our system permits scanning a wide continuous wavelength range or rapid switching between two wavelengths. Targeting specific wavelengths involves calibrating the output pulse wavelength as a function of the input optical pulse power or control voltage on the electro-optic

modulator. A demonstration of wavelength switching between approximately 1000 nm and 1100 nm is shown in Figure 46. The time response is limited by the response of the LC cell. The activation and relaxation times of the cell differ due to intrinsic material properties; the response time for activation (starting at time 0 ms in Figure 46) is approximately 10 ms, and the relaxation time (starting at time 50 ms in Figure 46) is approximately 20 ms. We have previously demonstrated faster switching times of roughly 5 μs with a PMT-PT modulator [78]. While the PMT-PT material has much faster response, its electro-optic efficiency may vary over time at 800 nm, requiring more careful calibration. The LC cell provided very good repeatability with standard deviation of 0.40 nm based on 50 trials. The pulse to pulse stability of the PCF soliton output can also be affected by intensity noise and power fluctuations of the pump laser. Based on the power-wavelength characteristic, a 0.1% RMS relative intensity noise would produce on the order of 0.2 nm RMS wavelength error. Therefore, this should not present a concern for this application.

The optical pulses at the PCF output pass through a bank of long-pass filters, which isolate the fundamental soliton and reject higher order solitons. A small fraction of the excitation light is sent to an optical power meter and optical spectrum analyzer for monitoring. The microscope (Olympus IX-71) houses a dichroic beam splitter (Chroma 800dcspxr) and objective lens (Olympus UPlanSApo 60x/1.20 Water Immersion). Because neither the dichroic beam splitter nor the lens is fully optimized for infrared wavelengths, their attenuation is stronger at 1150 nm than at 850 nm by approximately 4dB. Fluorescence emission passes back through the microscope dichroic splitter, a set of emission band-pass filters, and finally through a FRET dichroic splitter which discriminates donor and acceptor emission. Light is detected by avalanche

photodiode photon counters (Micro Photon Devices PDM Series). We characterized crosstalk by measurements of reference dyes and by calculations based on profiles of the optical components.

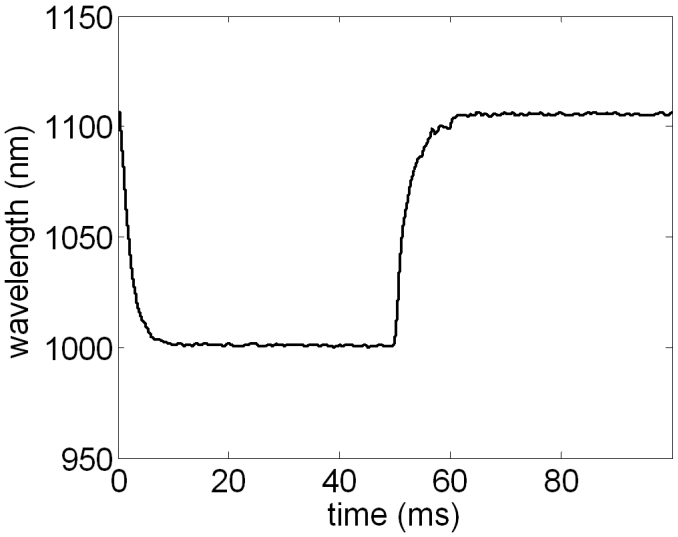

Figure 46. Wavelength switching time response.

The data shown in Figure 46 was sourced from traces measured by a high speed photodiode. In order to translate photo current values into wavelength values, an interpolation curve was used consisting of individually recorded data pairs (photo current and corresponding wavelength) measured at 100 points.

FRET Sample Preparation

The methods of preparation of calmodulin (CaM) labeled with Alexa Fluor 488 (AF-488) and Texas Red (TR) dyes were described in [80]. A specimen was prepared by diluting 50 µL of CaM in 50 µL high calcium buffer. A 25 µL volume of this solution was placed on a 25 mm glass cover slip treated with Bovine Serum Albumin (BSA). BSA was used to reduce adhesion of the protein to glass surfaces. The microscope focus was set 10 µm above the cover slip top surface. The concentration of CaM in the specimen was roughly 2.2 µM. Samples of the AF-488 and TR dye preparations were used for calibration.

The plasmid for E^0GFP-mCh was a kind gift from Dr. Lorenzo Albertazzi. Linked E^0GFP-mCherry (E^0GFP-mCh) FRET protein was developed by Albertazzi and coworkers [64]. The concentration of E^0GFP-mCh solution was approximately 2.0 μM. The fusion construct contains a thrombin enzyme cleavage site to allow separation of the two fluorophores. Cleaving eliminates FRET and thus provides calibration for the FRET efficiency measurement. The cleaving solution was prepared by combining 10 mL Phosphate Buffered Saline (PBS) solution, 1000 Units of bovine thrombin and 1% w/v BSA. The E^0GFP-mCh sample was cleaved with one part by volume cleaving solution added to ten parts by volume protein solution. Roughly 86 Units thrombin were used per milligram of protein, with a final thrombin concentration of about 9 Units/mL. Alongside the thrombin sample, a FRET sample (no thrombin) was incubated in buffer solution of PBS with 1% w/v BSA added. Specimens were placed on glass cover slips under the same procedure as described for CaM.

Calculation of experimental FRET efficiency from fluorescence intensities

FRET Efficiency calculation can be conveniently separated into two groups: (1) calibrations only related to the excitation and measurement optics system, and (2) calibrations only related to the fluorescent specimen. In our methodology, the following two parameters are related to specimen calibration: G, which accounts for fluorescence yield between the two fluorophores, and γ, which accounts for the overlapping excitation spectra of the two fluorophores. FRET efficiency can be expressed as

$$E = \frac{F_A}{F_A + G \cdot F_D} \tag{93}$$

where F_A is the sensitized acceptor fluorescence, F_D is the donor fluorescence and the factor G accounts for donor versus acceptor detector efficiency and quantum yields [65].

Overlapping Emission

The fluorescence F_A is measured primarily as counts in one photo detector, C_1, while F_D is measured primarily in C_2. We use a simple matrix notation to describe the relationship between detector counts and fluorescence. Using this notation we incorporate cross talk terms in a matrix S and background counts Bg_1 and Bg_2 as

$$\begin{bmatrix} C_1 \\ C_2 \end{bmatrix} = \begin{bmatrix} S_{1A} & S_{1D} \\ S_{2A} & S_{2D} \end{bmatrix} \cdot \begin{bmatrix} F_A \\ F_D \end{bmatrix} + \begin{bmatrix} Bg_1 \\ Bg_2 \end{bmatrix} \tag{94}$$

Elements of S are products of the various filter transmission curves, fluorophore emission spectra and detector responsivity, with one of four possible combinations, e.g.

$$S_{1D}(\lambda) = C_{norm} \cdot \Re_1(\lambda) H_1(\lambda) H_O(\lambda) I_D(\lambda) \tag{95}$$

where $\Re_1$ is the responsivity of the first (acceptor) photo detector, H_1 is the FRET dichroic filter transmission to the first photo detector, H_O is the transmission of the objective optics (common to all), $I_D(\lambda)$ is the donor emission spectrum normalized to unity area and C_{norm} is a normalizing constant. Transmission curves were generally held in data format, so S_{1D}, etc, were found by numeric integration over the relevant wavelength range. Inverting leads to the following equation to determine fluorescence values:

$$\begin{bmatrix} F_A \\ F_D \end{bmatrix} = K \cdot \begin{bmatrix} S_{2D} & -S_{1D} \\ -S_{2A} & S_{1A} \end{bmatrix} \cdot \begin{bmatrix} C_1 - Bg_1 \\ C_2 - Bg_2 \end{bmatrix} \tag{96}$$

The value of the constant K can be disregarded since it can be factored out in the efficiency equation. Since S is normalized, quantum yield differences and system bias between acceptor and donor responses can be lumped into the factor G, which can be measured experimentally.

We evaluated G according to the approach of [71], using measurements from a pair of samples, one with FRET and the other with no FRET, but otherwise identical in excitation and emission spectra and relative concentrations. From these samples we recorded ΔF_A and ΔF_D, the changes in fluorescence between the two samples taken under donor excitation, taking $G = \Delta F_A / \Delta F_D$.

Comparing crosstalk values calculated from emission spectra and filter transmission curves to those measured for the individual dyes, we found agreement within 3.0%. The measured crosstalk from AF-488 emission to the acceptor channel was 9.1%, and crosstalk from Texas Red emission to the donor channel was 2.9%. Since we could not measure separate E^0GFP and mCherry proteins, the calculated values (5.2 % donor emission to acceptor channel and 4.8 % acceptor emission to donor channel) were used.

Overlapping Excitation

In determining F_A and F_D, (96) corrects for cross-emission but does not account for cross-excitation. In particular, the Texas Red two-photon excitation band overlaps the TPE peak of Alexa Fluor 488 as shown in Figure 47. The fraction of acceptor fluorescence caused by this direct excitation could not be measured directly, but it could be extrapolated by taking acceptor fluorescence under acceptor excitation and scaling it by γ, the ratio between the TPE cross section of Texas Red at the donor and acceptor excitation wavelength. The FRET sensitized acceptor fluorescence was calculated as

$$F_A = F_{Ad} - \gamma F_{Aa} \tag{97}$$

where F_{Ad} and F_{Aa} are the measured acceptor fluorescence during excitation at donor and acceptor wavelengths, respectively.

It is useful to compare our methods with the three-cube method [71, 73], in which measurements of F_{Dd}, F_{Ad} and F_{Aa} are made with alternating filter sets and a single photo detector. As discussed in [73], in three-cube FRET correction for donor emission in the acceptor channel is made by calculations analogous to (96), while signal from acceptor emission in the donor channel is mitigated with narrow band emission filters. Note that we did not use individual narrow band emission filters, relying only on the dichroic beam splitter as a wavelength discriminator. Using two detectors, we measured donor and acceptor emission simultaneously, and the excitation wavelength was switched electronically so as to obtain all four signals, F_{Dd}, F_{Ad}, F_{Aa} and F_{Da}. We thus corrected all emission cross talk by the matrix calculation of (96). This approach can compensate a great degree of emission overlap in the detectors, allowing wider bandwidth emission windows and hence somewhat higher signal levels. Most importantly, it eliminates the need to alternate filter sets during measurement.

The peak two-photon excitation (TPE) wavelengths of the FRET fluorophores were found by scanning the excitation wavelength over a wide continuous range. To calculate TPE spectra, average dark counts were subtracted and intensities were normalized by the square of the measured excitation power. Excitation power and wavelength were monitored as described above.

FRET Results

Two-photon excitation spectra of Texas Red and Alexa Fluor 488

Two-photon excitation spectra are shown in Figure 47 for Texas Red and Alexa Fluor 488 dyes used in labeling calmodulin. For the purpose of comparison, the one-photon absorption (OPA) spectra measured with a UV-Visible Spectrophotometer (Agilent Cary-100) are also shown in

the same figure. In Figure 47, two-photon excitation is shown in dashed lines and one-photon absorption in solid lines. Texas Red is shown in bold and Alexa Fluor 488 in thin lines. The top axis shows TPE wavelength, and the OPA wavelength is on the bottom axis. In agreement with general TPE characteristics, prominent spectral components of the OPA align with components of the TPE spectra on a double wavelength scale. The relative intensity of bands are generally different in two-photon and one-photon excitation, specifically with spectral intensity in two-photon excitation shifted to vibronic bands, leading to a blue shift in the peak of the two-photon excitation spectrum compared to the one-photon absorption spectrum, as noted previously [83-85]. While few examples of AF-488 or Texas Red TPE spectra are available in the literature, we note that the TPE excitation spectrum of Alexa Fluor 488 presented here differs from that given in [86].

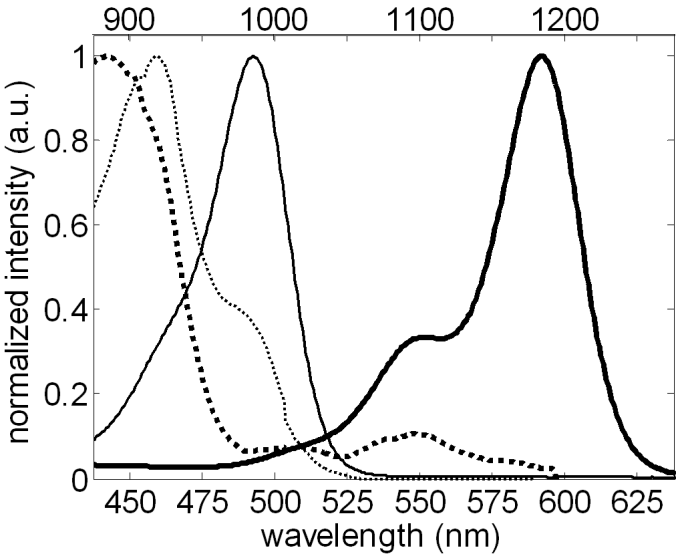

Figure 47. TPE and OPA of Texas Red and Alexa Fluor 488.
Texas Red is shown in bold lines. Alexa Fluor 488 is shown in thin lines. Dashed lines indicate two-photon excitation (axis above). Solid lines indicate one-photon absorption (axis below). The peaks of Texas Red are near 690 nm and 890 nm for OPA and TPE, respectively. The peaks of AF-488 are near 490 nm and 920 nm for OPA and TPE, respectively. TPE spectra were measured using the FRET measurement system. Traces are normalized.

FRET Efficiency of Calmodulin with Alexa Fluor 488 and Texas Red

In order to resolve any uncertainty in accounting for the strongly overlapped TPE of Texas Red and AF-488 near 900 nm, we varied the donor excitation wavelength over a broad range. The dependence of calculated FRET efficiency on the choice of donor excitation wavelengths is shown in Figure 48.

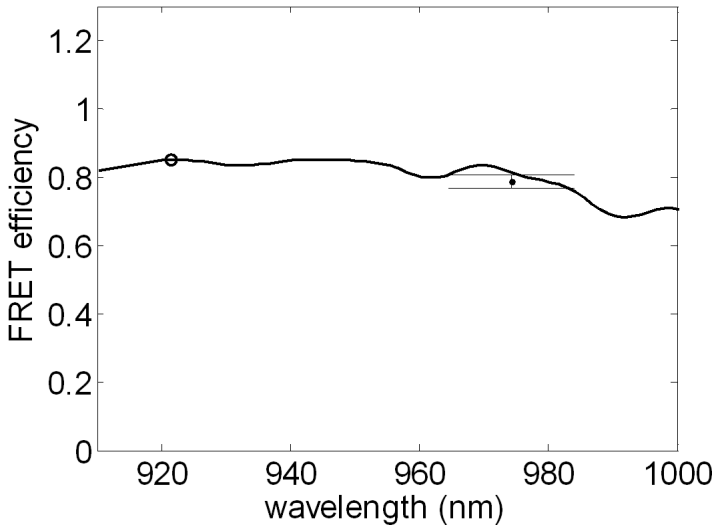

Figure 48. CaM FRET efficiency versus donor excitation wavelength.

In Figure 48, a circle marks the optimal wavelength choice of 922 nm, corresponding to the peak two-photon excitation of AF-488. The point marker with error bars shows the results of switched wavelength measurement, which was made at 974 nm to avoid producing higher order solitons within the pass band of a single excitation filter set in place.

The continuous line in Figure 48 was obtained by slowly scanning the wavelength of donor excitation; it provided the baselines to validate the results of wavelength switched FRET. As expected, the measured FRET efficiency shows little variation over the region of strong two-photon excitation of AF-488 and only shows a marked deviation in the region of weak two-photon cross section at wavelengths greater than 980 nm.

Our value of 0.85 for CaM two-photon FRET efficiency measured at 920 nm excitation wavelength is in close agreement with the previously reported value of 0.87 based on single photon excitation [87]. Moreover, the broad wavelength scan verified the accuracy of FRET measurements away from the peak donor TPE, at longer wavelengths. Therefore we could perform fast wavelength switched FRET in a wavelength region that avoided the need to change the long-pass filter during the measurement.

FRET efficiency of linked E^0GFP & mCherry

The FRET efficiency of E^0GFP-mCh measured using two-photon excitation was 0.27, in good agreement with our one-photon result (0.29) for the same sample. For calibration purposes, a sample of E^0GFP-mCh was cleaved with thrombin enzyme. The emission spectra of E^0GFP-mCh before and after thrombin cleavage are shown in Figure 49, showing the effect of FRET on the emission spectrum.

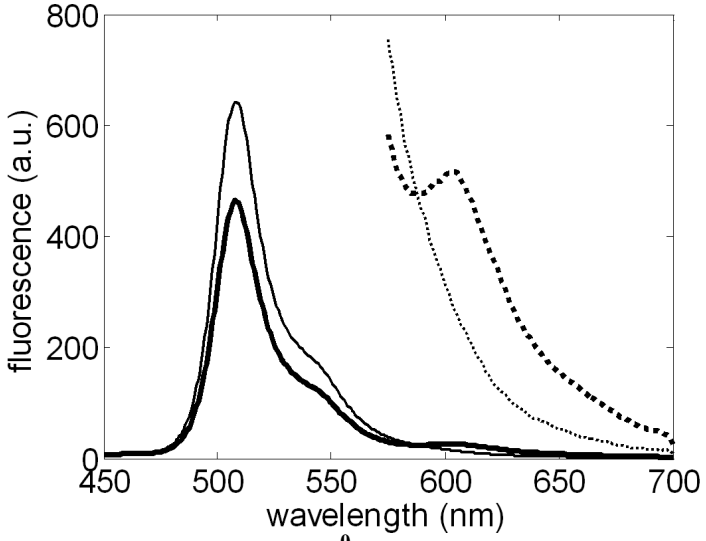

Figure 49. Fluorescence spectra of E^0GFP-mCh with and without cleaving.

In Figure 49, bold lines indicate E^0GFP-mCh fluorescence with FRET. Narrow lines show fluorescence of the cleaved sample (no FRET). Dashed lines are the same respective traces but magnified 20x. It appears that cleavage was complete because no observable acceptor emission remained, as shown by the 20x magnified traces in Figure 49. The difference between our result and the FRET efficiency of 0.35 previously reported in [64] could be explained by either a difference between the fluorophore separation of our E^0GFP sample and that of [64], or by a presence of unbound fluorophores due to some unknown cause. Because of the calibration process, a presence of unlinked E^0GFP in the sample would affect the measurement, but any presence of unlinked acceptor (mCherry) would not.

The results of various FRET efficiency measurements of CaM and E^0GFP-mCh are summarized in Table 2 and Table 3. Values of the Förster radius were 52 Å for CaM and 51 Å for E^0GFP-mCh [64].

Table 2. Summary of CaM FRET.

calmodulin	*FRET Efficiency*	*r*	*Excitation Wavelengths*
			(don. / acc.)
two-photon, λ-scanned	0.85	39 Å	922 nm / 1103 nm
two-photon, λ-switched	0.78 ± 0.02	41 Å	974 nm / 1097 nm

Table 3. Summary of E^0GFP-mCh FRET.

E^0GFP-mCherry	*FRET Efficiency*	*r*	*Excitation Wavelengths*
			(don. / acc.)
one-photon	0.29	59 Å	400 nm / 586 nm
two-photon, λ-scanned	0.27 %	60 Å	963 nm / 1077 nm
two-photon, λ-switched	0.28 ± 0.022	61 Å	964 nm / 1102 nm

The significance of the tabulated results can be summarized as follows. Firstly, measurement of CaM was made by dual ways: (1) relatively slow measurements made at various donor excitation wavelengths, even those wavelengths at which the excitation overlap between donor and acceptor were severe, and (2) rapid measurement with a relatively narrow gap between excitation wavelengths of donor and acceptor (974 nm and 1097 nm, as shown in Table 2). The first case demonstrated invariability of the measurement over a large range of excitation wavelengths as shown in Figure 48, which also required the necessary switching of one excitation filter. This test confirmed the successful calibration of the excitation and measurement optics. The second case resulted with a value of 41 Å, which is in agreement with the reference value of 39 Å taken from the first method, even though in the second method many measurements were taken rapidly. This

demonstrated the success of continuous calibration by alternating the excitation wavelength for each measurement.

In the case of E^0GFP-mCh, it was possible to evaluate the FRET efficiency of the same sample preparation by two independent means. Utilizing the specially designed cleavability of the E^0GFP-mCherry linkage, a one-photon value of 59 Å was found using a UV-VIS photo spectrometer. The values found using the two-photon FRET system, by manners similar to CaM, were 60 Å and 61 Å for E^0GFP-mCh, as shown in Table 3. This demonstrated agreement of the independent FRET efficiency findings. There was a discrepancy with an earlier reported result of a similar plasmid [64], which in the light of these results was most likely due to a difference between the two plasmid preparations.

Wavelength Switching Two-Photon FRET Measurement of CaM and E^0GFP-mCh

To investigate the capability of fast wavelength switching in this system, we made wavelength switched FRET measurements of both CaM and E^0GFP-mCh. Control voltages were calibrated to obtain the desired donor and acceptor wavelengths. Repeated tests of the voltage-wavelength characteristic confirmed that the calibration remained stable for at least one hour. Tracking the power levels confirmed that excitation wavelengths stayed entirely within ± 3 nm with respected to the targeted values over the course of each experiment. Photon counts were taken with 0.1 second integration. In Figure 48, the point marked with error bars shows the FRET measured with switched excitation between 974 nm and 1097 nm. These wavelengths were chosen to accommodate a fixed 950 nm long-pass optical filter in the system to reject the high order solitons.

The limitation of donor excitation range was not a concern for E^0GFP-mCh, because its donor excitation peak is at a longer wavelength than that of CaM, and therefore we switched the

excitation wavelength between 964nm and 1102nm in the measurement. The wavelength-switched two-photon FRET efficiencies of 0.78 ± 0.02 for CaM and 0.28 ± 0.022 for E^0GFP-mCh are consistent with the results of wavelength scanned measurements shown in Table 2 and Table 3.

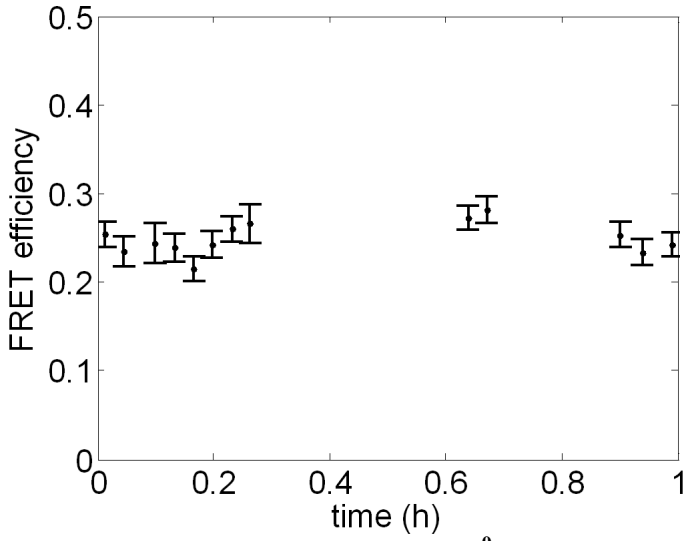

Figure 50. FRET efficiency of E^0GFP-mCh.

Figure 50 shows results for 13 data sets, where each point includes 50 measurements. Collection time was roughly 1 hour. Figure 50 shows the FRET efficiency of E^0GFP-mCh measured over the course of an hour. The average FRET efficiency of E^0GFP-mCh did not vary significantly. Since donor fluorescence can change due to varying concentration, pH or other factors, the value of F_D in (93) was tracked throughout measurements by gauging changes in the acceptor fluorescence compared to the reference acceptor fluorescence from the cleaved sample. The remaining fluctuations shown in Figure 50 are primarily due to noise in the collected fluorescence signals.

Summary of FRET System and Experimental Findings

We can conclude that the system measures FRET efficiency consistently and with a degree of accuracy comparable to traditional methods. The maximum measurement speed was primarily

limited by low fluorescence levels, a factor tied to the relatively low excitation power produced by the wavelength-shifted soliton pulse output of the PCF. With 0.1 seconds integration time per excitation wavelength, along with the added latencies of wavelength switching and the computer acquisition procedure, the overall measurement rate was roughly 1 Hz. The wavelength was switched within 10-20 ms as shown in Figure 46, and as previously discussed the technique allows much faster modulation depending on the choice of electro-optic modulator. The remaining latency of about 0.4 s, attributed to the computer acquisition procedure, could be greatly reduced by streamlining the hardware control, as the amount of data transferred is very small. Therefore, in principle the system has a capacity to reach 5 Hz as limited by 100 ms signal integration times for each measurement. This system could be used for imaging by raster scanning of the sample, with point by point FRET analysis. The imaging time, proportional to the measurement rate, would be generally acceptable for stable samples. The advantages of using this class of laser still outweigh the practical obstacles of higher power lasers for many uses, and the TPE rates could be significantly increased thanks to recent developments in specialty fibers which allow much greater efficiency SSFS with increased output power levels [88].

This work demonstrated a FRET measurement technique using two-photon excitation with rapid wavelength switching. It allowed measurement of two-photon excitation spectra of Alexa Fluor 488 and Texas Red dyes using continuous wavelength scanning between 850 nm and 1175 nm. One-photon absorbance measurements were also made separately for comparison. We compared FRET efficiency values of two proteins (calmodulin and an E^0GFP-mCh construct) under different excitation wavelengths, with wavelength switching as well as broad donor wavelength scanning in the same system. Electronically controlled wavelength switching simplified the two-photon FRET measurement process and eliminated the need to alternate filters for calibration.

The advantages of the system demonstrated here include lower cost of the laser source, greater portability because of the turn-key functionality of compact fiber lasers, and more rapid tunability of the excitation wavelength compared to conventional sources used for two-photon excitation.

IV. Fiber Laser Based Coherent Raman Scattering Spectroscopy

A variety of chemical and molecular-level properties of biological materials can be measured by their spontaneous Raman scattering spectra. Spontaneous Raman scattering originates from vibrational modes of molecular structures that can be excited by higher energy electronic states. Raman scattering can be associated with molecular vibrational modes which means it can be used to differentiate chemical species in a frequency selective way without requiring fluorescent dye labeling. Raman scattering has general uses in analyzing compounds to discover their constituent chemicals. Raman scattering in biological samples has the same mechanism as that involved in fiber nonlinear propagation already described intensively in previous sections, except for the different material properties and thus different characteristic resonance signatures. Raman scattering is an inelastic scattering process in which the emitted photon is red-shifted by anywhere from <1000 cm^{-1} to >4000 cm^{-1} for most biomedical samples.

Theory of Coherent anti-Stokes Raman Scattering

The spontaneous Raman spectrum of a sample can be recorded by a sensitive spectrometer when the sample is illuminated by an excitation laser source. However, the efficiency of spontaneous Raman emission is extremely low and the relative strength of the Raman component in the measured spectrum is very small, thus requiring a very sensitive spectrometer with very large dynamic range and long integration times. Coherent Anti-Stokes Raman Scattering (CARS) was demonstrated in 1965 [6]. The major advantage of CARS is the ability to coherently excite a Raman mode, producing a signal that is stronger than spontaneous Raman by several orders of magnitude. [6, 89-94]. The CARS technique also permits 3-dimensional sectioning of a biological sample by way of the nonlinear dependence on excitation intensity, which does not occur with conventional one-photon Raman techniques.

Theory of Coherent anti-Stokes Raman Scattering

CARS is a member of the class of Raman emission mechanisms generally referred to as Coherent Raman Scattering (CRS). CRS is a useful mechanism for spectroscopy and microscopy, with the ability to probe vibrational resonances of molecules and thus provide imaging contrast without fluorescence labeling [15-16]. CRS effects are based on nonlinear mixing between pump, probe and Stokes waves. The efficiency of CRS is proportional to the square of the optical power density of the pump, and thus tight focusing intrinsically provides a sectioning function for microscopy [95-96]. Biomedical spectroscopy and 3-dimensional imaging have been demonstrated with both coherent anti-Stokes Raman scattering (CARS) [95-96] and stimulated Raman scattering (SRS) [97-98]. CARS originates from a four-wave mixing process between the pump at frequency ω_p and the Stokes signal at frequency ω_S. An anti-Stokes signal is generated in the sample through the nonlinear Raman process, and it has a frequency of $\omega_{as} = 2\omega_p - \omega_S$. An energy level diagram of this process is shown below.

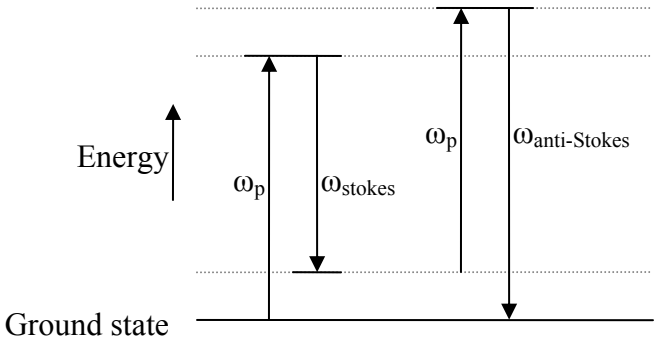

Figure 51. CARS energy level diagram.

The amplitude of the anti-Stokes beam is proportional to the 3rd order nonlinear susceptibility of the material, $\chi^{(3)}$. SRS is a method of probing the 3rd order susceptibility by which the high frequency pump transfers part of its energy into the lower frequency Stokes through the nonlinear Raman energy conversion in the sample, thus introducing a stimulated Raman gain

(SRG) in the Stokes and stimulated Raman loss (SRL) in the pump [15, 97]. Both CARS and SRS spectroscopy and imaging require short optical pulses to provide enhanced nonlinear response, as well as a continuously tunable wavelength difference between the pump and the Stokes in order to probe the Raman signature over a wide enough frequency window. In addition, the pulse repetition rate and the pulse arrival time between pump and Stokes have to be precisely synchronized to ensure optimal pulse overlap to maximize nonlinear mixing between them.

CARS Fiber Laser System Description

A typical CRS system uses two feedback controlled Ti:Sapphire lasers or two optical parametric oscillators (OPO) driven by the same pump to generate synchronized pump and Stokes pulses with different wavelengths [95-99]. Ti:Sapphire lasers are relatively bulky in size, and the tuning of their wavelengths through mechanical adjustments is generally slow and lacks repeatability.

Recent advancements have made fiber-optic lasers highly reliable and relatively low-cost, and fiber laser-based excitation system would significantly simplify CRS microscopy. Unfortunately, continuous wavelength tuning of femtosecond fiber lasers over a wide window has not been achieved so far. Precise synchronization between two passively mode-locked fiber lasers also remains a challenging task. The optical power of a femtosecond fiber laser in the 800 nm wavelength region is usually lower than that of a Ti:Sapphire laser, so efficient utilization of pulse energy in the CRS process is critical when a fiber laser is employed.

The goal of the following experiments was to demonstrate a CRS excitation source based on a single femtosecond fiber laser. Wavelength tuning between the pump and the Stokes was accomplished with soliton self-frequency shift (SSFS) in a photonic crystal fiber (PCF) [79, 100].

Wavelength shifting of femtosecond optical pulses based on SSFS has been studied and described in detail in previous sections. [41-42] Efficient wavelength shifting based on SSFS requires short optical pulses to be used, and in fact the efficiency of SSFS is proportional to $1/\Delta\tau^4$ for a given pulse energy, where $\Delta\tau$ is the temporal width of the pulse. Unfortunately, the short temporal width implies a broad spectral linewidth resulting in poor spectral resolution in CRS spectroscopy that is not adequate for most biomedical applications. This problem is solved in the following design by the application of identical linear frequency chirp on the pump and Stokes pulses to significantly improve the spectral resolution. The CARS spectrum of cyclohexane was measured with a spectral resolution of approximately 30 cm^{-1} using this single-laser excitation source based on a femtosecond fiber laser. Cyclohexane is a useful sample for testing and calibrating the CARS system, because it is optically transparent and has a well-defined Raman spectrum spanning wavelength ranges useful in biology.

CARS Experimental Setup

The experimental CARS spectroscopy setup is shown in Figure 52. Figure 52 shows the experimental configuration with controllable Stokes wavelength (λ_S) and pump-probe pulse relative delay (δt). A fiber laser (IMRA Femtolite-100) generates 120 fs pulses at 806 nm with approximately 9 nm spectral linewidth, 100 mW average optical power and 75 MHz repetition rate, corresponding to a pulse energy of approximately 1.3 nJ. This laser output is split into the pump and the Stokes paths. The pump passes through a motorized delay stage (Opto-Sigma) and passes twice through a 5 cm-long glass rod (Schott SF-6) for pulse chirping. The Stokes path has a voltage-controlled variable optical attenuator (VOA) which controls the optical power that enters a 2 m-long photonic crystal fiber (PCF) (Crystal Fiber NL-PM-750). By changing the applied voltage on the VOA, the wavelength of the Stokes could be varied from 850 nm to 1200

nm through SSFS [101]. The average optical power of the wavelength-shifted fundamental soliton at the PCF output is approximately 4 mW in the vicinity of 1000 nm, corresponding to a pulse energy of 53 pJ. In principle, the pulse-to-pulse wavelength stability of the soliton output can be affected by intensity noise and power fluctuations of the source laser. Based on the power-wavelength characteristic of SSFS, a 0.1 % RMS relative intensity noise of the fiber laser produces on the order of 0.05 nm RMS wavelength error, which has negligible impact in the CARS measurement. A long-pass filter after the PCF blocks the residual power at 806 nm wavelength as well as the 2nd-order soliton generated below 850 nm. Another 5-cm SF6 glass rod in the Stokes path has both end surfaces partially coated with gold so that the Stokes beam can fold back multiple times inside the rod.

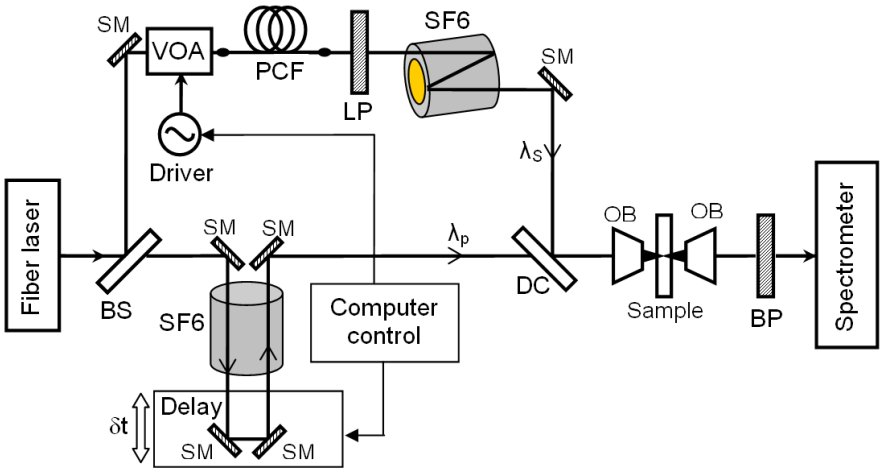

Figure 52. CARS system configuration.
The Stokes beam is labeled as λ_S and pump-probe pulse relative delay is labeled δt. The components include beam splitter (BS), silver mirrors (SM), photonic crystal fiber (PCF), long-pass filter (LP), SF-6 glass rods (SF6), dichroic beam combiner (DC), objective lenses (OB) and a band-pass filter (BP).

The pump and the Stokes pulses are then combined with a 45^{O} incidence dichroic filter and focused within the sample by a pair of objective lenses (Nikon 20x) in the confocal configuration. A bandpass filter rejects the pump and the Stokes components, and the anti-Stokes light is captured by a spectrometer (Ocean Optics). A laptop computer was used to control the

Stokes wavelength through the VOA and the relative pulse delay between pump and Stokes via the motorized delay stage.

Liquid cyclohexane was used as the sample for the CARS measurement because of its well known Raman signature. In this measurement, we were particularly interested in the two closely spaced C-H stretches at wave numbers around 2923 cm^{-1} and 2853 cm^{-1}. For transform-limited pump and Stokes pulses, the spectral resolution, $\Delta\upsilon_c$ of CARS is generally determined by $\Delta\upsilon_c = \frac{1}{c}\sqrt{1/(2T_p)^2 + 1/(2T_s)^2}$ where, T_p and T_s are the temporal widths of the pump and the Stokes pulses, and c is the speed of light. With the 120-fs pump and Stokes optical pulses in our laser system, the spectral resolution would be approximately 200 cm^{-1} which is not sufficient to resolve the two C-H stretches of cyclohexane separated by only 70 cm^{-1}.

One straightforward way to improve spectral selectivity would be to use a narrowband optical filter to reduce the spectral linewidth of the excitation source [102]. However, this would significantly reduce the pump and probe optical power, and would not be acceptable for the fiber laser-based excitation system which is often limited by the available power. Another technique to improve the spectral resolution is to apply a linear chirp on the optical pulses [93, 103-105]. In previous work, due to the lack of an efficient wavelength tuning mechanism, broadband Stokes pulses were often used to cover the spectral window of interest, either with ultra short optical pulses (<50 fs) or with supercontinuum generated in PCF.

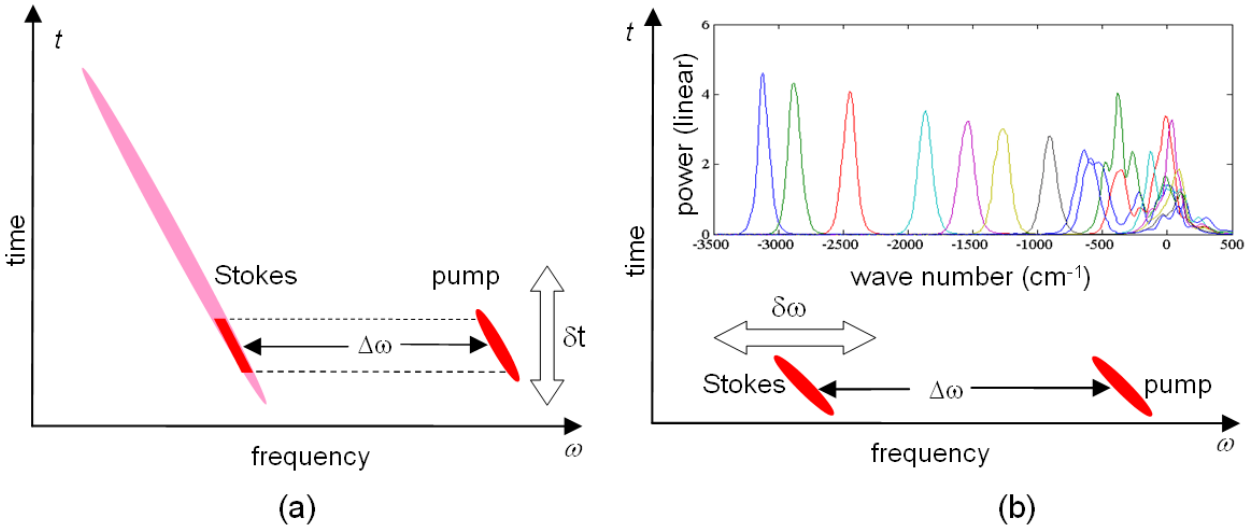

Figure 53. Pulse frequency chirp diagram for CARS.

Figure 53 shows an illustration of linear frequency chirp for coherent Raman spectroscopy (a) with wideband but fixed-wavelength Stokes and (b) with wavelength tunable Stokes. The inset shows examples of the soliton self frequency shift introduced with power control. With linearly chirped optical pulses, a frequency scan of $\Delta\omega$ between the pump and the Stokes can be accomplished by a time scan of δt as illustrated in Figure 53(a). Although the wide bandwidth, linearly chirped Stokes pulses may cover a large portion of the Raman spectrum for CARS spectroscopy [93, 104-105], at any particular moment only a small fraction of the Stokes spectrum overlaps with the pump in the mixing process, while the Stokes power outside this time-overlapped region is wasted. By comparison, in our excitation system the temporal and spectral widths of the pump and the Stokes are approximately matched, as illustrated in Figure 53(b). This ensures the maximum level of overlap between the pump and the Stokes pulses in the nonlinear mixing process, and thus maximizes the power efficiency, which is a key requirement of the fiber laser based CARS system.

Data Collection and Processing of CARS Measurements

In the CARS system, a sample mounted on a translation stage can be moved along the z direction with a micrometer dial. Figure 54 shows an example of measured anti-Stokes signal as a function of the z position of a sample with a resolution of 3 μm. This particular example was obtained from a mouse brain tissue sample mounted on a glass slide, and the Stokes frequency offset was tuned to target a lipid Raman response at 2880 cm^{-1}. Both the cover slip and the mounting slide are ordinary silica glass. The cover slip is on the side of the incident beam. The first signal, as z increases in the figure below, is non-resonant background from the cover slip, followed by the resonant signal from the 10 μm thick specimen layer (occurring at roughly 0.3 mm), followed by non-resonant background from the slide glass. This scan shows that anti-Stokes signal power fluctuates over time even in the solid glass volume. This small fluctuation can be partially attributed to time jitter in the Stokes pulses, as well as insufficient signal to noise ratio (SNR).

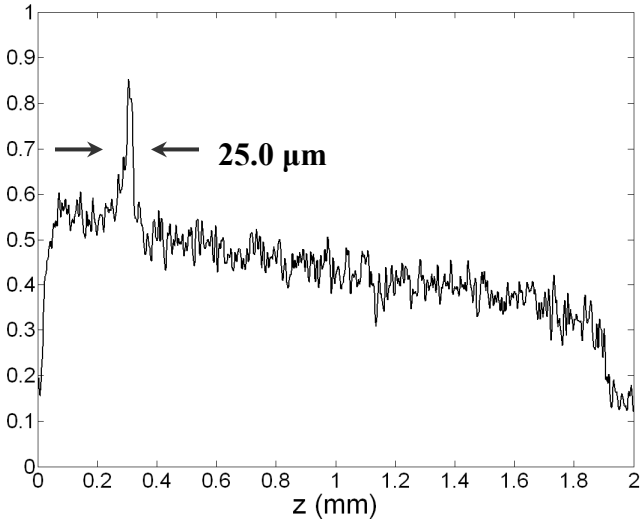

Figure 54. Cross section of CARS signal in slide mounted specimen.

The CARS spectrum of a material resembles, but is not identical to, the underlying Raman resonance spectrum of the material. As with most spectral measurement methods, a number of steps are required to extract the CARS signal spectrum from raw measured data. For each data

point, the control program saves the spectrometer trace, time of measurement, total power transmitted by the specimen, position of the delay stage with 2 μm resolution, and voltage values of the electro optic modulator and 2 dimensional translation stage inputs. By design, data can be collected up to a size of roughly 200 by 200 points, although this could be expanded. For some purposes, several data sets must be combined after collection.

There are two data collection modes. The first mode is for CARS spectroscopy at a fixed focal point in the sample. In this mode, the Stokes wavelength and delay stage position are scanned over the ranges necessary to obtain a complete CARS spectrum. The second measurement mode is for CARS microscopy, in which a 2-dimensional Piezo-electric translation stage, which holds the sample, is scanned to obtain the CARS-contrasted image in a plane within the sample. A screen capture of the custom interface that accomplishes all the needed tasks for CARS measurement is shown in Figure 55. The interface also has a spectrum display designed to simplify alignment and signal-finding.

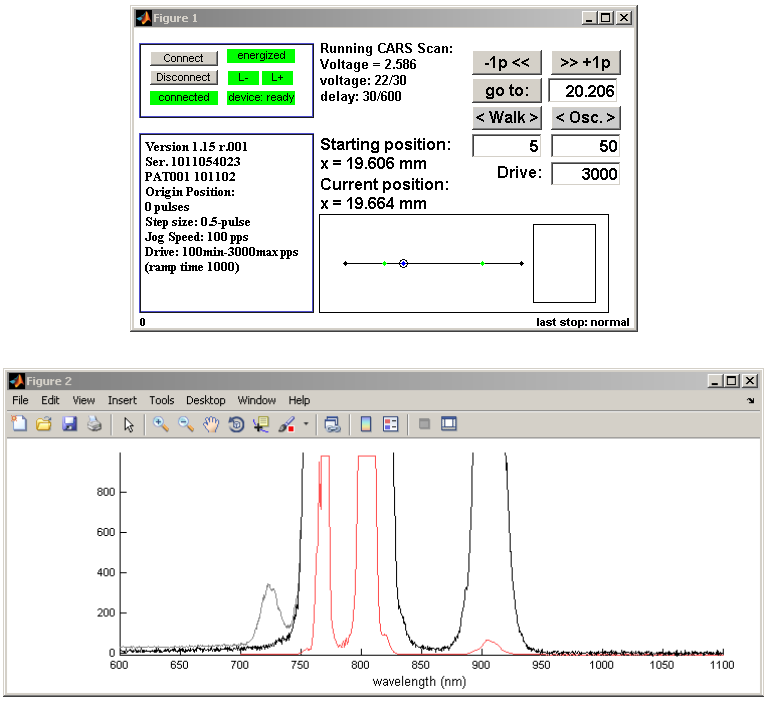

Figure 55. CARS custom hardware control interface.

Obtaining a CARS spectrum requires tuning the Stokes wavelength and measuring the anti-Stokes signal amplitude while keeping the pump and Stokes pulses aligned in the time domain. During measurement, the wavelength is varied at each delay stage position, avoiding excess wear of the mechanical delay stage. The time-space dependence of the Stokes pulse is illustrated in Figure 56.

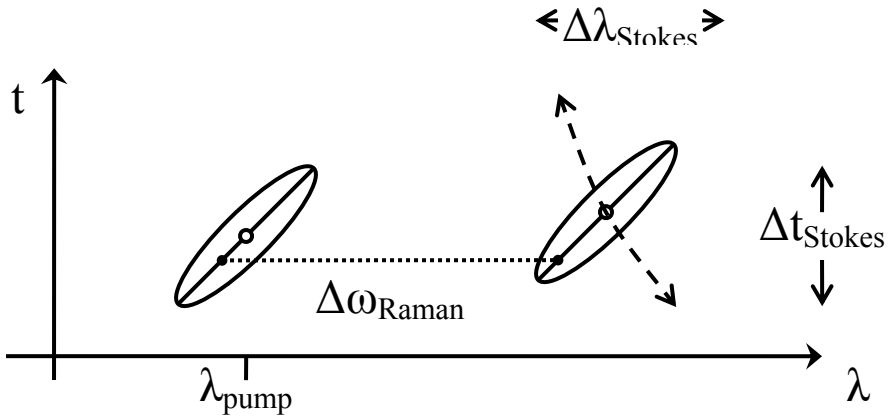

Figure 56. Relationship of Stokes wavelength and propagation delay.

The anti-Stokes signal will appear when these two values are properly set by varying the relative pulse delay between pump and Stokes and the wavelength of the Stokes pulse. However, the values of optimum relative pulse delay and the control voltage on the electro-optic modulator to maximize the peak anti-Stokes amplitude are not always predictable. This is because the relationship of the control voltage on the modulator and the actual Stokes wavelength does not remain fixed; instead, it depends on the power coupling condition between the laser and the PCF, which may vary over time. Furthermore, for a sample material with multiple closely spaced Raman resonance peaks, the amplitude of the anti-Stokes measured at a certain wavelength has contributions from multiple Raman resonances. In other words, the measured anti-Stokes amplitude at a certain wavelength may be over-emphasized if there are other Raman resonances nearby. However, if the pulses have the required frequency chirp to singularly excite resonances, a global peak can be found for each Raman resonance frequency where both of the following conditions are met: 1) the pump and the Stokes pulses are precisely aligned in time and 2) the frequency separation between the pump and the Stokes is exactly at the Raman resonance frequency. The measured CARS spectrum can thus be displayed as functions of pulse delay and Stokes wavelength. The optimum setting of relative pulse delay and the Stokes wavelength corresponding to each anti-Stokes wavelength can be obtained through a curve fitting of this data. In order to ensure the accuracy of Raman resonance frequency measurements, the wavelengths of the pump and the Stokes need to be measured as precisely as possible, which is sometimes complicated by the fact that the pump intensity entering the spectrometer is usually extremely high, and its central wavelength may thus be hard to determine.

A Z-plane image can be made by translating a three dimensional sample in the X and Y coordinates with a Piezo-electrically controlled translation stage. In the Z-plane imaging mode,

measurements are made over a uniform rectangular grid of X and Y coordinates. The delay and wavelength can be adjusted during measurement, but they generally remain fixed unless thermally or mechanically introduced fluctuations are significant, necessitating some adjustment during the recording.

Note that in the measurement setup, a spectrometer was used as the receiver, which records the entire optical spectrum for each delay and Stokes wavelength setting, while the useful information is discrete including the pump and Stokes wavelengths and the amplitude and wavelength of the anti-Stokes. Therefore, once this data has been collected, peak searching can be used to extract the useful information and greatly reduce the data size. Peak finding routines were used to estimate the central wavelength, bandwidth and intensity level of the pump, Stokes and anti-Stokes signals. An example of a trace in the peak finding output is shown in Figure 57. The triangle in the figure shows the expected value (mean) wavelength when calculated over the FWHM span.

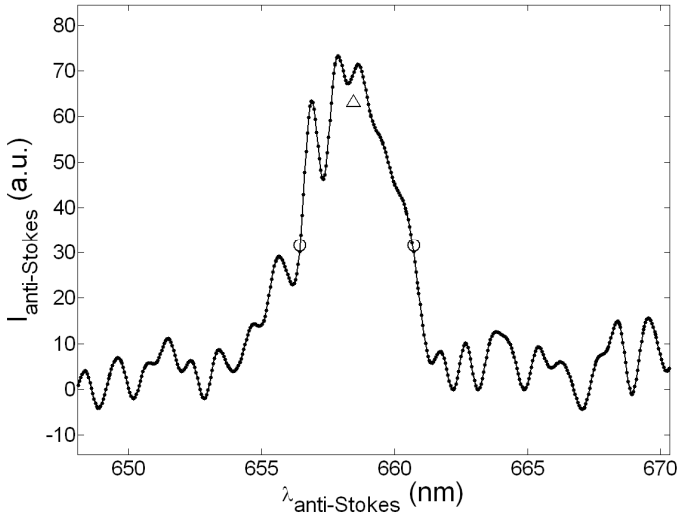

Figure 57. Peak search example at very low SNR.

Initially, any signal level is considered valid, even if the anti-Stokes signal is absent and the spectrometer trace is only noise. In subsequent steps, a minimum intensity threshold is used to

single out occurrences of anti-Stokes signals above the noise floor. Peak finding greatly reduces the data size without discarding useful information, because only the strength and wavelength of the CARS signal contains information useful in the later steps. After reducing the data size into secondary data sets, multiple runs were stitched together. The relative change of Stokes wavelength versus time over 1.5 hours is shown in Figure 58, during which the wavelength control setting was not changed. This demonstrates the unavoidable variability of the Stokes wavelength over time. The process of obtaining a CARS spectrum involves interpolating the anti-Stokes intensity as a function of the frequency difference between the pump and Stokes. Wavelength values must be unique and monotonic for interpolation. Therefore, some values have to be discarded and various approaches are needed to assemble a useful subset of signals forming a CARS spectrum.

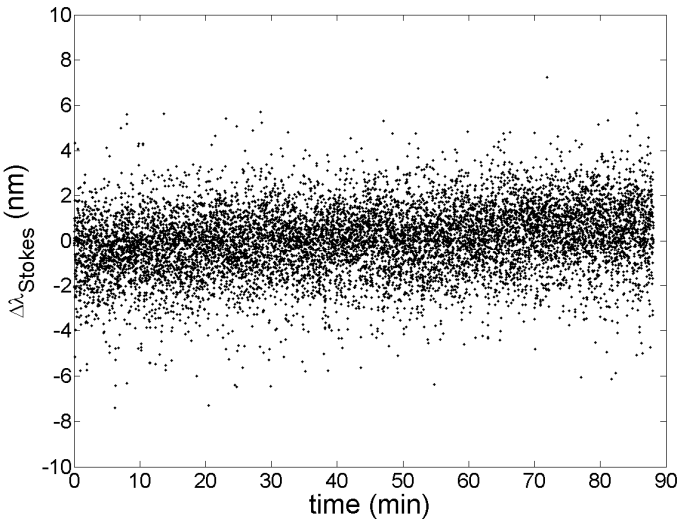

Figure 58. Stokes wavelength change over time.

For the Z-plane imaging application, the translation stage (Mad City Labs Nano-H) was used in a horizontal configuration, meaning that the direction normal to its X-Y positioning plane was horizontal. In other words, changing the Y position involved moving the stage against the force of gravity, while the X-positioner may have experienced an extra vertical hanging load. It was

assured by the manufacturer (Mad City Labs) that this was appropriate use and well within the designed tolerances of the stage. To mitigate any scan misalignment problems due to hysteresis of the Piezo-mechanical stage, a triangular raster pattern of the X and Y scan coordinates was used in order. However, some hysteresis of the translation stage did occur. The amount of offset can be found by cross correlation between adjacent lines in the image and removed by interpolation. An example of the scan-by-scan offset history is shown in Figure 59 for a data set of 100 scans. It shows that the triangular scanning pattern resulted in an alternating lag of up to 4 μm.

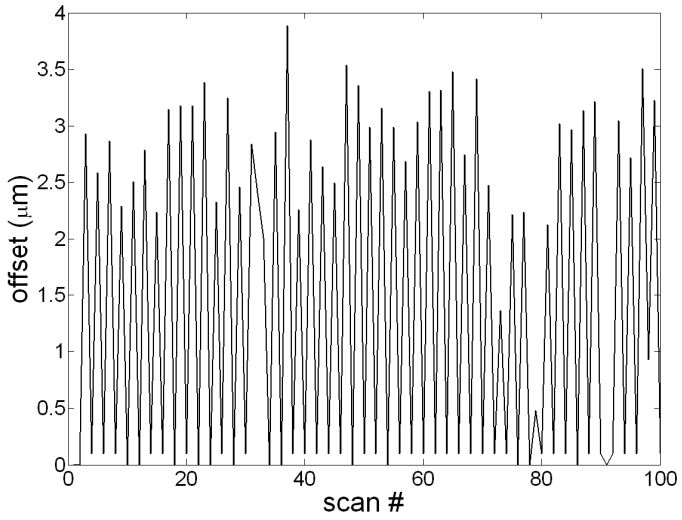

Figure 59. Hysteresis of the translation stage.

It was found that fluctuation of the optical power coupled into the fiber, mostly caused by instabilities of the laser-to-PCF coupling apparatus and variation of the laser output power, caused some variation of the soliton wavelength. While the relative power change may be very slight, the soliton wavelength is very sensitive to the input coupled power, and most importantly the timing of the Stokes pulse is in turn very sensitive to the soliton wavelength change when compared to the pulse duration. Therefore, slight fluctuations in the laser power coupled into the fiber produce problematic walk-off between pump and Stokes pulses. The histogram of the laser

power measured over time is shown in Figure 60, with binning into 100 slots. The power measurements (abscissa values) in this figure were normalized to represent percentage of the average power.

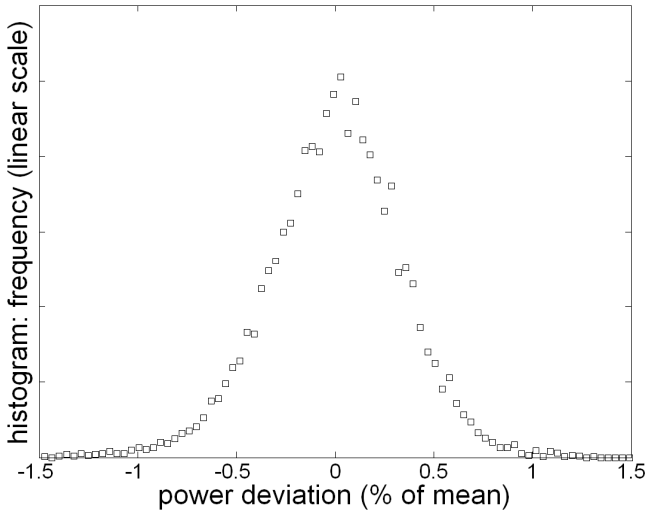

Figure 60. CARS excitation power distribution.

Figure 61 shows anti-Stokes intensity values from a Z-plane scan in which the Stokes frequency was not tuned. It illustrates the effect of pulse-jitter on the anti-Stokes signals. The instability of the Stokes wavelength creates pulse walk-off between the pump and Stokes, with a resulting characteristic wavelength-dependent reduction of the anti-Stokes intensity.

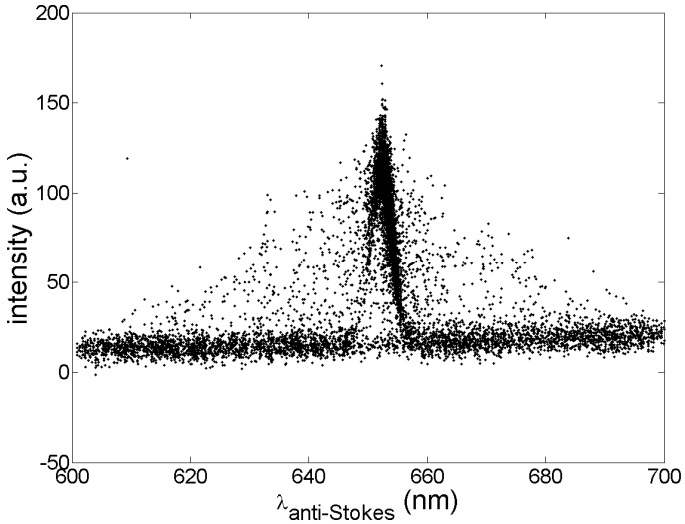

Figure 61. Jitter-related intensity spread.

Figure 61 indicates that both the intensity and the wavelength of the anti-Stokes vary due to the pulse timing jitter. To attempt to correct this, the signal was fitted by a Gaussian curve as shown in Figure 62.

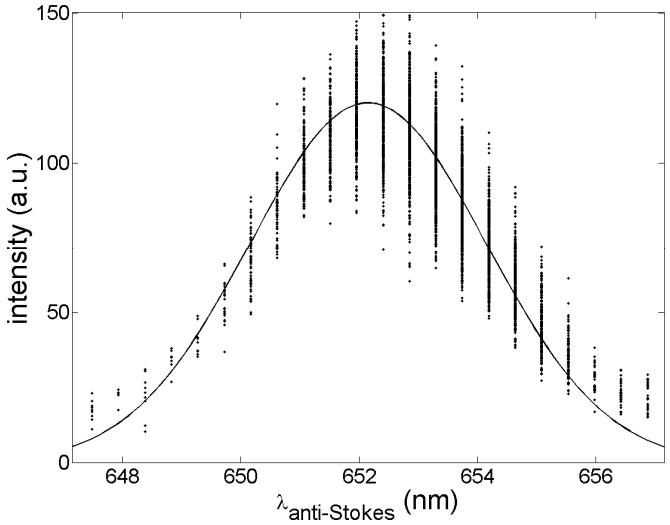

Figure 62. Jitter correction curve.

After normalizing by the jitter correction curve, the intensity dependence was reduced, as the data in Figure 63 show.

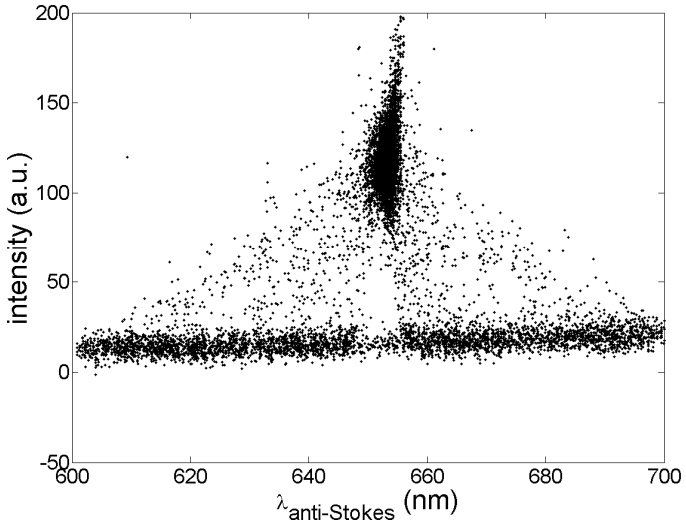

Figure 63. Anti-Stokes intensity after jitter correction.

Care has to be taken noticing that normalizing the signal intensity without regard to the anti-Stokes wavelength may lead to false interpretation of the resonance response. Some part of the wavelength dependence is due to the resonance line-shape and not the pulse jitter. It must be remembered that the points shown in Figure 61 represent values found everywhere within the z-plane image. Equalizing the intensities thus has an effect on the quality of the image contrast based on the presence or absence of anti-Stokes response. It is important to isolate the changes of anti-Stokes response that stem from the sample's Raman contribution from those due to timing jitter. The greatest contrast results when the anti-Stokes signal has the widest range of values, which appears to occur at a wavelength of roughly 655 nm in Figure 63.

Finally, care was taken to remove any impact on the anti-Stokes intensity by power fluctuations of the pump beam. Because the CARS process is a nonlinear mixing process, the variation of pump power over time affects the anti-Stokes signal by the square of its intensity fluctuation. Due to the limitations of the hardware, the most convenient way to estimate the relative pump power at the exact time of the spectrum acquisition is to correlate it with the measured Stokes wavelength found in the same spectrometer trace reading. In the particular system used in this experiment, the approximate relationship between the pump power and Stokes wavelength between 1000 nm and 1050 nm was

$$P_{pump} \approx 1.390 \cdot 10^{-4} \cdot \lambda_{Stokes} - 0.080 \quad mW \qquad (98)$$

where λ_{Stokes} is in the unit of nanometers. A correction factor was applied using this equation. Inspection of the values showed that the pump and Stokes power variation caused less than 5 % anti-Stokes intensity variation.

CARS Spectrum Data Preparation

The CARS spectrum is usually graphed on a frequency axis as a function of the Raman shift frequency. The Raman shift, usually measured in the unit of wavenumbers (cm^{-1}) is given by

$$\Omega_R = 1/100 \cdot \left(1/\lambda_{pump} - 1/\lambda_{Stokes}\right) \qquad cm^{-1} \tag{99}$$

The initial image is based only on the voltage and stage position values as shown in the figure above. Figure 64 was taken from a sample of mouse brain tissue and shows the intensities of anti-Stokes power (located from a peak search for each point) as a function of the stage position and applied voltage on the EOA.

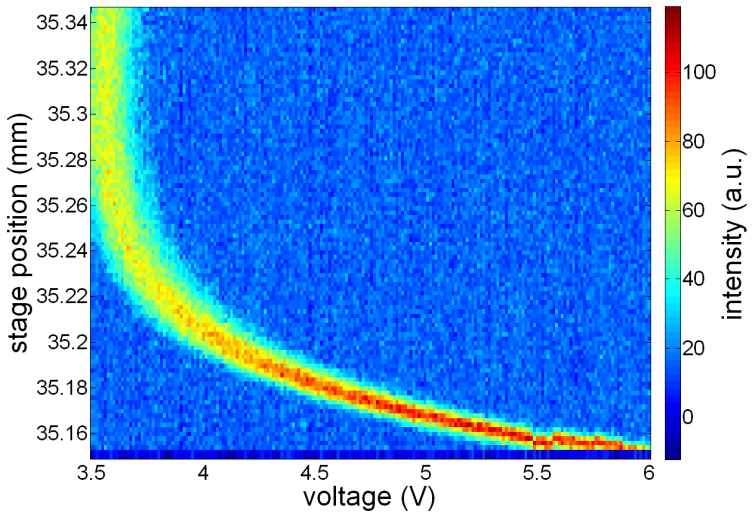

Figure 64. Anti-Stokes intensity data example.

The Raman shift must be calculated from the spectral data stored at each point. The characteristic curve of Figure 64 may vary after a long time. In general, the wavelength of the fundamental soliton varies as a function of the optical power at the fiber input. As a rough approximation, (98) gives the following conversion over the 1000 nm to 1050 nm range:

$$\lambda_{Stokes} \approx 7194\,(P_1 + 80 \cdot 10^{-6}) \qquad \text{(nm)} \tag{100}$$

where P_1 is a power meter measurement proportional to the attenuated laser power going into the fiber. In practice, in addition to this power dependence the voltage-to-wavelength response tends

to vary because of laser thermal instability and optical alignment drift. The relationship between PCF input power and the voltage applied to the electro optic attenuator (EOA) also has gradual variations. The EOA attenuation is modulated by changing the angle of optical signal polarization, which is converted into an intensity modulation through a linear polarizer. The output power of the EOA, which is proportional to the input power to the PCF, can be expressed as

$$P_1 \propto (P_{\max} - P_{\min})\cos(\theta_{inc})^2 + P_{\min} \tag{101}$$

where θ_{inc} (radians) is the polarization angle (from vertical) of the polarization modulator in the EOA, and $P_{\min}, P_{\max}$ (Watts) are the minimum and maximum transmitted power levels (allowing leakage and attenuation of the electro optic cell). The polarization rotation inside the EOA is related to the applied voltage as

$$\theta_{inc} = \left(\Re_{EO} \cdot V_c + \theta_0\right)^{P_L} \tag{102}$$

where $\Re_{EO}$ (rad/V) is an electro-optic responsivity factor, V_c (V) is the applied control voltage, θ_0 is an initial offset polarization angle and $P_L \approx 2.0$ is the power law of the electro-optical response.

The CARS spectrum is contained in the series of peaks in Figure 64. The Raman shift at each of those peaks now remains to be determined. A straightforward way is to use the measured Stokes wavelength and calculate the Raman shift according to (99). Because of the uncertainties in the wavelength control, sometimes the anti-Stokes wavelength values are not unique and they may not be in increasing order. Therefore, handling the original data requires discarding repeated values and sorting the sequence of scans into monotonically increasing data sets for each value of delay. Once this is done, the plot of anti-Stokes intensities at each delay position becomes similar to a spectrum. It is not a spectrum however; rather it is a collection of peak wavelength

and intensity values. As the delay is scanned incrementally, the wavelength dependence of the propagation delay of the PCF can be traced out (as long as an anti-Stokes signal is present). Using the Stokes wavelengths at each of these points, a two dimensional pseudo-spectral image (as shown in Figure 65) can be formed by interpolation and the Raman resonance frequency of an unknown sample can be accurately estimated. The key feature to note is that the series of strong peaks has now been straightened, because the spectrum was translated according to the Raman shift using interpolation.

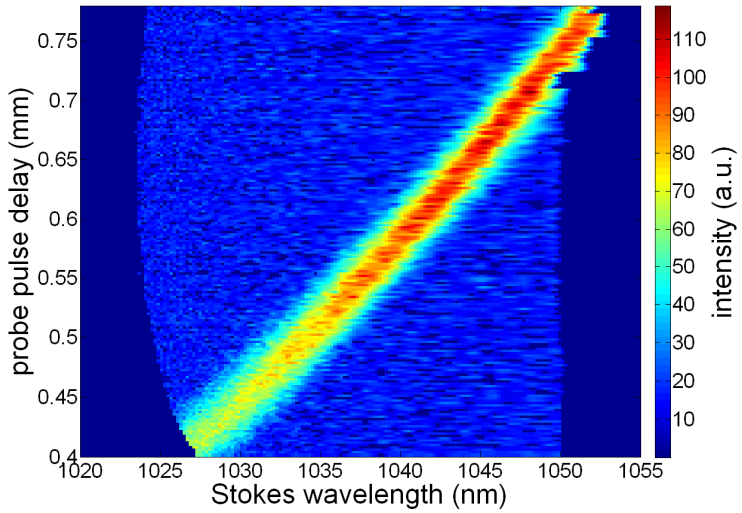

Figure 65. Anti-Stokes intensity interpolated for Stokes wavelengths.

According to the frequency relation between the pump, Stokes and anti-Stokes frequencies in the CARS mixing process, the CARS spectrum should be represented by a single linear trace interpolated along the high intensity diagonal line shown in Figure 65. This line of peaks appears in the figure, and bilinear interpolation was used to extract the values of intensity along the peaks. The remaining steps to obtaining the CARS spectrum included subtracting background levels and normalizing by the incident power, and finally stitching several data sets together to cover the complete range of delay and wavelength points. The maximum size of a data set that can be handled at once in the Matlab program is about 300 MB, which allows storage of spectra

over a 200 by 200 point grid. This results in a slow measurement process. However, with the knowledge of the optimum relative pulse delay as a function of the Stokes wavelength, it would be simple to speed up the operation by reducing the range of the delay scan to the vicinity of the bright diagonal line as shown in Figure 65. The signal could be maximized by moving the delay stage in as few as 5 steps for each voltage value, resulting in far fewer stored points and far less data.

CARS Measurements of Cyclohexane

This section discusses the experimental details and the major results of CARS measurements of Cyclohexane. In the experiment, SF6 glass rods (Schott Glass) were used to introduce pulse chirping. As the chromatic dispersion of the SF6 glass is higher for the pump at 806 nm than for the Stokes at around 1000 nm, the pump is passed through the 5-cm glass rod twice, while the Stokes is passed through the rod 3 times in a fold-back configuration. As a result, both the pump and the Stokes pulses were stretched to approximately 700 fs, improving the spectral resolution to approximately 30 cm^{-1}. When the SF6 glass rods were not used, the intensity of the generated CARS signal was enough to be seen by the naked eye. A digital photo was taken of the spot of CARS light, as it would enter the spectrometer aperture, caught on ordinary paper as a small red spot. The photo is shown in Figure 66 (a). To demonstrate that this was in fact only the CARS signal detected, another photo was taken immediately after, with the only change being an adjustment of the delay stage by the minimum amount necessary to time-offset the pump and Stokes pulses (Figure 66 b). This may be the first digital photograph of a CARS signal from a fiber laser system.

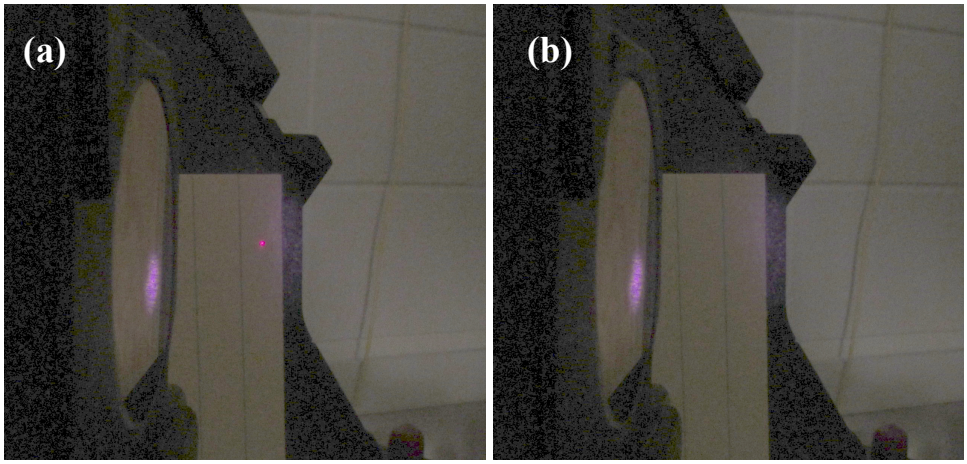

Figure 66. Photo of 655 nm CARS Anti-Stokes emission from Cyclohexane. (a: pulses time-aligned. b: pulses not time-aligned.)

Figure 67 shows color plots of the spectrum of measured anti-Stokes light originated from CARS as a function of the linearly scanned Stokes wavelength. The collections of spectral lines were taken with optimized pulse delay at each Stokes wavelength. The vertical axis is Stokes wavelength, which can also be interpreted as scanning of the Raman probing frequency. In both plots, the standard spontaneous Raman spectrum of cyclohexane [106-107] is shown by a white line along the anti-Stokes axis. In Figure 67 (a), pulse chirping was used and the two spectral peaks of cyclohexane are clearly separable as a function of the Raman probing frequency. As a comparison, Figure 68(b) shows the same measurement but with both SF6 glass rods removed from the optical paths. As expected, without linear chirping the spectral resolution is poor and it is not possible to resolve the two closely spaced vibrational Raman peaks. Principally, in each figure the CARS spectral information lies along a diagonal line traversing the spectral peaks, and the intensity taken along these diagonal lines provides the CARS spectra, which are shown in Figure 68 (a) and (b) corresponding to Figure 67 (a) and (b), respectively.

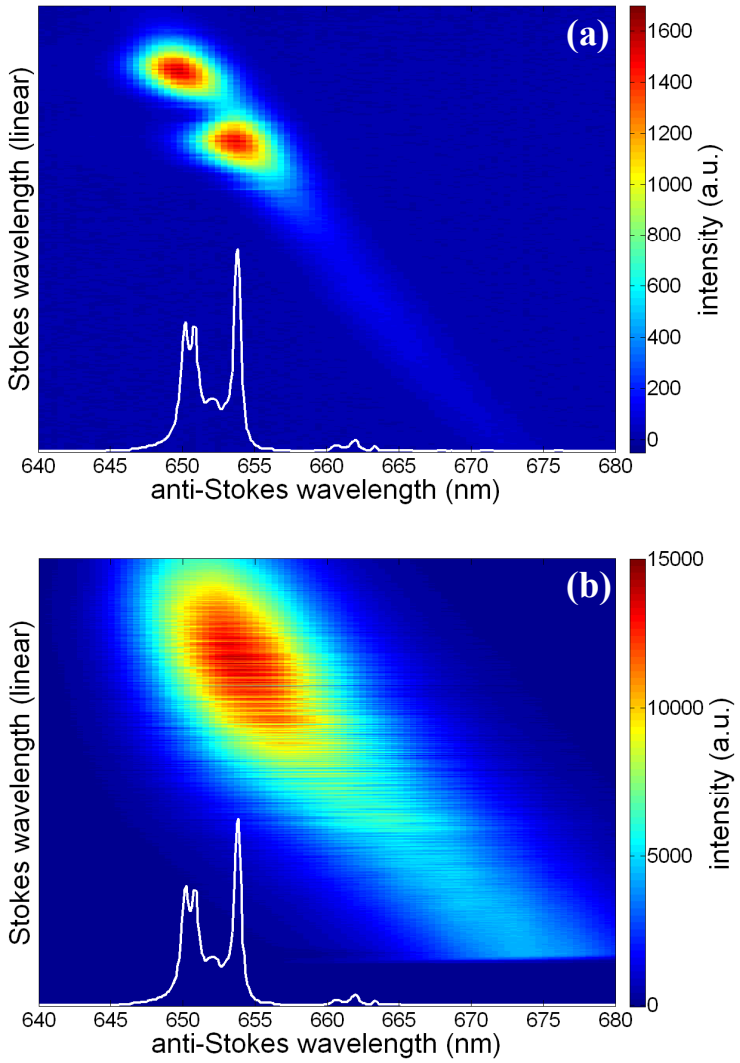

Figure 67. Anti-Stokes spectra of cyclohexane shown two-dimensionally. The vertical axis is Stokes wavelength, which can also be interpreted as scanning of the Raman probing frequency. Fundamentally, the important Raman spectral information is in the intensity values taken along a diagonal line in each image. The diagonal line can be pinned at two points by choosing the peaks of the horizontal spectral lines at two locations. The CARS spectra provided by interpolating (a) and (b) accordingly are shown in a following figure.

The results of interpolating a CARS spectrum from the diagonal line of peaks in Figure 68(a) and Figure 68(b) are shown in Figure 68, together with the reference Raman spectrum of cyclohexane [106-107]. Figure 68 (b) shows results without pulse chirping. In Figure 68 (a), the two C-H stretches of cyclohexane separated by 70 cm^{-1} are clearly separated with the help of

linear pulse chirping. It is interesting to note that in this measurement, the resolution of CARS spectroscopy is not determined by the spectral width of the anti-Stokes signal; rather, it is determined by the temporal width of the chirped pulses and the parallelism between the pump and the Stokes pulses in the frequency-time diagram as illustrated in Figure 53.

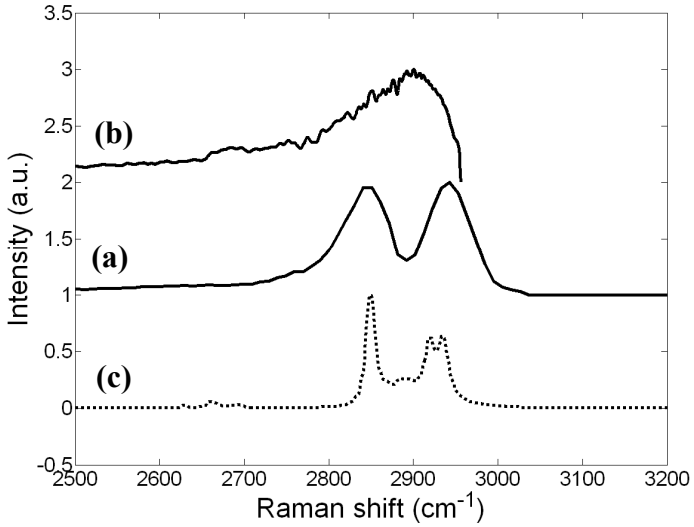

Figure 68. Anti-Stokes CARS (and Raman) spectra of cyclohexane.
(a) CARS spectrum of cyclohexane with pulse chirp.
(b) CARS spectrum without pulse chirp.
(c) Spontaneous Raman spectrum of cyclohexane. [106-107]

One practical issue in the CRS excitation source based on SSFS is the dependence of Stokes pulse propagation delay as a function of its central wavelength, which creates differential pulse walk-off between the pump and Stokes pulses during wavelength tuning. To obtain the results shown in Figure 68, we had to adjust the delay line to optimize the temporal delay between the pump and the Stokes pulses when the Stokes wavelength was tuned. Since the wavelength-dependent propagation delay of the Stokes is determined by the chromatic dispersion parameter of the PCF, which is deterministic, the computer-controlled delay stage in the measurement setup could effectively compensate for this differential pulse walk off.

Figure 69 shows the measured and calculated Stokes propagation delay through the 2-m PCF as a function of the wavelength. Due to the anomalous dispersion in the PCF, pulse group delay increases with the wavelength at the rate of approximately 106 fs/nm around 1000 nm Stokes wavelength. When the output Stokes pulses pass three times through the 5-cm SF6 glass (15.17 cm path length considering the beam angle inside the rod), which has normal dispersion in this wavelength, the overall dispersion slope reduces to approximately 68 fs/nm. The calculated group delays, shown as the continuous lines in Figure 69, were obtained through numerical simulations by solving nonlinear Schrödinger equations [41, 100] for soliton propagation in the PCF, and considering the linear propagation delay in the bulk SF6 glass. In the experiment, the time overlap between the wavelength-varying Stokes and the fixed-wavelength pump was adjusted by optimizing the anti-Stokes signal in cyclohexane. The measured pulse delay versus the Stokes wavelength is also shown in Figure 69 as the sections of thick lines.

CARS Delay Compensation

In the CARS spectroscopy measurement shown in Figure 68, the optimization of pulse delay at different Stokes wavelengths was accomplished by adjusting the mechanical delay line. In a situation where the Stokes wavelength needs to be modulated at a high speed, such as in FM CARS [95], mechanical delay may not be fast enough and the differential pulse delay between the pump and the Stokes pulses over the modulation range must be small enough so that feedback adjustment is not necessary. In principle, minimizing the differential delay can be accomplished through proper dispersion compensation. However, in practice the PCF and the dispersion compensator (in this case, SF6 glass) may have different dispersion slopes, and therefore the minimum differential pulse delay between the pump and the Stokes can only be maintained in the vicinity of a specific Stokes wavelength, depending on the length of the

dispersion compensator. The solid line in Figure 69 was calculated when the path length inside the SF6 glass rod was 44.5 cm. With this dispersion compensation, the maximum pulse delay variation is less than 300 fs over a wavelength window from 1000 nm to 1100 nm. Generally, this is suitable for FM CARS microscopy as the Stokes wavelength modulation only needs to be on the level of the linewidth of the molecular vibrational resonance, which itself should be much less than 50 nm. Therefore, the dispersion compensation from 44.5 cm of SF-6 glass should be sufficient.

In Figure 69, measured relative propagation delay versus wavelength is shown (thick lines) along with the calculated delay (thin lines).

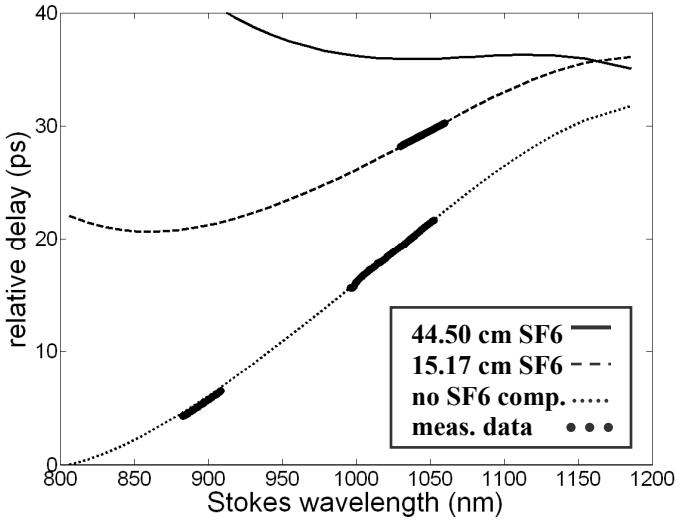

Figure 69. Relative pulse delay versus wavelength.
The dotted line represents no dispersion compensation (no SF6 glass bar), the dashed line represents dispersion compensation with 15.17 cm path length in SF6 glass (beam folded 3 times inside the 5 cm rod), and the solid line represents dispersion compensation with 44.5 cm path length inside SF6 glass for optimum operation around the 1000 nm Stokes wavelength. In order to accommodate the three curves in the same figure, the dashed and the solid lines have been shifted in their absolute delays by 905 ps and 2663 ps, respectively.

CARS Mouse Brain Tissue Experiments

While CARS spectroscopy measures the spectral characteristics of Raman resonances without changing the location of the light inside the sample, CARS microscopy refers to application of

the system to create a spatial image. To do this, in CARS microscopy the frequency separation between the pump and the Stokes is set to a steady value so that one vibrational band of the material is probed, while the focal point in the sample is spatially scanned to obtain the CARS image which thus translates to an image with biochemical contrast. In this experiment, mouse brain tissue was used as the specimen. Lipid distribution in mouse brain tissue has been an important biomedical feature of interest for disease prediction [108-109].

The primary purpose of the CARS system is acquisition of useful information from biological specimens, hopefully including imaging with a biochemical contrast. The sample of brain tissue obtained from mouse is a commonly used subject and one for which lipid identification has been an important concern [108-109].

A mouse brain tissue (MBT) sample of 10 μm nominal thickness was mounted on silica glass in water. Unlike the FRET experiments which are highly pH-sensitive due to protein activity, the MBT sample could be mounted in either glycerol or water. Although glycerol is preferable because it does not evaporate as rapidly as water, it unfortunately has a strong Raman signature in the same spectral region as a lipid. Therefore, the MBT samples were mounted in water. A diagram of the brain section, which is illustrated by the image inset approximately, and an image under optical microscope with standard illumination are shown below. The tissue is porous and has some void channels.

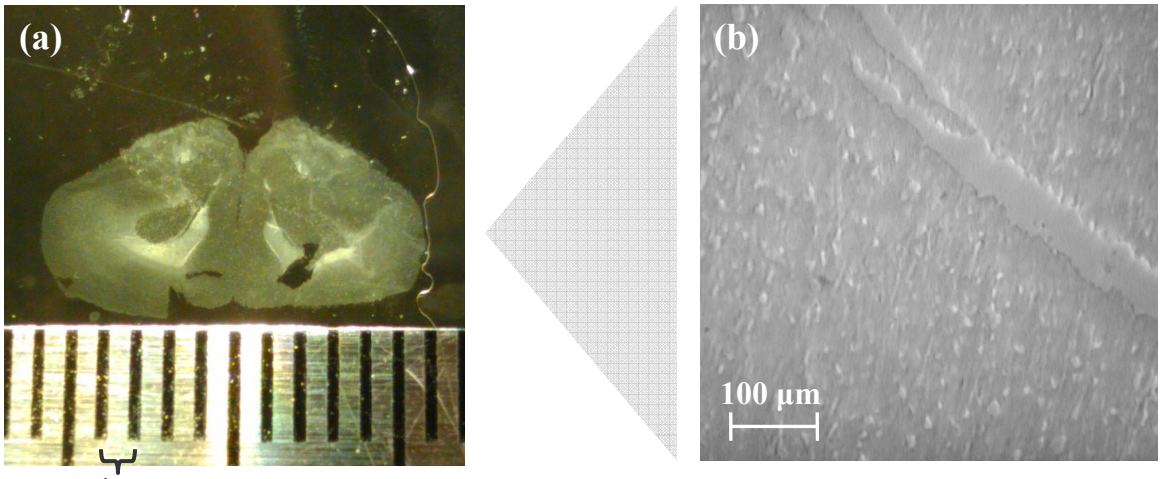

Figure 70. Example bright field images of mouse brain tissue. (slice thickness: 10 µm)

Compared to the transparent optical characteristics of cyclohexane or other liquids, the rough surface structure and opacity of tissues both significantly encumber CARS measurement. Transmission at various wavelengths is reduced because of the attenuation through the sample, while the rough surface has the effect of defocusing the excitation beam and thus reducing the photon density at the focal point. At the same time, the anti-Stokes wave generated at the focal point is also scattered by the rough exit facet and cannot be fully collected by an objective lens with limited numerical aperture (NA ≈ 0.4 in this experimental setup). The impact of de-focusing and scattering varies from location to location across the sample which will be superimposed on the CARS image. A rigorous way to isolate the CARS response from scattering and de-focusing is to normalize one image, taken with stimulating frequency tuned on the strong Raman resonance, by a second image taken with the frequency tuned off the Raman resonance. To demonstrate that such a CARS resonance contrasts can in fact be obtained in this system, a reference CARS spectrum was measured at a single point within the tissue sample. The CARS spectrum was obtained by slowly scanning the Stokes frequency and the measured anti-Stokes amplitude was normalized by the excitation power and other variables as described in the

previous section. This measured CARS spectrum, shown in Figure 71 below, demonstrates similar spectral features as those reported in [109]. The CARS spectrum of [109] was measured using a high power laser and lenses with much higher resolving power and numerical aperture. Therefore, the CARS spectrum below represents spatially averaged multiple lipid CARS responses, rather than a single specific lipid construct.

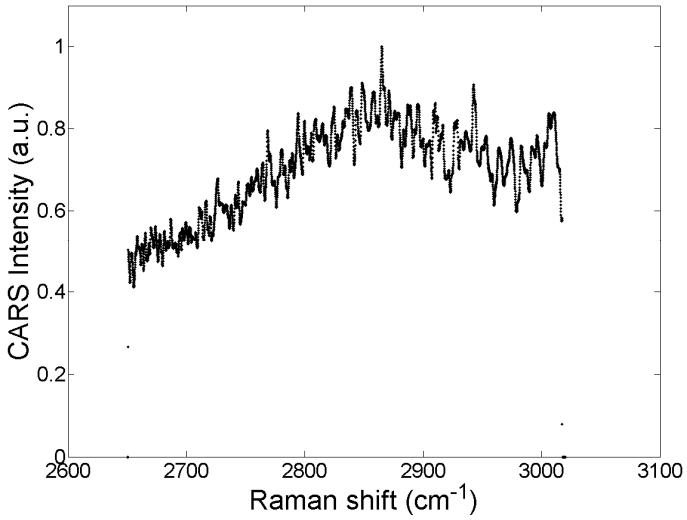

Figure 71. CARS spectrum of mouse brain tissue.

The Z-plane images are shown in Figure 72. Figure 72(a) shows the measurement of pump transmission, which roughly shows the physical structure but also includes blur from scattering outside the focal volume. Figure 72(b) shows the anti-Stokes contrasted image. The Stokes beam was turned on with the Raman shift tuned to 2650 cm^{-1} (off-resonance) and then 2835 cm^{-1} (on-resonance), respectively, and the amplitude of anti-Stokes was measured accordingly. The two images measured on-resonance and off-resonance were subtracted to find the resonance contrast which is shown in Figure 72(b).

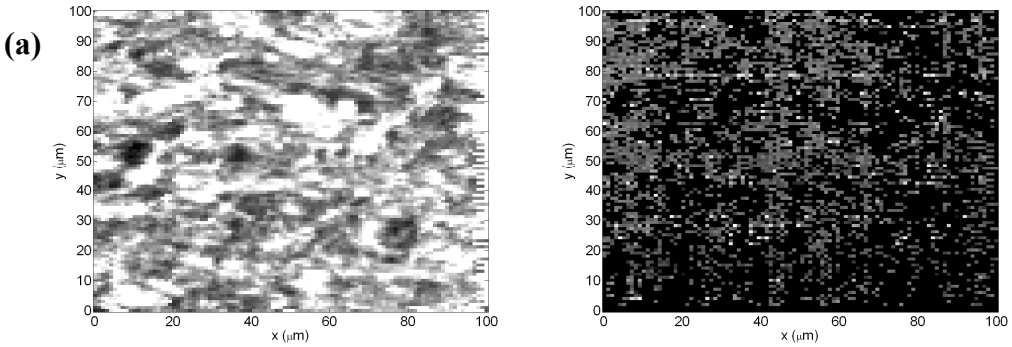

Figure 72. Mouse brain tissue images.
(a): opacity (b): resonance contrast

Unfortunately, the data shown Figure 72 (b) is not useful because the resonance contrasted image is obscured by measurement noise and excitation instabilities. The inability to produce a clear image is primarily attributed to the low signal to noise ratio in the measured anti-Stokes amplitude, and thermal fluctuation of the laser which caused instability of the Stokes pulse delays during image acquisition. With active feedback control of the delay stage and the Stokes wavelength, the standard deviation of the pulse delay instability could be kept below the pulse width during the X-plane scanning operation.

V. Conclusions

Nonlinear Raman spectroscopy and imaging based on fiber lasers and nonlinear fiber optics is a challenging but realizable goal. The study of nonlinear optical propagation remains a deeply interesting and rich field, and the investigations in this report have attempted to bridge the gaps between analytic, numerical and experimental results. For practical purposes, every attempt has been made, as described in this report, to reach the end goal of applying theories and physical phenomena to the purpose of designing a simple and practical nonlinear spectroscopy system.

Summary of Completed Work

This work presented the theoretical foundation of nonlinear propagation in optical fibers, with in-depth investigation of soliton propagation in the highly dispersive and nonlinear regime. Two principal spectroscopy systems were designed, namely a Coherent Raman Scattering measurement system and a two-photon Förster Resonance Energy Transfer (FRET) system.

Central to these techniques was an electrically controlled wavelength tuning apparatus utilizing the phenomenon of soliton wavelength shift of femtosecond optical pulses in a photonic crystal fiber. In this report, investigations of soliton propagation were devoted to the characterization of the wavelength shifting system and the performance optimization of rapidly tunable wavelength-shifting femtosecond light sources, and some useful guidelines for future designs and system applications in nonlinear Raman spectroscopy and microscopy were provided as well.

To improve the spectral resolution of CARS, a pulse linear frequency chirping scheme was developed which achieved an excitation spectral resolution of 30 cm^{-1}. The CARS spectrum of cyclohexane was measured and its two vibrational Raman resonance peaks separated by 70 cm^{-1} were clearly resolved, thus overcoming a difficult power and resolution tradeoff of fiber laser based systems.

In the application of FRET efficiency measurement, which is a powerful quantitative tool for measuring molecular-level structure, two important varieties of biological samples were characterized. The FRET efficiencies of Calmodulin protein labeled with localized fluorescent dyes, as well as a custom engineered linked mCherry-Enhanced Green Fluorescent Protein were measured. The results of two-photon and one-photon excitation measured using the FRET system were in agreement with those of the controls and previous studies. In addition, new two-photon spectra of the fluorescent dyes were presented which, besides contributing to the very few published data, revealed a discrepancy with the cited nonlinear fluorescence excitation spectrum of one of the dyes. A key component of the FRET system is rapid wavelength tunability, which greatly simplified the process of signal calibration which is essential for accurate FRET measurement.

Future Directions

The CARS system developed in this work leaves the potential for two key developments: 1) incremental improvements to the power level of pulsed fiber lasers, and 2) refinement of the tuning and alignment hardware. In light of these remaining goals, this work has demonstrated that practical CARS and FRET systems could be designed based on the new technology of fiber lasers. It is hoped that with the increasing availability and quality of pulsed fiber lasers and a large variety of specialty nonlinear fibers, and a growing use of non-invasive spectroscopy in scientific communities, these systems may be used more easily and with more widespread application.

VI. Acknowledgements of Collaborators

The CARS and FRET systems were developed in collaboration with Dr. Carey K. Johnson (University of Kansas Department of Chemistry), who contributed significant expertise and resources to this work.

Samples of purified Calmodulin protein labeled with Alexa Fluor and Texas Red fluorescent dyes were prepared and kindly provided by Matthew S. Devore (University of Kansas).

The mCherry-Green Fluorescent Protein (E^0GFP-mCh) plasmid was developed and kindly donated by Dr. Lorenzo Albertazzi (Scuola Normale Superiore and Istituto Italiano di Tecnologia, Pisa, Italy).

Samples of mouse brain tissue used for CARS spectroscopy and imaging experiments were prepared and kindly provided by Dr. Jingqi Yan (University of Kansas Department of Pharmacology & Toxicology).

The CARS System was developed together with Dr. Carey K. Johnson (University of Kansas Department of Chemistry), with helpful assistance in design and initial tests by Dr. David C. Arnett (Northwestern College, Iowa).

The Quantitative Two-Photon FRET System was developed together with Dr. Carey K. Johnson (University of Kansas Department of Chemistry), with contributions by Gideon VanRiette (University of Kansas) (work on initial design and assembly) as well as helpful assistance from Matthew S. Devore (University of Kansas).

VII. References

1. A. Einstein, "Quantum theory of radiation.," Phys Z 18, 121-128 (1917).
2. L. M. Biberman, B. A. Veklenko, V. L. Ginzburg, G. S. Zhdanov, B. B. Kadmotsev, S. M. Rytov, B. M. Smirnov, I. L. Fabelinskii, E. L. Feinberg, and I. A. Yakovlev, "Fabrikant,Valentin,Aleksandrovich (Obituary)," Usp Fiz Nauk+ 161, 215-218 (1991).
3. S. G. Lukishova, "Valentin A. Fabrikant: negative absorption, his 1951 patent application for amplification of electromagnetic radiation (ultraviolet, visible, infrared and radio spectral regions) and his experiments," J Eur Opt Soc-Rapid 5(2010).
4. J. Hecht, "A short history of laser development," Appl Opt 49, F99-122 (2010).
5. D. Gabor, "A new microscopic principle," Nature 161, 777 (1948).
6. P. D. Maker and R. W. Terhune, "Study of Optical Effects Due to an Induced Polarization Third Order in Electric Field Strength," Phys Rev 137, A801-& (1965).
7. E. Snitzer, "Proposed Fiber Cavities for Optical Masers," J Appl Phys 32, 36-& (1961).
8. A. L. Schawlow and C. H. Townes, "Infrared and Optical Masers," Phys Rev 112, 1940-1949 (1958).
9. D. You, R. R. Jones, P. H. Bucksbaum, and D. R. Dykaar, "Generation of High-Power Sub-Single-Cycle 500-Fs Electromagnetic Pulses," Optics Letters 18, 290-292 (1993).
10. M. Y. Shverdin, D. R. Walker, D. D. Yavuz, G. Y. Yin, and S. E. Harris, "Generation of a single-cycle optical pulse," Physical Review Letters 94(2005).
11. K. Yamane, Z. G. Zhang, K. Oka, R. Morita, M. Yamashita, and A. Suguro, "Optical pulse compression to 3.4 fs in the monocycle region by feedback phase compensation," Optics Letters 28, 2258-2260 (2003).
12. S. Benson, G. Biallas, C. Bohn, D. Douglas, H. F. Dylla, R. Evans, J. Fugitt, R. Hill, K. Jordan, G. Krafft, R. Legg, R. Li, L. Merminga, G. R. Neil, D. Oepts, P. Piot, J. Preble, M. Shinn, T. Siggins, R. Walker, and B. Yunn, "First lasing of the Jefferson Lab IR Demo FEL," Nucl Instrum Meth A 429, 27-32 (1999).
13. J. Hecht, *City of light : the story of fiber optics*, The Sloan technology series (Oxford University Press, New York, 1999), pp. xii, 316 p.
14. G. P. Agrawal, *Nonlinear fiber optics,* 4th ed., Quantum electronics--principles and applications (Elsevier / Academic Press, Amsterdam ; Boston, 2007), pp. xvi, 529 p.
15. M. D. Levenson and S. Kano, *Introduction to nonlinear laser spectroscopy,* Rev. ed., Quantum electronics--principles and applications (Academic Press, Boston, 1988), pp. xvi, 299 p.
16. Y. R. Shen, *The principles of nonlinear optics,* Wiley classics library ed., Wiley classics library (Wiley-Interscience, Hoboken, N.J., 2003), pp. xii, 563 p.
17. M. Sargent, M. O. Scully, and W. E. Lamb, *Laser physics* (Addison-Wesley Pub. Co., Advanced Book Program, Reading, Mass.,, 1974), p. 432 p.
18. J. D. Jackson, *Classical electrodynamics,* 2d ed. (Wiley, New York, 1975), pp. xxii, 848 p.
19. IMRA, "Femtolite FX 100 Documentation", retrieved http://www.imra.com/pdf/FX-100.pdf.

20. W. H. Hayt and J. A. Buck, *Engineering electromagnetics,* 6th ed., McGraw-Hill series in electrical engineering (McGraw-Hill, Boston, 2001), pp. xiii, 561 p.
21. F. Träger, *Springer handbook of lasers and optics* (Springer, New York, 2007), pp. xxvi, 1332 p.
22. B. G. Streetman and S. Banerjee, *Solid state electronic devices,* 5th ed., Prentice Hall series in solid state physical electronics (Prentice Hall, Upper Saddle River, N.J., 2000), pp. xviii, 558 p.
23. K. S. Yee, "Numerical Solution of Initial Boundary Value Problems Involving Maxwells Equations in Isotropic Media," Ieee T Antenn Propag Ap14, 302-& (1966).
24. A. Taflove and M. E. Brodwin, "Numerical-Solution of Steady-State Electromagnetic Scattering Problems Using Time-Dependent Maxwells Equations," Ieee T Microw Theory 23, 623-630 (1975).
25. R. M. Joseph, S. C. Hagness, and A. Taflove, "Direct time integration of Maxwell's equations in linear dispersive media with absorption for scattering and propagation of femtosecond electromagnetic pulses," Opt Lett 16, 1412-1414 (1991).
26. P. M. Goorjian, A. Taflove, R. M. Joseph, and S. C. Hagness, "Computational Modeling of Femtosecond Optical Solitons from Maxwell Equations," Ieee J Quantum Elect 28, 2416-2422 (1992).
27. D. M. Sullivan, "Frequency-Dependent Fdtd Methods Using Z-Transforms," Ieee T Antenn Propag 40, 1223-1230 (1992).
28. D. M. Sullivan, "Nonlinear Fdtd Formulations Using Z-Transforms," Ieee T Microw Theory 43, 676-682 (1995).
29. W. H. Weedon and C. M. Rappaport, "A general method for FDTD modeling of wave propagation in arbitrary frequency-dispersive media," Ieee T Antenn Propag 45, 401-410 (1997).
30. M. Y. Koledintseva, J. Zhang, J. Wu, J. L. Drewniak, and K. N. Rozanov, "Development of an FDTD Tool for Modeling of Dispersive Media Part I," (2003).
31. M. Y. Koledintseva, J. Zhang, J. Wu, J. L. Drewniak, and K. N. Rozanov, "Development of an FDTD Tool for Modeling of Dispersive Media Part II," (2003).
32. S. Nakamura, N. Takasawa, and Y. Koyamada, "Comparison between finite-difference time-domain calculation with all parameters of Sellmeier's fitting equation and experimental results for slightly chirped 12-fs laser pulse propagation in a silica fiber," J Lightwave Technol 23, 855-863 (2005).
33. E. E. Serebryannikov, A. M. Zheltikov, N. Ishii, C. Y. Teisset, S. Kohler, T. Fuji, T. Metzger, F. Krausz, and A. Baltuska, "Nonlinear-optical spectral transformation of few-cycle laser pulses in photonic-crystal fibers," Phys Rev E Stat Nonlin Soft Matter Phys 72, 056603 (2005).
34. R. Hui and M. S. O'Sullivan, *Fiber optic measurement techniques* (Elsevier/Academic Press, Amsterdam ; London, 2009), pp. xvii, 652 p.
35. C. Pask and A. Vatarescu, "Spectral Approach to Pulse-Propagation in a Dispersive Nonlinear Medium," J Opt Soc Am B 3, 1018-1024 (1986).
36. W. M. Zhao and E. Bourkoff, "Femtosecond Pulse-Propagation in Optical Fibers - Higher-Order Effects," Ieee J Quantum Elect 24, 365-372 (1988).

37. S. V. Chernikov and P. V. Mamyshev, "Femtosecond Soliton Propagation in Fibers with Slowly Decreasing Dispersion," J Opt Soc Am B 8, 1633-1641 (1991).
38. P. L. Francois, "Nonlinear Propagation of Ultrashort Pulses in Optical Fibers - Total Field Formulation in the Frequency-Domain," J Opt Soc Am B 8, 276-293 (1991).
39. Demartin.F, C. H. Townes, Gustafso.Tk, and P. L. Kelley, "Self-Steepening of Light Pulses," Phys Rev 164, 312-& (1967).
40. M. J. Ablowitz, D. J. Kaup, A. C. Newell, and H. Segur, "Inverse Scattering Transform-Fourier Analysis for Nonlinear Problems," Stud Appl Math 53, 249-315 (1974).
41. J. P. Gordon, "Theory of the soliton self-frequency shift," Opt Lett 11, 662-664 (1986).
42. F. M. Mitschke and L. F. Mollenauer, "Discovery of the soliton self-frequency shift," Opt Lett 11, 659-661 (1986).
43. P. V. Mamyshev and S. V. Chernikov, "Ultrashort-Pulse Propagation in Optical Fibers," Optics Letters 15, 1076-1078 (1990).
44. D. V. Skryabin, F. Luan, J. C. Knight, and P. S. Russell, "Soliton self-frequency shift cancellation in photonic crystal fibers," Science 301, 1705-1708 (2003).
45. E. E. Serebryannikov, M. L. Hu, Y. F. Li, C. Y. Wang, Z. Wang, L. Chai, and A. M. Zheltikov, "Enhanced soliton self-frequency shift of ultrashort light pulses," Jetp Lett+ 81, 487-490 (2005).
46. N. Ishii, C. Y. Teisset, S. Kohler, E. E. Serebryannikov, T. Fuji, T. Metzger, F. Krausz, A. Baltuska, and A. M. Zheltikov, "Widely tunable soliton frequency shifting of few-cycle laser pulses," Phys Rev E Stat Nonlin Soft Matter Phys 74, 036617 (2006).
47. M. Erkintalo, G. Genty, B. Wetzel, and J. M. Dudley, "Limitations of the linear Raman gain approximation in modeling broadband nonlinear propagation in optical fibers," Opt Express 18, 25449-25460 (2010).
48. M. J. Ablowitz, D. J. Kaup, A. C. Newell, and H. Segur, "Nonlinear-Evolution Equations of Physical Significance," Physical Review Letters 31, 125-127 (1973).
49. A. Hasegawa and F. Tappert, "Transmission of Stationary Nonlinear Optical Pulses in Dispersive Dielectric Fibers .1. Anomalous Dispersion," Appl Phys Lett 23, 142-144 (1973).
50. L. M. Degtyarëv and V. V. Krylov, "A method for the numerical solution of problems of the dynamics of wave fields with singularities," USSR Computational Mathematics and Mathematical Physics 17, 172-179 (1977).
51. S. N. Vlasov, V. A. Petrishchev, and V. I. Talanov, "Averaged description of wave beams in linear and nonlinear media (the method of moments)," Radiophysics and Quantum Electronics 14, 1062-1070 (1971).
52. V. S. Grigoryan, C. R. Menyuk, and R. M. Mu, "Calculation of timing and amplitude jitter in dispersion-managed optical fiber communications using linearization," J Lightwave Technol 17, 1347-1356 (1999).
53. J. P. Gordon and H. A. Haus, "Random walk of coherently amplified solitons in optical fiber transmission," Opt Lett 11, 665-667 (1986).
54. J. Santhanam and G. P. Agrawal, "Raman-induced spectral shifts in optical fibers: general theory based on the moment method," Opt Commun 222, 413-420 (2003).

55. R. G. Molla, "Nonlinear Fiber Optics for Bio-Imaging," Thesis (University of Kansas, Lawrence, KS, 2005).
56. R. A. Fisher and W. K. Bischel, "Numerical studies of the interplay between self-phase modulation and dispersion for intense plane-wave laser pulses," J Appl Phys 46, 4921-4934 (1975).
57. O. V. Sinkin, R. Holzlohner, J. Zweck, and C. R. Menyuk, "Optimization of the split-step Fourier method in modeling optical-fiber communications systems," J Lightwave Technol 21, 61-68 (2003).
58. R. H. Stolen, J. P. Gordon, W. J. Tomlinson, and H. A. Haus, "Raman Response Function of Silica-Core Fibers," J Opt Soc Am B 6, 1159-1166 (1989).
59. G. W. Gordon, G. Berry, X. H. Liang, B. Levine, and B. Herman, "Quantitative fluorescence resonance energy transfer measurements using fluorescence microscopy," Biophys J 74, 2702-2713 (1998).
60. K. Mori, H. Takara, and S. Kawanishi, "Analysis and design of supercontinuum pulse generation in a single-mode optical fiber," J Opt Soc Am B 18, 1780-1792 (2001).
61. VPI-Photonics, VPI Transmission Maker V8.7, VPIsystems, Inc., VPIsystems, Inc. 300 Atrium Drive, Somerset, NJ 08873 USA, (732) 332-0233, 2012
62. T. Förster, "Zwischenmolekulare Energiewanderung und Fluoreszenz," Annalen der Physik 437, 55-75 (1948).
63. L. Stryer, "Fluorescence energy transfer as a spectroscopic ruler," Annu Rev Biochem 47, 819-846 (1978).
64. L. Albertazzi, D. Arosio, L. Marchetti, F. Ricci, and F. Beltram, "Quantitative FRET analysis with the EGFP-mCherry fluorescent protein pair," Photochem Photobiol 85, 287-297 (2009).
65. R. M. Clegg, "Fluorescence resonance energy transfer and nucleic acids," Methods Enzymol 211, 353-388 (1992).
66. L. N. Hillesheim, Y. Chen, and J. D. Muller, "Dual-color photon counting histogram analysis of mRFP1 and EGFP in living cells," Biophys J 91, 4273-4284 (2006).
67. M. Millington, G. J. Grindlay, K. Altenbach, R. K. Neely, W. Kolch, M. Bencina, N. D. Read, A. C. Jones, D. T. Dryden, and S. W. Magennis, "High-precision FLIM-FRET in fixed and living cells reveals heterogeneity in a simple CFP-YFP fusion protein," Biophys Chem 127, 155-164 (2007).
68. N. Panchuk-Voloshina, R. P. Haugland, J. Bishop-Stewart, M. K. Bhalgat, P. J. Millard, F. Mao, and W. Y. Leung, "Alexa dyes, a series of new fluorescent dyes that yield exceptionally bright, photostable conjugates," J Histochem Cytochem 47, 1179-1188 (1999).
69. N. C. Shaner, R. E. Campbell, P. A. Steinbach, B. N. Giepmans, A. E. Palmer, and R. Y. Tsien, "Improved monomeric red, orange and yellow fluorescent proteins derived from Discosoma sp. red fluorescent protein," Nat Biotechnol 22, 1567-1572 (2004).
70. D. C. Youvan, C. M. Silva, E. J. Bylina, W. J. Coleman, M. R. Dilworth, and M. M. Yang, "Calibration of Fluorescence Resonance Energy Transfer in Microscopy Using Genetically Engineered GFP Derivatives on Nickel Chelating Beads," Biotechnology et alia 3, 1-18 (1997).

71. H. Chen, H. L. Puhl, 3rd, S. V. Koushik, S. S. Vogel, and S. R. Ikeda, "Measurement of FRET efficiency and ratio of donor to acceptor concentration in living cells," Biophys J 91, L39-41 (2006).

72. C. Dinant, M. E. van Royen, W. Vermeulen, and A. B. Houtsmuller, "Fluorescence resonance energy transfer of GFP and YFP by spectral imaging and quantitative acceptor photobleaching," J Microsc 231, 97-104 (2008).

73. M. G. Erickson, B. A. Alseikhan, B. Z. Peterson, and D. T. Yue, "Preassociation of calmodulin with voltage-gated Ca(2+) channels revealed by FRET in single living cells," Neuron 31, 973-985 (2001).

74. A. Periasamy and A. Diaspro, "Multiphoton microscopy," J Biomed Opt 8, 327-328 (2003).

75. W. Denk, J. H. Strickler, and W. W. Webb, "Two-photon laser scanning fluorescence microscopy," Science 248, 73-76 (1990).

76. A. N. Kapanidis, N. K. Lee, T. A. Laurence, S. Doose, E. Margeat, and S. Weiss, "Fluorescence-aided molecule sorting: analysis of structure and interactions by alternating-laser excitation of single molecules," Proc Natl Acad Sci U S A 101, 8936-8941 (2004).

77. B. K. Müller, E. Zaychikov, C. Brauchle, and D. C. Lamb, "Pulsed Interleaved Excitation," Biophys J 89, 3508-3522 (2005).

78. P. Adany, E. S. Price, C. K. Johnson, R. Zhang, and R. Q. Hui, "Switching of 800 nm femtosecond laser pulses using a compact PMN-PT modulator," Review of Scientific Instruments 80(2009).

79. J. R. Unruh, E. S. Price, R. G. Molla, L. Stehno-Bittel, C. K. Johnson, and R. Hui, "Two-photon microscopy with wavelength switchable fiber laser excitation," Opt Express 14, 9825-9831 (2006).

80. M. W. Allen, R. J. Urbauer, and C. K. Johnson, "Single-molecule assays of calmodulin target binding detected with a calmodulin energy-transfer construct," Anal Chem 76, 3630-3637 (2004).

81. M. G. Banaee and J. F. Young, "High-order soliton breakup and soliton self-frequency shifts in a microstructured optical fiber," J. Opt. Soc. Am. B 23, 1484-1489 (2006).

82. J. C. Knight, J. Arriaga, T. A. Birks, A. Ortigosa-Blanch, W. J. Wadsworth, and P. S. J. Russell, "Anomalous dispersion in photonic crystal fiber," Photonics Technology Letters, IEEE 12, 807-809 (2000).

83. M. Albota, D. Beljonne, J. L. Bredas, J. E. Ehrlich, J. Y. Fu, A. A. Heikal, S. E. Hess, T. Kogej, M. D. Levin, S. R. Marder, D. McCord-Maughon, J. W. Perry, H. Rockel, M. Rumi, G. Subramaniam, W. W. Webb, X. L. Wu, and C. Xu, "Design of organic molecules with large two-photon absorption cross sections," Science 281, 1653-1656 (1998).

84. M. A. Albota, C. Xu, and W. W. Webb, "Two-Photon Fluorescence Excitation Cross Sections of Biomolecular Probes from 690 to 960 nm," Appl Opt 37, 7352-7356 (1998).

85. C. Xu and W. W. Webb, "Measurement of two-photon excitation cross sections of molecular fluorophores with data from 690 to 1050 nm," J. Opt. Soc. Am. B 13, 481-491 (1996).

86. F. Bestvater, E. Spiess, G. Stobrawa, M. Hacker, T. Feurer, T. Porwol, U. Berchner-Pfannschmidt, C. Wotzlaw, and H. Acker, "Two-photon fluorescence absorption and emission spectra of dyes relevant for cell imaging," J Microsc 208, 108-115 (2002).

87. B. D. Slaughter, J. R. Unruh, E. S. Price, J. L. Huynh, R. J. Bieber Urbauer, and C. K. Johnson, "Sampling unfolding intermediates in calmodulin by single-molecule spectroscopy," J Am Chem Soc 127, 12107-12114 (2005).

88. J. van Howe, J. H. Lee, S. Zhou, F. Wise, C. Xu, S. Ramachandran, S. Ghalmi, and M. F. Yan, "Demonstration of soliton self-frequency shift below 1300 nm in higher-order mode, solid silica-based fiber," Opt Lett 32, 340-342 (2007).

89. B. Hudson, W. Hetherington, S. Cramer, I. Chabay, and G. K. Klauminzer, "Resonance Enhanced Coherent Anti-Stokes Raman-Scattering," Proceedings of the National Academy of Sciences of the United States of America 73, 3798-3802 (1976).

90. W. M. Tolles, J. W. Nibler, J. R. Mcdonald, and A. B. Harvey, "Review of Theory and Application of Coherent Anti-Stokes Raman-Spectroscopy (Cars)," Applied Spectroscopy 31, 253-271 (1977).

91. N. Bloembergen, "Nonlinear optics and spectroscopy," Science 216, 1057-1064 (1982).

92. R. Leonhardt, W. Holzapfel, W. Zinth, and W. Kaiser, "Terahertz Quantum Beats in Molecular Liquids," Chem Phys Lett 133, 373-377 (1987).

93. E. T. J. Nibbering, D. A. Wiersma, and K. Duppen, "Ultrafast Nonlinear Spectroscopy with Chirped Optical Pulses," Physical Review Letters 68, 514-517 (1992).

94. A. M. Zheltikov, "Coherent anti-Stokes Raman scattering: from proof-of-the-principle experiments to femtosecond CARS and higher order wave-mixing generalizations," J Raman Spectrosc 31, 653-667 (2000).

95. J. X. Cheng and X. S. Xie, "Coherent anti-Stokes Raman scattering microscopy: Instrumentation, theory, and applications," Journal of Physical Chemistry B 108, 827-840 (2004).

96. F. Legare, C. L. Evans, F. Ganikhanov, and X. S. Xie, "Towards CARS Endoscopy," Opt Express 14, 4427-4432 (2006).

97. C. W. Freudiger, W. Min, B. G. Saar, S. Lu, G. R. Holtom, C. He, J. C. Tsai, J. X. Kang, and X. S. Xie, "Label-free biomedical imaging with high sensitivity by stimulated Raman scattering microscopy," Science 322, 1857-1861 (2008).

98. P. Gilch, E. Ploetz, S. Laimgruber, S. Berner, and W. Zinth, "Femtosecond stimulated Raman microscopy," Appl Phys B-Lasers O 87, 389-393 (2007).

99. J. X. Cheng, A. Volkmer, and X. S. Xie, "Theoretical and experimental characterization of coherent anti-Stokes Raman scattering microscopy," J Opt Soc Am B 19, 1363-1375 (2002).

100. N. Nishizawa and T. Goto, "Widely wavelength-tunable ultrashort pulse generation using polarization maintaining optical fibers," Ieee J Sel Top Quant 7, 518-524 (2001).

101. P. Adany, E. S. Price, C. K. Johnson, R. Zhang, and R. Hui, "Switching of 800 nm femtosecond laser pulses using a compact PMN-PT modulator," Rev Sci Instrum 80, 033107 (2009).

102. K. B. Shi, P. Li, and Z. W. Liu, "Broadband coherent anti-Stokes Raman scattering spectroscopy in supercontinuum optical trap," Appl Phys Lett 90(2007).

103. T. Hellerer, A. M. K. Enejder, and A. Zumbusch, "Spectral focusing: High spectral resolution spectroscopy with broad-bandwidth laser pulses," Appl Phys Lett 85, 25-27 (2004).
104. K. P. Knutsen, B. M. Messer, R. M. Onorato, and R. J. Saykally, "Chirped coherent anti-stokes Raman scattering for high spectral resolution spectroscopy and chemically selective imaging," J Phys Chem B 110, 5854-5864 (2006).
105. A. F. Pegoraro, A. Ridsdale, D. J. Moffatt, Y. Jia, J. P. Pezacki, and A. Stolow, "Optimally chirped multimodal CARS microscopy based on a single Ti:sapphire oscillator," Opt Express 17, 2984-2996 (2009).
106. I. R. Lewis and H. G. M. Edwards, *Handbook of Raman spectroscopy : from the research laboratory to the process line*, Practical spectroscopy (Marcel Dekker, New York, 2001), pp. xiii, 1054 p.
107. J. M. Chalmers and P. R. Griffiths, *Handbook of vibrational spectroscopy* (J. Wiley, New York, 2002).
108. C. Pohling, T. Buckup, A. Pagenstecher, and M. Motzkus, "Chemoselective imaging of mouse brain tissue via multiplex CARS microscopy," Biomed Opt Express 2, 2110-2116 (2011).
109. C. L. Evans, X. Xu, S. Kesari, X. S. Xie, S. T. Wong, and G. S. Young, "Chemically-selective imaging of brain structures with CARS microscopy," Opt Express 15, 12076-12087 (2007).
110. R. P. Feynman, R. Leighton, and E. Hutchings, *"Surely you're joking, Mr. Feynman!" : adventures of a curious character* (W.W. Norton, New York, 1985), p. 350 p.

VII. Appendix

Moments Equations Solutions

The results of the application of the moments method to the behavior of solitons are found in the literature references: [50-54]. However, the techniques to arrive at the solutions are not elucidated. The following solutions are provided in order to give insight to the moments analysis technique.

We start by consider the GNLSE with the following terms:

$$\frac{\partial A}{\partial z}+\frac{\alpha}{2}A+i\frac{\beta_2}{2}\frac{\partial^2 A}{\partial t^2}=i\gamma\left|A\right|^2 A \tag{103}$$

The energy of the pulse is defined as

$$E=\int_{-\infty}^{\infty}|A|^2\,dt \tag{104}$$

Taking the partial z-derivative of both sides, and using the following integral rule (said to be a favorite by R.P. Feynman [110]),

$$\frac{\partial}{\partial z}\int_{a(z)}^{b(z)}f(t,z)dt=f(t,b(z))\frac{\partial}{\partial z}b(z)-f(t,a(z))\frac{\partial}{\partial z}a(z)+\int_{a(z)}^{b(z)}\frac{\partial}{\partial z}f(t,z)dt \tag{105}$$

in this case the derivative can simply be moved inside the integral:

$$\frac{\partial}{\partial z}E=\int_{-\infty}^{\infty}\frac{\partial}{\partial z}|A|^2\,dt \tag{106}$$

Taking the conjugate of (103) and multiplying by A provides the following equation and its conjugate,

$$A\frac{\partial A^*}{\partial z}+\frac{\alpha}{2}AA^*-i\frac{\beta_2}{2}A\frac{\partial^2}{\partial t^2}A^*=-i\gamma\left|A\right|^2 AA^* \tag{107}$$

$$A^* \frac{\partial A}{\partial z} + \frac{\alpha}{2} A^* A + i \frac{\beta_2}{2} A^* \frac{\partial^2}{\partial t^2} A = i\gamma |A|^2 A^* A \tag{108}$$

Adding these two equations and extracting the $|A|^2$ terms provides the following,

$$\frac{\partial}{\partial z} |A|^2 = -\alpha |A|^2 - i\beta_2 \left(A^* \frac{\partial^2}{\partial t^2} A - A \frac{\partial^2}{\partial t^2} A^* \right) \tag{109}$$

and substituting this in the integral (106) results in

$$\frac{\partial}{\partial z} E = -\int_{-\infty}^{\infty} \alpha |A|^2 dt - \int_{-\infty}^{\infty} i\beta_2 \left(A^* \frac{\partial^2}{\partial t^2} A - A \frac{\partial^2}{\partial t^2} A^* \right) dt \tag{110}$$

which is the same as

$$\frac{\partial}{\partial z} E = -\alpha E - i\beta_2 \int_{-\infty}^{\infty} \left(A^* \frac{\partial^2}{\partial t^2} A - A \frac{\partial^2}{\partial t^2} A^* \right) dt \tag{111}$$

Intuitively, the propagation parameter β_2 should have no effect on the pulse energy, but as long as A is complex this is not mathematically ensured. We can also reason that the integration in (111) must be imaginary because the pulse energy must be a real value. Indeed, only imaginary terms occur in the integrand. This can be shown by dividing the envelope term into its real and imaginary parts as $A(t) = u(t) + iv(t)$. The integrand in these terms, is $i2(uv'' - u''v)$. Writing the field as a complex phasor $A(t) = U(t)e^{j\Omega_R t}$ where $U(t)$ is real valued, reduces the integrand to $i2\Omega_R U \frac{\partial}{\partial t} U$, leaving the following equation:

$$\frac{\partial}{\partial z} E = -\alpha E + 2\beta_2 \Omega_R \int_{-\infty}^{\infty} U \frac{\partial}{\partial t} U \, dt \tag{112}$$

For an arbitrary real valued $U(t)$ the result is

$$\frac{\partial}{\partial z} E = -\alpha E + 2\beta_2 \Omega_R \frac{1}{2} U(t)^2 \Big|_{-\infty}^{\infty} \tag{113}$$

which, for a time-limited waveform, results in the equation for the evolution of the pulse energy,

$$\frac{\partial}{\partial z}E = -\alpha E \tag{114}$$

More generally, integrals over infinity of a function of the form $F(t) - F(t)^*$ will vanish when F is a phasor with a real-valued envelope. Turning next to the time center of the pulse, we have

$$\frac{\partial}{\partial z}T = \frac{\partial}{\partial z}\frac{1}{E}\int_{-\infty}^{\infty} t|A|^2\,dt = -\frac{1}{E^2}\int_{-\infty}^{\infty} t|A|^2\,dt\,\frac{\partial}{\partial z}E + \frac{1}{E}\frac{\partial}{\partial z}\int_{-\infty}^{\infty} t|A|^2\,dt \tag{115}$$

which reduces as

$$\frac{\partial}{\partial z}T = \frac{\partial}{\partial z}\frac{1}{E}\int_{-\infty}^{\infty} t|A|^2\,dt = -\frac{T}{E^2}\frac{\partial}{\partial z}E + \frac{1}{E}\int_{-\infty}^{\infty} t\frac{\partial}{\partial z}|A|^2\,dt \tag{116}$$

next, we again substitute the GNLSE terms, this time jumping straight to the form involving the slowly varying envelope:

$$\frac{\partial}{\partial z}T = -\frac{T}{E^2}\frac{\partial}{\partial z}E + \frac{1}{E}\int_{-\infty}^{\infty}\left[-t\alpha|A|^2 - i\beta_2 t\left(i2\Omega_R U\frac{\partial}{\partial t}U\right)\right]dt \tag{117}$$

separating the integral into two parts, we have

$$\frac{\partial}{\partial z}T = -\frac{T}{E^2}\frac{\partial}{\partial z}E + \frac{-\alpha}{E}\int_{-\infty}^{\infty} t|A|^2\,dt + \frac{2\beta_2\Omega_R}{E}\int_{-\infty}^{\infty} t\left(U\frac{\partial}{\partial t}U\right)dt \tag{118}$$

now, recognizing relations (114) and (68), we have

$$\begin{aligned}\frac{\partial}{\partial z}T &= -\frac{T}{E^2} - \alpha E + \frac{-\alpha}{E}T + \frac{2\beta_2\Omega_R}{E}\int_{-\infty}^{\infty} t\left(U\frac{\partial}{\partial t}U\right)dt \\ &= \frac{\alpha T}{E} - \frac{\alpha T}{E} + \frac{2\beta_2\Omega_R}{E}\int_{-\infty}^{\infty} t\left(U\frac{\partial}{\partial t}U\right)dt\end{aligned} \tag{119}$$

which leaves

$$\frac{\partial}{\partial z}T = \frac{2\beta_2\Omega_R}{E}\int_{-\infty}^{\infty} t\left(U\frac{\partial}{\partial t}U\right)dt \tag{120}$$

next, we find by integration for arbitrary real valued $U(t)$ the following result,

$$\int_{-\infty}^{\infty} t\left(U\frac{\partial}{\partial t}U\right)dt = \frac{1}{2}\left(tU(t)^2\Big|_{-\infty}^{\infty} - \int_{-\infty}^{\infty} U(t)^2\,dt\right) = -\frac{1}{2}\int_{-\infty}^{\infty}|A(t)|^2\,dt = -\frac{E}{2} \quad (121)$$

therefore, we arrive at the expression for the pulse time center moments evolution,

$$\frac{\partial}{\partial z}T = -\beta_2\Omega_R \quad (122)$$

This demonstrates the general method for obtaining the differential solutions. Continuing with this procedure, explicit equations can be found for Gaussian and sech pulse shapes.